Available online at www.sciencedirect.com
ScienceDirect
Separation and Purification Technology 61 (2008) 414–423
Separation Purification Technology
www.elsevier.com/locate/seppur

Segregation effects in adsorption of CO_2-containing mixtures and their consequences for separation selectivities in cage-type zeolites

R. Krishna*, J.M. van Baten

Van't Hoff Institute for Molecular Sciences, University of Amsterdam, Nieuwe Achtergracht 166, 1018 WV Amsterdam, The Netherlands

Received 5 November 2007; received in revised form 1 December 2007; accepted 3 December 2007

Abstract

For separation of CO_2 from gaseous mixtures with CH_4, N_2, or Ar, cage-type zeolites such as DDR, CHA, LTA, and ERI are of practical interest. These zeolites consist of cages separated by narrow windows and the selectivity of separation of CO_2 is dictated by both adsorption and diffusion characteristics. For adsorption of CO_2/CH_4 mixtures, Grand Canonical Monte Carlo (GCMC) simulations show that the window regions of cage-type zeolites have a significantly higher proportion of CO_2 than within the cages. Due to the segregated nature of mixture adsorption, the ideal adsorbed solution theory is unable to predict the mixture loadings accurately. For adsorption of CO_2/N_2, CO_2/Ar, and N_2/CH_4 segregation effects are also present but their impact is far less severe than for CO_2/CH_4 mixtures.

For CO_2-bearing mixtures, the preponderance of CO_2 in the window regions has important consequences for mixture diffusion. Molecular dynamics (MD) simulations for self-diffusion in binary mixtures demonstrate that the CO_2 slows down the partner molecules far more than anticipated by the Maxwell–Stefan diffusion theory using pure component data inputs.

The GCMC and MD simulation results also lead to the conclusion that DDR and CHA yield the highest permeation selectivities for membrane-based separation of CO_2/CH_4, CO_2/N_2, and CO_2/Ar mixtures. For N_2/CH_4 separation, DDR and ERI are the best choices.

Keywords: Zeolite membrane; LTA; CHA; ERI; DDR; Adsorption selectivity; Permeation selectivity; CO_2 separation

1. Introduction

There is considerable interest in the use of zeolite membranes for separation of variety of mixtures such as CO_2/CH_4, N_2/CH_4, and CO_2/N_2 [1–6]. The permeation selectivity is dictated by both adsorption and diffusion characteristics of the components. For CO_2/N_2 separation, Ohta et al. [7] used a dynamic Monte Carlo combinatorial approach to conclude that the highest separation factors were obtained with zeolite structures that consist of cages separated by window openings smaller than about 4.2 Å. DDR, CHA, ERI and LTA cage-type zeolites fall into this category; see the window dimensions pictured in Fig. 1.

In the modeling of mixture permeation across zeolite membranes, a common practice is to use the ideal adsorbed solution theory (IAST) of Myers and Prausnitz [8] for estimating the component loadings in the mixture from information of pure component isotherm fits [1–3]. A key assumption of the IAST is that the composition of the adsorbed phase is spatially uniform within the zeolite. The first objective of the present communication is to demonstrate, using GCMC simulations, that for adsorption of binary mixtures containing CO_2, *segregation* effects are present in DDR, CHA, ERI and LTA zeolites. For these cage-type zeolites the window regions are richer in CO_2 when compared to the composition within the entire pore space. We show that segregation effects, in some cases, cause the failure of IAST to provide a good *quantitative* representation of component loadings. The second objective is to show, on the basis of MD simulations, that segregation effects also influence mixture diffusion in cage-type zeolites. We show that the Maxwell–Stefan (M–S) diffusion equations, commonly used to predict mixture diffusion on the basis of information on pure component diffusivity data, fails due to segregation effects. The reason for this failure can be traced to the preponderance of CO_2 in the window regions, hindering the inter-cage hopping of partner molecules in the mixture. The third objective is to compare the selectivities for separation of CO_2/CH_4, CO_2/N_2, CO_2/Ar, and N_2/CH_4 mixtures using DDR, CHA, ERI and LTA membranes.

* Corresponding author. Tel.: +31 20 5257007; fax: +31 20 5255604.
E-mail address: r.krishna@uva.nl (R. Krishna).

1383-5866/$ – see front matter © 2007 Elsevier B.V. All rights reserved.
doi:10.1016/j.seppur.2007.12.003

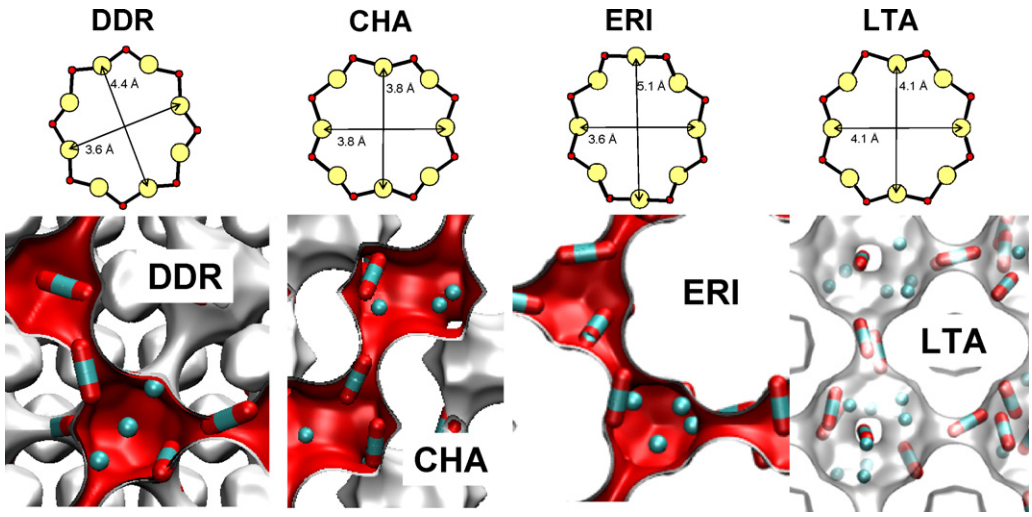

Fig. 1. Window dimensions of DDR, CHA, ERI, and LTA. Also shown are snapshots of the equilibrium locations of CH_4 and CO_2; these snapshots were obtained from NVT GCMC mixture simulatons.

The work reported here is an extension of our preliminary communication on segregation effects in DDR zeolite [9] and underlines the generic nature of segregation effects in cage-type zeolites. The GCMC and MD simulation methodologies, including information on the force fields used, along with detailed simulation results for pure component and mixture isotherms, segregation statistics, self-diffusivities in pure components and binary mixtures are given in Supplementary material accompanying this publication. A selection of this data is discussed below in order to draw a range of generic conclusions that are of practical importance.

2. Segregation effects in adsorption

Adsorption equilibria in DDR, CHA, ERI and LTA zeolites were computed using Monte Carlo (MC) simulations in the grand canonical (GC) ensemble. The crystallographic data are available elsewhere [10]. The zeolite lattices are assumed to be rigid in the simulations, with static atomic charges that are assigned by choosing $q_{Si} = +2.05$ and $q_O = -1.025$, following the works of Jaramillo and Auerbach [11] and Calero et al. [12]. CH_4 molecules are described with a united atom model, in which each molecule is treated as a single interaction center [13]. The interaction between adsorbed molecules is described with Coulombic and Lennard–Jones terms. The Coulombic interactions in the system are calculated by Ewald summation for periodic systems [14]. The parameters for CH_4 are taken from Dubbeldam et al. [15] and Calero et al. [12]. CO_2 molecules are taken linear and rigid with bond length C–O of 1.16 Å according to the 3LJ3CB.EPM2 model developed by Harris and Young [16]. We use the 2LJ3CB.MSKM model for N_2 dumbbell molecules with a rigid interatomic bond of 1.098 Å [17,18]. The partial charges of N_2 and CO_2 are distributed around each molecule to reproduce experimental quadrupole moment. The interactions between adsorbed molecules and the zeolite are dominated by dispersive forces between the pseudo-atoms and

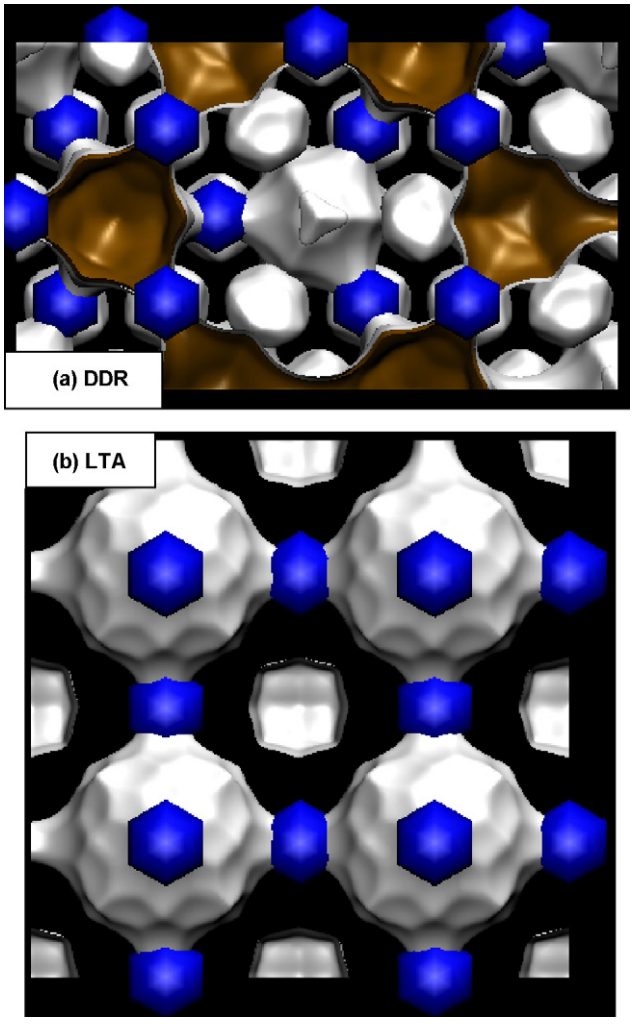

Fig. 2. Framework structures of: (a) DDR and (b) LTA. The blue spheres of 3 Å (for DDR) and 4 Å (for LTA) diameter are taken to indicate the window region. (For interpretation of the references to color in this figure legend, the reader is referred to the web version of the article.)

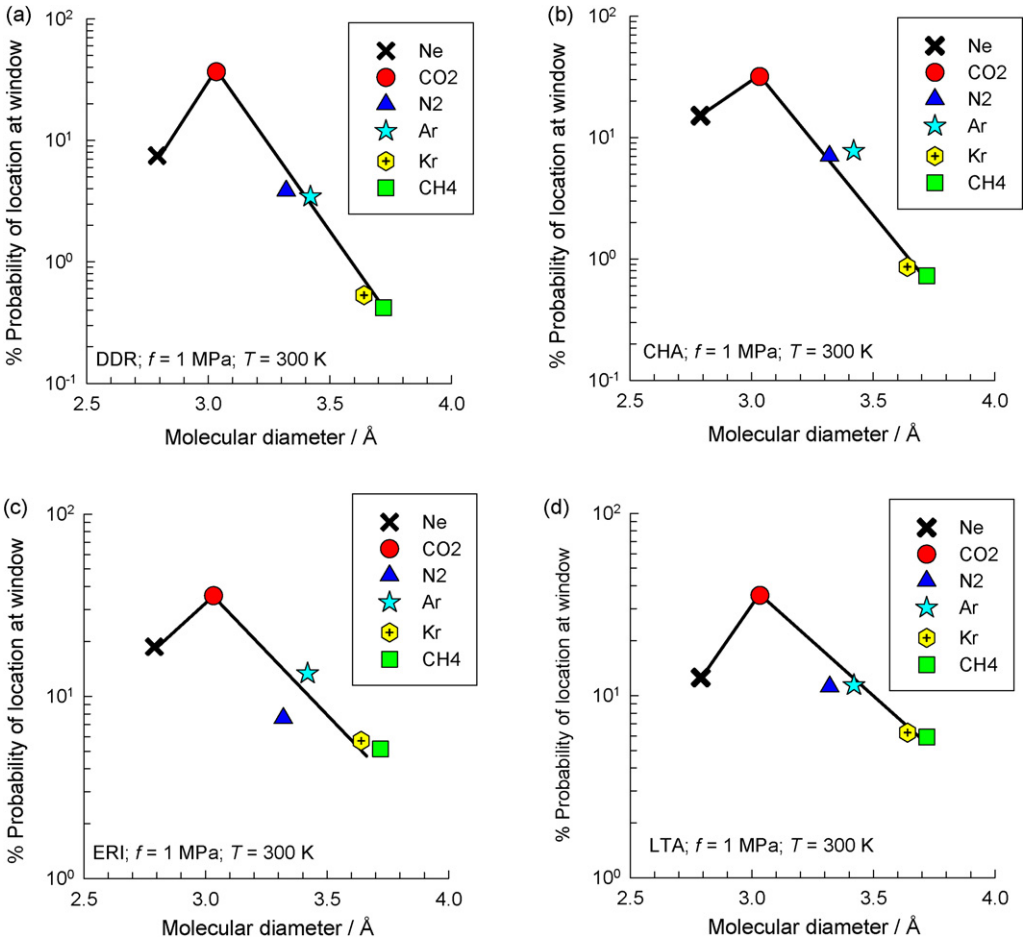

Fig. 3. Probability % for adsorption of component in the window region of: (a) DDR, (b) CHA, (c) ERI, and (d) LTA as function of the molecular diameter of CH_4, Ar, N_2, CO_2, Ne, and Kr.

the oxygen atoms of the zeolite [19,20] and the interactions of silicon and aluminium are considered through an effective potential with only the oxygen atoms. The Lennard–Jones parameters for CH_4–zeolite interactions are taken from Dubbeldam et al. [15]. The Lennard–Jones parameters for CO_2–zeolite and N_2–zeolite interactions are essentially those of Makrodimitris et al. [18]; see also García-Pérez et al. [21]. The force fields for Ne and Ar are taken from the paper by Skoulidas and Sholl [22]. The force field for Kr is from Talu and Myers [23].

Let us first consider adsorption of pure CH_4, Ar, N_2, CO_2, Ne, and Kr. GCMC simulations were run to determine the adsorption equilibrium at 300 K and 1 MPa. Each GCMC simulation was run for 10^7 cycles. The centers of the molecules were captured every 1000 cycles, starting at cycle 1000. Statistics of 10^4 samples of the equilibrium positions within the DDR, CHA, ERI and LTA frameworks were collected for each molecule. The window regions for each of the four zeolites were defined by drawing a sphere of diameter equal to either 3 Å (DDR and CHA) or 4 Å (ERI and LTA). As example, the framework structures of DDR and LTA are shown in Fig. 2; the spheres with a diameter of 3 Å (for DDR) and 4 Å (for LTA) encompass the window region. From the collected statistics the % probability of locating a molecule within the window region can be determined; the data are summarized in Fig. 3a–d. Probability density plots that provide a visual reinforcement of the data in Fig. 3 are available in Supplementary material. For all zeolites CO_2 has the highest probability, about 30–40%, of locating at the window regions. With increasing molecular diameter (Ar, N_2, Kr, CH_4), probability of locating at the window region decreases. For Kr and CH_4 the window regions are practically unpopulated because of the high degree of constraint experienced by these molecules at the window region. Ne has a smaller diameter than CO_2 but has a lower probability of locating at the window region; one possible explanation for this is that the molecular *length* of CO_2 is such that this molecule can nestle comfortably at the window of all four zeolites.

GCMC simulations were also carried out for adsorption of CO_2/CH_4 binary mixtures, with partial fugacities $f_1 = f_2 = 1$ MPa and $T = 300$ K. From 10^4 collected equilibrium samples, the adsorption selectivity, i.e. the ratio of the number of molecules of CO_2 to that of CH_4, could be determined separately for the entire pore space and within the cages; these data are summarized in Table 1. For all four zeolites, the adsorption selectivity within the cages is *lower* than that for the entire pores space. This is due to the higher proportion of CO_2 in the window regions, as compared to CH_4; the snapshots in Fig. 1 provide a visual demonstration of this. There are consequences of this segregated nature of mixture adsorption.

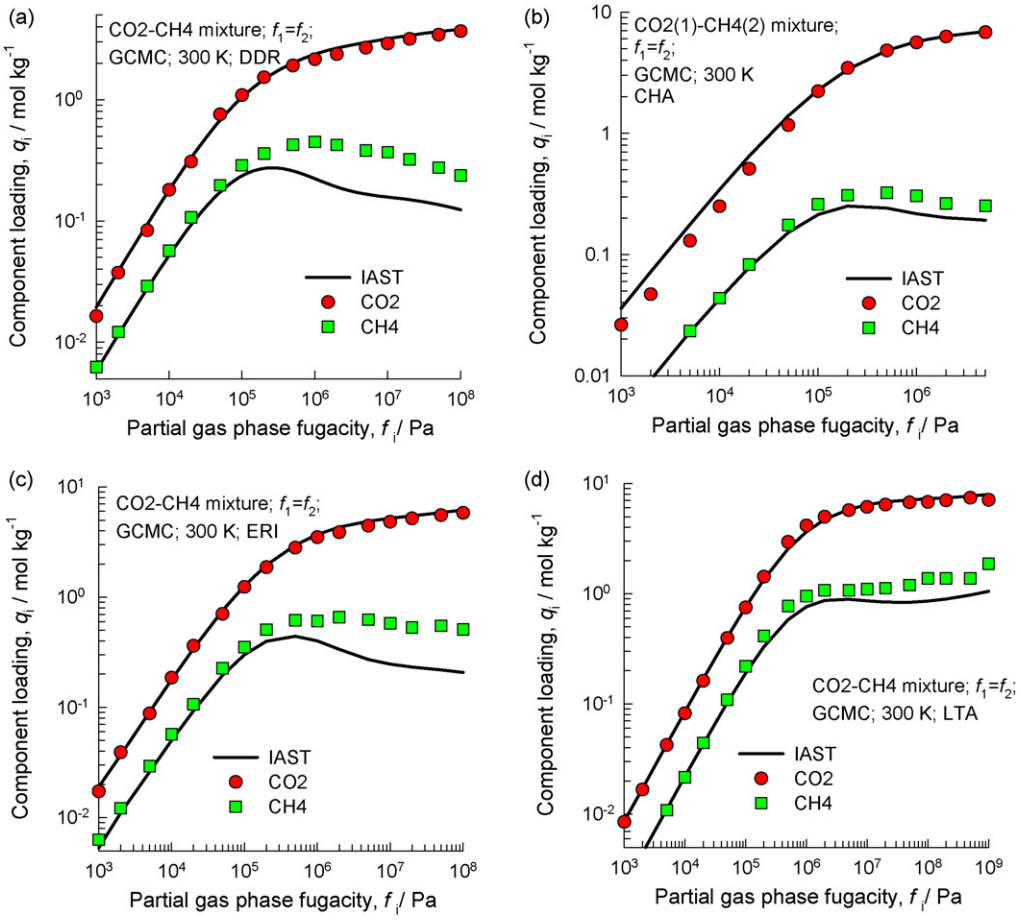

Fig. 4. GCMC simulations for the component loadings in equilibrium with equimolar CO_2/CH_4, gas mixtures in: (a) DDR, (b) CHA, (c) ERI, and (d) LTA at 300 K. The continuous solid lines represent calculations of the IAST [8] using three-site Langmuir fits of pure component isotherms with fitted parameter values as given in Supplementary material accompanying this publication.

GCMC simulations for the component loadings in equilibrium with equimolar CO_2/CH_4 gas mixtures for a range of partial fugacities f_i are shown in Fig. 4. We note that for all four zeolites, the IAST under-predicts the loading of the more weakly adsorbed CH_4 in the CO_2/CH_4 mixture at high gas phase fugacities. The conventional IAST calculation assumes that CH_4 molecules compete with *all* of the CO_2, making no allowance for segregation. Due to segregation effects the competition faced by CH_4 molecules within the cages, where they almost exclusively reside, is *smaller* than that in the entire pore space, as witnessed by the data in Table 1 for partial fugacities $f_1 = f_2 = 1$ MPa. The IAST anticipates a stiffer competition between CO_2 and CH_4 as it assumes a uniform distribution of composition; consequently the separation selectivity is *over*estimated.

A further point to note from Fig. 4 is that the predictions of IAST are poorer for DDR and ERI than for CHA and LTA. The reason for this is to be found in the capacity within the cages. Both CHA and LTA have significantly higher cage capacities than DDR and ERI. Consequently, segregation effects are of lesser significance.

From Fig. 4 we also note that the predictions of the IAST become progressively worse with increasing fugacities f_i. For all four zeolites, segregation effects are negligibly small for partial fugacities $f_i < 100$ kPa. Simulations with varying temperatures and isobaric conditions were also carried out. For CO_2/CH_4 mixture adsorption in DDR with partial fugacities $f_1 = f_2 = 500$ kPa we note that the predictions of IAST become progressively worse when the temperature is decreased; see Fig. 5a. Generally speaking, the consequences of segregation effects in the modeling of zeolite membrane permeation are more severe at high loadings within the zeolites, as we shall demonstrate later in this paper. The IAST predictions of the *total* mixture loading, $q_1 + q_2$, are in good agreement with the GCMC simulation results in all cases; this is illustrated in see Fig. 5b.

Table 1
Adsorption selectivity in mixtures, determined from the statistics on location of molecules within cages only, and within the entire pore structure of DDR, CHA, ERI, and LTA

Zeolite	Selectivity within cages	Selectivity in total pore structure
DDR	2.9	5
CHA	13.3	19.3
ERI	3.5	5.4
LTA	2.9	4.8

The data obtained for equimolar binary CO_2/CH_4 mixtures at 300 K and partial fugacities of 1 MPa.

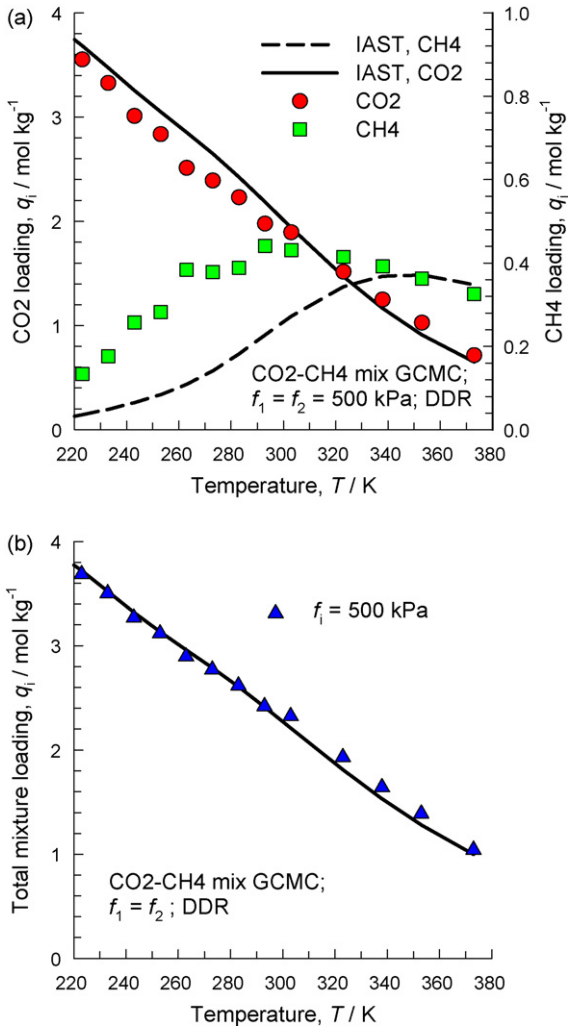

Fig. 5. GCMC simulations for the: (a) component loadings and (b) total mixture loading in equilibrium with equimolar CO_2/CH_4, gas mixtures in DDR with partial gas phase fugacities $f_1 = f_2 = 500$ kPa, and varying temperatures. The continuous solid lines represent calculations of the IAST [8] using three-site Langmuir fits of pure component isotherms with fitted parameter values as given in Supplementary material accompanying this publication.

Segregation effects were also investigated for CO_2/N_2, CO_2/Ar, and N_2/CH_4 mixtures in the four cage-type zeolites; details are available in Supplementary material. In all cases the impact of segregation were considerably less significant; departures of IAST predictions from GCMC mixture simulations were significantly smaller than for CO_2/CH_4 mixtures.

The failure of the IAST to provide a good quantitative description of mixture adsorption when segregation effects occur due to preferential location of branched and cyclic hydrocarbons at the intersections of MFI zeolite have been stressed earlier by Murthi and Snurr [24] and Krishna and van Baten [25].

2.1. Segregation effects in mixture diffusion

The Maxwell–Stefan (M–S) diffusion equations are widely used in practice [26,27] to model mixture diffusion. For binary mixtures, the M–S equations are

$$-\rho\frac{\theta_i}{RT}\frac{\mathrm{d}\mu_i}{\mathrm{d}x} = \sum_{\substack{j=1\\ j\neq i}}^{2}\frac{q_jN_i - q_iN_j}{q_{i,\mathrm{sat}}q_{j,\mathrm{sat}}Đ_{ij}} + \frac{N_i}{q_{i,\mathrm{sat}}Đ_i}; \quad i = 1,2 \tag{1}$$

where N_i is the molar flux, ρ the zeolite framework density, q_i the molar loading, $q_{i,\mathrm{sat}}$ the saturation capacity, $\mathrm{d}\mu_i/\mathrm{d}x$ the chemical potential gradient, R the gas constant, T is the absolute temperature, $Đ_i$ the M–S diffusivity of species i and $Đ_{ij}$ are the binary exchange coefficients. Within the framework of the M–S formulation correlation effects are embodied in the exchange coefficients $Đ_{ij}$ that quantify the extent of slowing-down of the more mobile species and speeding-up of the tardier species [26,27]. Conformity with the Onsager reciprocal relations demands that

$$q_{j,\mathrm{sat}}Đ_{ij} = q_{i,\mathrm{sat}}Đ_{ji} \tag{2}$$

In Eq. (1) the fractional occupancies θ_i are defined by

$$\theta_i \equiv q_i/q_{i,\mathrm{sat}} \quad i = 1,2 \tag{3}$$

Eq. (1) offer the possibility of predicting the diffusion characteristics in a binary mixture from pure component diffusion data by making the following two assumptions. First, we assume that the $Đ_i$ in the mixture is the same as that of pure component i, and estimate this diffusivity at the same occupancy as that of the *total* mixture, $\theta_1 + \theta_2$; this procedure has been explained earlier [3,26]. Second, we estimate the $Đ_{ij}$ using the interpolation formula, suggested earlier [28,29]

$$q_{2,\mathrm{sat}}Đ_{12} = [q_{2,\mathrm{sat}}Đ_{11}]^{q_1/(q_1+q_2)}[q_{1,\mathrm{sat}}Đ_{22}]^{q_2/(q_1+q_2)} \tag{4}$$

The self-exchange coefficients $Đ_{11}$ and $Đ_{22}$ quantify the correlation effects of pure components 1 and 2; these can be determined from information of self- ($D_{i,\mathrm{self}}$) and M–S-diffusivities of pure components. The pure component M–S diffusivities $Đ_i$ and the exchange coefficients $Đ_{ii}$ are all strong functions of the loading for all guest-zeolite combinations considered in this work. The loading dependence of $Đ_i$ is best described using the Reed and Ehrlich model described in an earlier publication [26] and this data is also available in Supplementary material, along with the correlations for the exchange coefficients.

The M–S equations lead to the following expression for the self-diffusivities in the mixture [29]:

$$D_{1,\mathrm{self}} = \frac{1}{(1/Đ_1) + (q_1/q_{1,\mathrm{sat}}Đ_{11}) + (q_2/q_{2,\mathrm{sat}}Đ_{12})};$$
$$D_{2,\mathrm{self}} = \frac{1}{(1/Đ_2 + (q_2/q_{2,\mathrm{sat}}Đ_{22}) + (q_1/q_{1,\mathrm{sat}}Đ_{21})} \tag{5}$$

Eq. (5) has been verified to be of good accuracy for a wide variety of alkane mixtures in different zeolites [29,30].

We now test the predictions of Eq. (5), using pure component diffusion data inputs, against MD simulation results of self-diffusivities in CO_2-bearing mixtures in cage-type zeolites. Fig. 6 shows the data on self-diffusivities in CO_2/Ar mixtures, at a fixed value of total loading in the mixture, $q_1 + q_2$, for

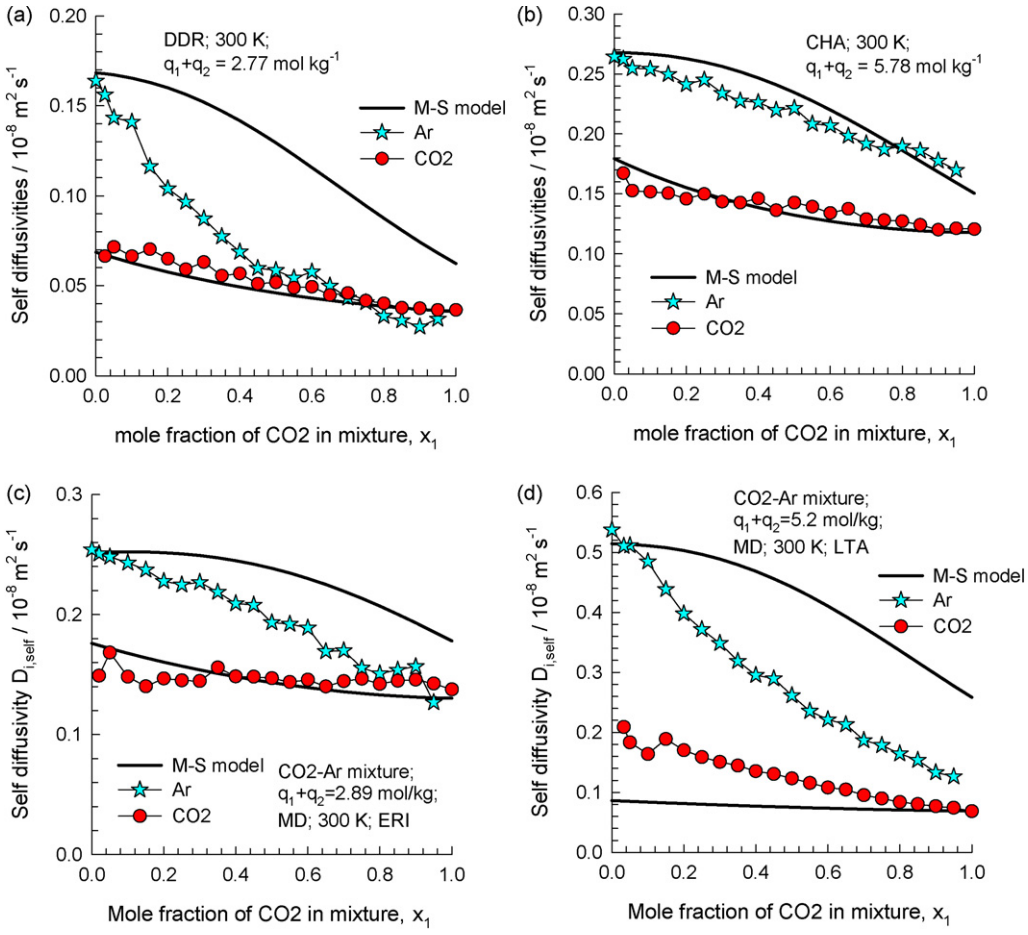

Fig. 6. Self-diffusivities in CO_2/Ar mixtures in: (a) DDR, (b) CHA, (c) ERI, and (d) LTA at 300 K obtained keeping total mixture loading constant for each zeolite. The continuous solid lines are calculations using Eq. (5).

the four cage-type zeolites. For all four zeolites the total loading was chosen to be large enough so that segregation effects would be significant. In all four zeolites, Ar is the more mobile species and CO_2 is the tardier species. Correlation effects tend to slow down self-diffusion of Ar, while speeding-up that of CO_2. For CHA, Eq. (5) are in reasonably good agreement with MD simulations of $D_{i,self}$ of either species. For DDR and ERI, while the predictions of CO_2 are good, Eq. (5) severely overestimates the $D_{i,self}$ of Ar. It appears the CO_2 suppresses the diffusion of Ar much more than anticipated by the M–S formulation. The same conclusions also hold for LTA zeolite, for which the predictions of self-diffusion of CO_2 are also not very good.

A similar situation emerges for CO_2/N_2 mixtures; in DDR, ERI, and LTA the overwhelming presence of CO_2 in the window regions retards the diffusion of N_2 much more than anticipated by the M–S equations; see Fig. 7. For CHA, the predictions of the M–S equations are reasonably good for either species. Indeed the experimental data for permeation of CO_2/N_2 mixtures across a SAPO-34 (an isotype of CHA) membrane could be modeled adequately by use of the M–S formulation [1].

Fig. 8 compares MD simulations of $D_{i,self}$ in CO_2/CH_4 mixtures with the predictions of Eq. (5). For CHA, the predictions of the M–S equations are very good for either species, explaining the good match between experimental data permeation data across a SAPO-34 membrane and the M–S formulation [1]. For DDR, ERI, and LTA zeolites the MD simulations for CH_4 show a considerably stronger reduction in $D_{i,self}$ with increasing presence of CO_2 than anticipated by the M–S predictions. For DDR and ERI, the reduction in the self-diffusivity of CH_4 with increasing proportion of CO_2, as witnessed in MD simulations, is remarkable because CH_4 is the tardier species.

A visual appreciation of the hindrance effect exerted by CO_2 is obtained by observing the animations of MD simulations of mixture diffusion in DDR, CHA, ERI, and LTA [31].

From a practical point of view of separation of CO_2 for mixtures with Ar, N_2 or CH_4 the hindrance by CO_2 for inter-cage hopping of partner molecules in DDR, ERI, and LTA is welcome because this will improve the permeation selectivity in membrane separation processes. We should also expect the predictions of the separation selectivity using the M–S formulation to be overly conservative. In order to verify this conclusion we have re-analysed the experimental data of van den Bergh et al. [2] for permeation of CO_2/CH_4 and N_2/CH_4 mixtures across a DDR membrane; the details of the re-analysis are presented in Supplementary material and the salient results are discussed below.

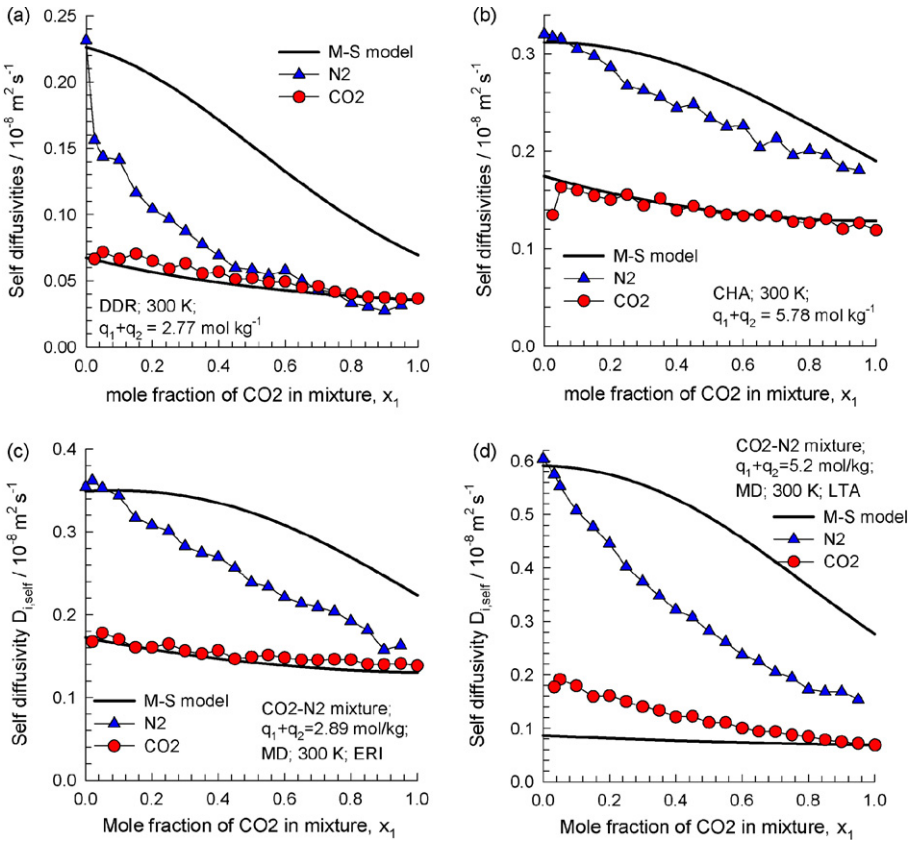

Fig. 7. Self-diffusivities in CO_2/N_2 mixtures in: (a) DDR, (b) CHA, (c) ERI, and (d) LTA at 300 K obtained keeping total mixture loading constant for each zeolite. The continuous solid lines are calculations using Eq. (5).

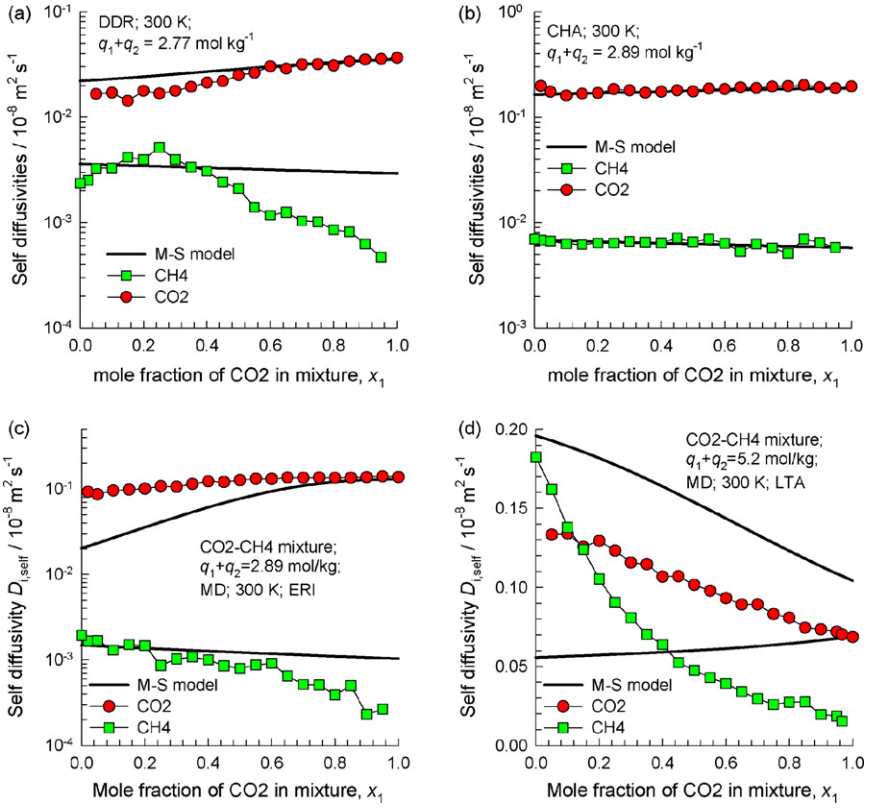

Fig. 8. Self-diffusivities in CO_2/CH_4 mixtures in: (a) DDR, (b) CHA, (c) ERI, and (d) LTA at 300 K obtained keeping total mixture loading constant for each zeolite. The continuous solid lines are calculations using Eq. (5).

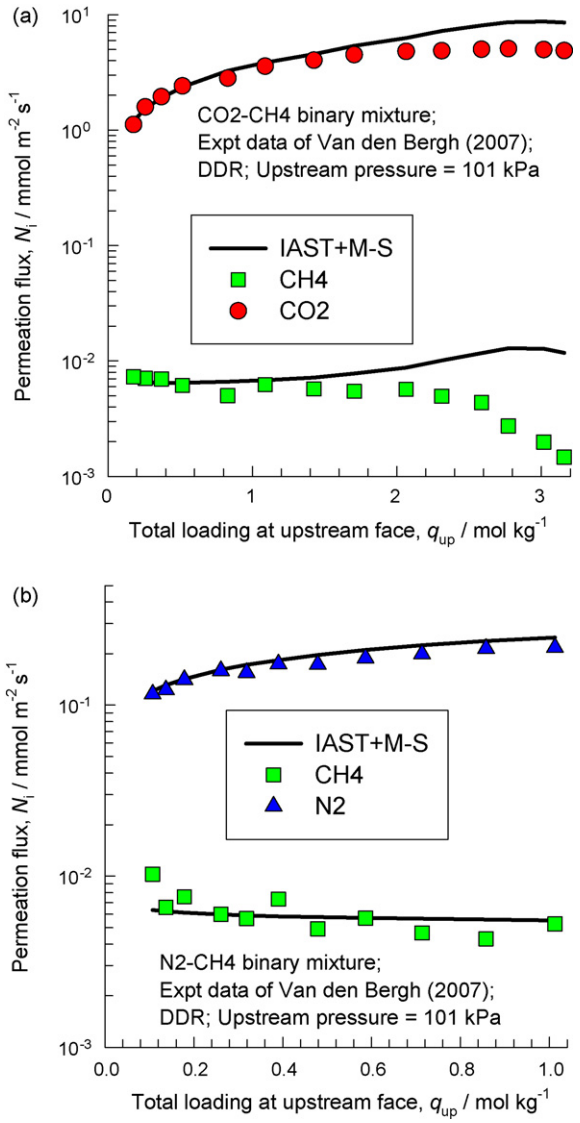

Fig. 9. Component fluxes for: (a) CO_2/CH_4 and (b) N_2/CH_4 binary mixture permeation across DDR membrane, for upstream pressures of 101 kPa. The experimental data of van den Bergh et al. [2] are denoted by filled symbols. The continuous solid lines represent the calculations using the Maxwell–Stefan diffusion model with parameter inputs as specified in Supplementary material accompanying this publication. The IAST is used for calculation of adsorption equilibrium in the mixture.

In Fig. 9a, the experimental fluxes for CO_2/CH_4 mixture permeation are compared with the model predictions based on IAST and the M–S equations. In the campaign shown the total upstream pressure is held constant at 101 kPa and the temperatures are varied; a reduction in temperature leads to a higher total loading of the mixture. At low values of the total mixture loadings, the predictions of the fluxes are in good agreement with experimental values. However, with increased total loadings, the predictions get progressively worse. In particular, we note that the model predictions of CH_4 fluxes are significantly higher than those obtained experimentally. This deviation cannot be ascribed to the failure of the IAST, as witnessed in Figs. 4a and 5a for DDR, because segregation effects will tend to have the effect of increasing the loading of CH_4 even further, causing even worse predictions. The inescapable conclusion is that the failures of the model predictions are due to the hindrance effect of CO_2 at the window regions. A similar conclusion was reached earlier [9] by analysis of the permeation experiments of Himeno et al. [32] across a DDR membrane.

In Fig. 9b, the experimental fluxes for N_2/CH_4 mixture permeation are compared with the model predictions based on IAST and the M–S equations. For this mixture segregation effects are of relatively minor importance and, consequently, the model predictions are in very good agreement with the experimental results over the entire range of loadings.

2.2. Comparison of permeation selectivities

From the GCMC and MD simulation data discussed in the foregoing, we can screen the four cage-type zeolites on the selectivity for permeation across zeolite membranes for (a) CO_2/CH_4, (b) CO_2/N_2, (c) CO_2/Ar, and (d) N_2/CH_4 mixtures. The permeation selectivity is defined by

$$\alpha_{\text{perm}} = \frac{N_1/N_2}{f_1/f_2} \tag{6}$$

For *screening* purposes we consider an equimolar gas mixture in the upstream compartment, i.e. $f_1 = f_2$, take the downstream loadings to be vanishingly small and approximate Eq. (6) by

$$\alpha_{\text{perm}} = \frac{D_{1,\text{self}}}{D_{2,\text{self}}}\frac{q_1}{q_2} = \alpha_{\text{diff}}\alpha_{\text{sorp}} \tag{7}$$

where the sorption selectivity α_{sorp} is defined as the ratio of the molar loadings q_i of species 1 and 2 at the upstream face of the membrane

$$\alpha_{\text{sorp}} = \frac{q_1}{q_2} \tag{8}$$

The diffusion selectivity α_{diff} is the ratio of the self-diffusivities of components 1 and 2, i.e.

$$\alpha_{\text{diff}} = \frac{D_{1,\text{self}}}{D_{2,\text{self}}} \tag{9}$$

MD simulations of the self-diffusivities for equimolar mixtures, $q_1 = q_2$, are reported in Supplementary material.

A combination of the GCMC and MD mixture simulations allows us to estimate α_{perm} values for each zeolite as a function of the total mixture loading. Fig. 10 summarizes the data on permeation selectivity for separation of: (a) CO_2/CH_4, (b) CO_2/N_2, (c) CO_2/Ar, and (d) N_2/CH_4 mixtures across DDR, CHA, ERI, and LTA membranes. For CO_2/CH_4 separation DDR, ERI and CHA offer α_{perm} values in excess of 100, that could be commercially attractive. The precise choice of the zeolite will be dictated by the anticipated operating pressure and loadings within the zeolite. For CO_2/N_2 and CO_2/Ar separations, DDR and CHA are again the best choices. For N_2/CH_4 separation, DDR and ERI offer the highest α_{perm} values. For all four zeolites, LTA has the least α_{perm} value.

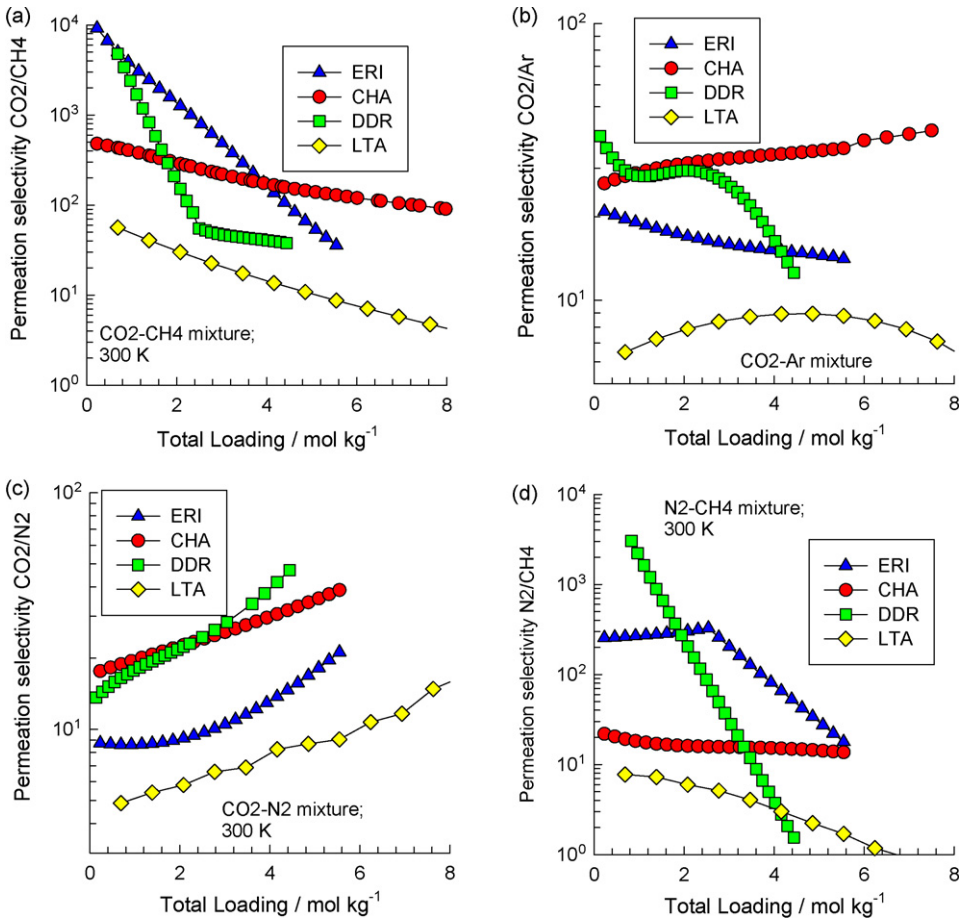

Fig. 10. Permeation selectivity for separation of: (a) CO_2/CH_4, (b) CO_2/N_2, (c) CO_2/Ar, and (d) N_2/CH_4 mixtures across DDR, CHA, ERI, and LTA membranes.

3. Conclusions

GCMC simulations reveal the segregated nature of adsorption of CO_2/CH_4, CO_2/Ar, and CO_2/N_2, mixtures in cage-type zeolites. The window regions of these zeolites has a preponderance of CO_2 molecules. The IAST does not adequately describe the component loadings for CO_2/CH_4 mixture adsorption at high gas phase fugacities. Another important consequence of segregation is that the adsorbed CO_2 molecules at the window regions hinder the inter-cage transport of partner molecules such as CH_4, Ar, and N_2. This hindrance effect is particularly strong for DDR, ERI and LTA zeolites and relatively unimportant for CHA zeolite. Such hindrance effect is not catered for by the Maxwell–Stefan diffusion formulation. This hindrance effect exerted by CO_2 enhances the separation selectivity, making cage-type zeolites particularly attractive for technological use.

From a combination of the GCMC and MD simulation results, DDR and CHA are found to yield the highest permeation selectivities for membrane-based separation of CO_2/CH_4, CO_2/N_2, and CO_2/Ar mixtures.

Acknowledgements

RK and JMvB acknowledge the grant of a TOP subsidy from the Netherlands Foundation for Fundamental Research (NWO-CW) for intensification of reactors.

Appendix A. Supplementary data

Supplementary material associated with this article can be found, in the online version, at doi:10.1016/j.seppur.2007.12.003.

References

[1] S. Li, J.L. Falconer, R.D. Noble, R. Krishna, Interpreting unary, binary and ternary mixture permeation across a SAPO-34 membrane with loading-dependent Maxwell–Stefan diffusivities, J. Phys. Chem. C 111 (2007) 5075–5082.
[2] J. van den Bergh, W. Zhu, J.C. Groen, F. Kapteijn, J.A. Moulijn, K. Yajima, K. Nakayama, T. Tomita, S. Yoshida, Natural gas purification with a DDR zeolite membrane; permeation modelling with Maxwell–Stefan equations, Stud. Surf. Sci. Catal. 170 (2007) 1021–1027.
[3] R. Krishna, J.M. van Baten, E. García-Pérez, S. Calero, Incorporating the loading dependence of the Maxwell–Stefan diffusivity in the modeling of CH_4 and CO_2 permeation across zeolite membranes, Ind. Eng. Chem. Res. 46 (2007) 2974–2986.
[4] S. Himeno, T. Tomita, K. Suzuki, K. Nakayama, S. Yoshida, Synthesis and permeation properties of a DDR-type zeolite membrane for separation of CO_2/CH_4 gaseous mixtures, Ind. Eng. Chem. Res. 46 (2007) 6989–6997.
[5] W. Zhu, P. Hrabanek, L. Gora, F. Kapteijn, J.A. Moulijn, Role of adsorption in the permeation of CH_4 and CO_2 through a silicalite-1 membrane, Ind. Eng. Chem. Res. 45 (2006) 767–776.
[6] M.P. Bernal, J. Coronas, M. Menendez, J. Santamaria, Separation of CO_2/N_2 mixtures using MFI-type zeolite membranes, A.I.Ch.E.J. 50 (2004) 127–135.

[7] Y. Ohta, H. Takaba, S. Nakao, A combinatorial dynamic monte carlo approach to finding a suitable zeolite membrane structure for CO_2/N_2 separation, Microporous Mesoporous Mater. 101 (2007) 319–323.
[8] A.L. Myers, J.M. Prausnitz, Thermodynamics of mixed gas adsorption, A.I.Ch.E.J. 11 (1965) 121–130.
[9] R. Krishna, J.M. van Baten, Influence of segregated adsorption on mixture diffusion in DDR zeolite, Chem. Phys. Lett. 446 (2007) 344–349.
[10] C. Baerlocher, L.B. McCusker, Database of zeolite structures, International Zeolite Association, http://www.iza-structure.org/databases/, 26 June 2001.
[11] E. Jaramillo, S.M. Auerbach, New force field for Na cations in faujasite-type zeolites, J. Phys. Chem. B 103 (1999) 9589–9594.
[12] S. Calero, D. Dubbeldam, R. Krishna, B. Smit, T.J.H. Vlugt, J.F.M. Denayer, J.A. Martens, T.L.M. Maesen, Understanding the role of sodium during adsorption. A force field for alkanes in sodium exchanged faujasites, J. Am. Chem. Soc. 126 (2004) 11377–11386.
[13] J.P. Ryckaert, A. Bellemans, Molecular dynamics of liquid alkanes, Faraday Discuss, Chem. Soc. 66 (1978) 95–106.
[14] D. Frenkel, B. Smit, Understanding molecular simulations: from algorithms to applications, 2nd edition, Academic Press, San Diego, 2002.
[15] D. Dubbeldam, S. Calero, T.J.H. Vlugt, R. Krishna, T.L.M. Maesen, B. Smit, United atom forcefield for alkanes in nanoporous materials, J. Phys. Chem. B 108 (2004) 12301–12313.
[16] J.G. Harris, K.H. Yung, Carbon dioxide's liquid–vapor coexistence curve and critical properties as predicted by a simple molecular model, J. Phys. Chem. 99 (1995) 12021–12024.
[17] C.S. Murthy, K. Singer, M.L. Klein, I.R. McDonald, Pairwise additive effective potentials for nitrogen, Mol. Phys. 41 (1980) 1387–1399.
[18] K. Makrodimitris, G.K. Papadopoulos, D.N. Theodorou, Prediction of permeation properties of CO_2 and N_2 through silicalite via molecular simulations, J. Phys. Chem. B 105 (2001) 777–788.
[19] A.G. Bezus, A.V. Kiselev, A.A. Lopatkin, P.Q. Du, Molecular statistical calculation of the thermodynamic adsorption characteristics of zeolites using the atom–atom approximation. Part 1. Adsorption of methane by zeolite sodium-X, J. Chem. Soc., Faraday Trans. II 74 (1978) 367–379.
[20] A.V. Kiselev, A.A. Lopatkin, A.A. Shul'ga, Molecular statistical calculation of gas adsorption by silicalite, Zeolites 5 (1985) 261–267.
[21] E. García-Pérez, J.B. Parra, C.O. Ania, A. García-Sánchez, J.M. van Baten, R. Krishna, D. Dubbeldam, S. Calero, A computational study of CO_2, N_2 and CH_4 adsorption in zeolites, Adsorption 13 (2007) 469–476.
[22] A.I. Skoulidas, D.S. Sholl, Transport diffusivities of CH_4, CF_4, He, Ne, Ar, Xe, and SF_6 in silicalite from atomistic simulations, J. Phys. Chem. B 106 (2002) 5058–5067.
[23] O. Talu, A.L. Myers, Reference potentials for adsorption of helium, argon, methane and krypton in high-silica zeolites, Colloids Surf. A 187/188 (2001) 83–93.
[24] M. Murthi, R.Q. Snurr, Effects of molecular siting and adsorbent heterogeneity on the ideality of adsorption equilibria, Langmuir 20 (2004) 2489–2497.
[25] R. Krishna, J.M. van Baten, Diffusion of hydrocarbon mixtures in MFI zeolite: influence of intersection blocking, Chem. Eng. J. (2008) DOI:10.1016/j.cej.2007.11.026.
[26] R. Krishna, J.M. van Baten, Insights into diffusion of gases in zeolites gained from molecular dynamics simulations, Microporous Mesoporous Mater. 109 (2008) 91–108.
[27] R. Krishna, S. Li, J.M. van Baten, J.L. Falconer, R.D. Noble, Investigation of slowing-down and speeding-up effects in binary mixture permeation across SAPO-34 and MFI membranes, Sep. Purif. Technol. (2008) DOI:10.1016/j.seppur.2007.08.012.
[28] A.I. Skoulidas, D.S. Sholl, R. Krishna, Correlation effects in diffusion of CH_4/CF_4 mixtures in MFI zeolite. A study linking MD simulations with the Maxwell–Stefan formulation, Langmuir 19 (2003) 7977–7988.
[29] R. Krishna, J.M. van Baten, Diffusion of alkane mixtures in zeolites. Validating the Maxwell–Stefan formulation using MD simulations, J. Phys. Chem. B 109 (2005) 6386–6396.
[30] J.M. van Baten, R. Krishna, Entropy effects in adsorption and diffusion of alkane isomers in mordenite: an investigation using CBMC and MD simulations, Microporous Mesoporous Mater. 84 (2005) 179–191.
[31] J.M. van Baten, R. Krishna, MD animations of diffusion in zeolites, University of Amsterdam, Amsterdam, http://www.science.uva.nl/research/cr/animateMD/, 30 October 2007.
[32] S. Himeno, T. Komatsu, S. Fujita, T. Tomita, K. Suzuki, K. Nakayama, S. Yoshida, CO_2/CH_4 Permeation characteristics of a new type DDR zeolite membrane, Kagaku Kogaku Ronbunshu 33 (2007) 122–129.

-Supplementary material to accompany:

Segregation effects in adsorption of CO_2 containing mixtures and their consequences for separation selectivities in cage-type zeolites

R. Krishna*, J.M. van Baten

Van 't Hoff Institute for Molecular Sciences, University of Amsterdam, Nieuwe Achtergracht 166,

1018 WV Amsterdam, The Netherlands

1. GCMC simulation methodology

Adsorption equilibriua in DDR, CHA, ERI and LTA zeolites were computed using Monte Carlo (MC) simulations in the grand canonical (GC) ensemble. The crystallographic data are available elsewhere.[1] The zeolite lattices are rigid during simulations, with static atomic charges that are assigned by choosing q_{Si} = +2.05 and q_O = -1.025, following the works of Jaramillo and Auerbach [2] and Calero et al.[3]. CH_4 molecules are described with a united atom model, in which each molecule is treated as a single interaction center.[4] CO_2 molecules are taken linear and rigid, with bond length C-O of 1.16Å and partial charges distributed around each molecule to reproduce experimental quadrupole moment. The interaction between adsorbed molecules is described with Coulombic and Lennard-Jones terms. The Coulombic interactions in the system are calculated by Ewald summation for periodic systems[5]. The parameters for CH_4 are taken from Dubbeldam et al[6] and Calero et al.[3]. CO_2 molecules are taken linear and rigid with bond length C–O of 1.16Å according to the 3LJ3CB.EPM2 model developed by Harris and Young [7]. We use the 2LJ3CB.MSKM model for N_2 dumbbell molecules with a rigid interatomic bond of 1.098Å[8, 9]. The partial charges of N_2 and CO_2 are distributed around each molecule to reproduce experimental quadrupole moment. The interactions between adsorbed molecules and the zeolite are dominated by dispersive forces between the pseudo-atoms and the oxygen atoms of the zeolite [10, 11] and the interactions of silicon and aluminium are considered through an effective potential with only the oxygen atoms. The Lennard-Jones parameters for CH_4-zeolite interactions are taken from Dubbeldam et al.[6]. The Lennard-Jones parameters for CO_2-zeolite and N_2-zeolite interactions are essentially those of Makrodimitris et al.[9]. The force fields for Ne and Ar are taken from the paper by Skoulidas and Sholl[12]. The force field for Kr is from Talu and Myers [13]. Table 1 summarizes the information on the force fields for all gases.

The Lennard-Jones potentials are shifted and cut at 12 Å. The number of unit cells in the simulation box was chosen such that the minimum length in each of the coordinate directions was larger than 24 Å. Periodic boundary conditions were employed. Further GCMC simulation details are available in earlier publications[3, 6, 14].

The GCMC simulations were performed using the BIGMAC code developed by T.J.H. Vlugt[15] as basis. The code was modified to handle rigid molecular structures and charges. S. Calero is gratefully acknowledged for her technical inputs in this regard. Detailed validation of the force fields used for CH_4, CO_2, and N_2 is available elsewhere[6, 16].

2. Pure component isotherms fits, probability density plots and segregation data for DDR

The GCMC simulated data for pure component isotherms for CO_2, CH_4, and N_2 in DDR at 220 K, 252 K, 273 K, 300 K, 348 K, and 373 K are presented in Figures 1 and 2. Also shown in Figure 2 are the equilibrium data obtained at constant gas phase fugacities of 101 kPa, 1000 kPa, and 1500 kPa and varying *T*. The isotherm for Ar at 300 K is also presented in Figure 2. The GCMC simulation results, shown by the filled symbols in Figure 1 are in good agreement with the experimental data (open symbols) for CO_2, and CH_4, of Himeno et al. [17, 18], indicated by the open symbols in Figure 1. The continuous solid lines in Figure 1 are 3-site Langmuir fits of the isotherms

$$q = \frac{q_{sat,A} b_A f}{1 + b_A f} + \frac{q_{sat,B} b_B f}{1 + b_B f} + \frac{q_{sat,C} b_C f}{1 + b_C f} \qquad (1)$$

It was found impossible to fit any of the component isotherms with either a 2-site or single site Langmuir model. The 3-site Langmuir fits are "empirical" and the individual sites cannot be identified with specific locations within DDR. In eq. (1) q is the molar loading expressed in mol kg^{-1}, $q_{sat,A}$ is the saturation loading of site A, and f is the fugacity of the bulk gas phase. The values of the fitted *T*-dependent parameters b and q_{sat} are specified in Table 2. These isotherm fits will be used to re-analyse the experimental permeation data of Van den Bergh et al. [19].

DDR consists of cages separated by narrow elliptical shaped windows of 3.6 – 4.4 Å size; for the purposes of quantifying segregation effects we have defined the window region to be a sphere with a diameter of 3 Å, as indicated by the blue spheres in Figure 9.

The GCMC simulations were run for 10^7 cycles. The centers of the molecules were captured every 1000 cycles (starting at cycle 1000). Each cycle performs a number of trial moves that is determined by MAX(20, number of molecules). For low pressures this means 20 moves per cycle, for higher pressures this means the number of trial moves per cycle equals the number of molecules. If the centre of the molecule falls within the blue spheres it is taken as belong to the window region. The total number of molecules within the simulation box was also determined. The percentage of molecules in the windows was calculated by determining the percentage of molecule centers that were within a distance of 1.5 Å from a window center with respect to the total number of captured molecule centers. The remainder of the molecules is taken as belong to the cage region.

The probability density plots for CH_4, Ar, N_2, and CO_2 in DDR at 1 MPa and 273 K are shown in Figures 4, 5, 6 , and 7 respectively.

By summing over the all the 10^4 samples, reliable statistics were obtained for the % probability of adsorbing a molecule within the window region. These % probabilities were determined at both 273 K and 300 K; see the data in Figure 8 for CH_4, Ar, N_2, CO_2, Ne, and Kr. The data appear to correlate with the molecular diameter with a maximum for CO_2. The molecular dimensions are shown in Figure 9.

For adsorption of CO_2/CH_4 and CH_4/N_2 mixtures, with partial fugacities $f_1 = f_2 = 1$ MPa and $T = 273$ K, in DDR the probability density snapshots in Figures 10 and 11 indicate that segregation effects are also present in the mixtures. The mixture segregation data for DDR were obtained a variety of temperatures in the range 223 K- 300K. From these data the sorption selectivities, i.e. the ratio of the loadings of the components in equimolar CO_2/CH_4, N_2/CH_4, CO_2/N_2, and CO_2/Ar mixtures could be determined both within the cages and in the entire pore structure; the data are summarized in Table 4.

GCMC simulations for the component loadings in equilibrium with equimolar CO_2/CH_4, N_2/CH_4, and CO_2/N_2, and CO_2/Ar gas mixtures were determined for a variety of T and partial gas phase fugacities; the simulation data are presented in Figures 12, 13, 14, 15, 16, 17, 18. The continuous solid lines in these Figures represent calculations of the IAST[20] using 3-site Langmuir fits of pure component isotherms with T-dependent parameters b and q_{sat} as specified in Table 2. For CO_2/CH_4 for all

conditions, the IAST underestimates the CH_4 loadings; this is a consequence of segregation effects. For CH_4/N_2 and CO_2/N_2 mixtures, the IAST underestimates the N_2 to a small extent. The reason for this that the degree of segregation of CH_4/N_2, CO_2/N_2 and CO_2/Ar mixtures is much less significant; see data in Table 4. It is to be noted that the IAST predictions of the *total* mixture loading are in excellent agreement with the GCMC mixture simulation results in all cases; this is illustrated in Figure 13.

3. Pure component isotherms fits, probability density plots and segregation data for CHA

The GCMC simulated data for pure component isotherms for CO_2, CH_4, and N_2 in CHA at 273 K and 300 K are presented in Figure 19. The continuous solid lines in Figure 19 are 3-site Langmuir fits of the isotherms. The values of the fitted parameters b and q_{sat} are specified in Table 3.

CHA consists of cages separated by windows of 3.8 Å size; see the framework structure in Figure 20. The probability density plots were also constructed for adsorption of CO_2, CH_4, Ar, and N_2 in CHA at 1 MPa and 300 K; these are shown in Figures 21, 22, 23, and 24. The picture is analogous to that for DDR: we note that no CH_4 molecules are to be detected in the vicinity of the windows, and for Ar, N_2, and CO_2, the window region shows increasing population of molecules. For the purposes of quantifying segregation effects we have defined the window region to be a sphere with a diameter of 3 Å, as indicated by the blue spheres in Figure 20. If the centre of the molecule falls within the blue spheres it is taken as belong to the window region. The remainder of the molecules is taken as belong to the cage region. By summing over the all the 10^4 samples, reliable statistics were obtained for the % probability of adsorbing a molecule within the window region. These % probabilities appear to correlate with the molecular diameter; see Figure 25. The observed trend is similar to that for DDR, with CO_2 displaying the maximum probability for location at the window regions.

One important consequence of non-homogeneous distribution of molecules in CHA is that the IAST will be less successful in predicting the component loadings in the mixture using pure component isotherm fits. For CO_2/CH_4 gas mixtures at 273 K and 300 K mixture the GCMC simulations for the

component loadings in equilibrium are compared the IAST predictions in Figure 26. We note that the IAST under-predicts the loading of the more weakly adsorbed CH_4 in the CO_2/CH_4 mixture. The conventional IAST calculation assumes that CH_4 molecules compete with *all* of the CO_2, making now allowance for segregation. For example, at f = 1 MPa and 300 K, the ratio of the number of molecules of CO_2 to that of CH_4 within the entire CHA pore space is 19.3, whereas within the cage this ratio is 13.3. Put another way, segregation effects reduces the competition faced by CH_4. We also note that the predictions of the IAST become progressively worse with increasing gas phase fugacities.

For CH_4/N_2, CO_2/N_2 and CO_2/Ar mixtures, segregation effects are considerably less significant and the IAST provides a good prediction of the component loadings; see Figures 27, 28, and 29.

4. Pure component isotherms fits and segregation data for ERI

The GCMC simulated data for pure component isotherms for CO_2, CH_4, N_2, and Ar in ERI at 273 K and 300 K are presented in Figure 30. The continuous solid lines in Figure 30 are 3-site Langmuir fits of the isotherms. The values of the fitted parameters b and q_{sat} are specified in Table 3.

ERI consists of cages separated by windows of 3.6 – 5.1 Å size; see the framework structure in Figure 31. For the purposes of quantifying segregation effects we have defined the window region to be a sphere with a diameter of 4 Å, as indicated by the blue spheres in Figure 31. The diameter of the blue spheres is chosen to be slightly higher than that earlier chosen for CHA and DDR because the ellipsoidal window of ERI has a larger major diameter than either CHA or DDR. The % probabilities for locating at the window regions are plotted in Figure 32. The observed trends are similar to that for DDR and CHA. Once again, CO_2 has the maximum probability for location at the window regions.

One important consequence of non-homogeneous distribution of molecules in ERI is that the IAST will be less successful in predicting the component loadings in the mixture using pure component isotherm fits. For CO_2/CH_4 gas mixtures at 273 K and 300 K mixture the GCMC simulations for the component loadings in equilibrium are compared the IAST predictions in Figure 33. We note that the IAST under-predicts the loading of the more weakly adsorbed CH_4 in the CO_2/CH_4 mixture. The

conventional IAST calculation assumes that CH_4 molecules compete with *all* of the CO_2, making now allowance for segregation. For example, at f = 1 MPa and 300 K, the ratio of the number of molecules of CO_2 to that of CH_4 within the entire ERI pore space is 5.4, whereas within the cage this ratio is 3.5. Put another way, segregation effects reduces the competition faced by CH_4. We also note that the predictions of the IAST become progressively worse with increasing gas phase fugacities.

For CH_4/N_2, CO_2/N_2 and CO_2/Ar mixtures, segregation effects are considerably less significant and the IAST provides a good prediction of the component loadings; see Figures 34, 35, and 36.

Generally speaking, segregation effects in ERI appear to be intermediate to those experienced in DDR and CHA.

5. Pure component isotherms fits and segregation data for LTA

The GCMC simulated data for pure component isotherms for CO_2, CH_4, N_2, and Ar in LTA at 300 K are presented in Figure 37. The continuous solid lines in Figure 37 are 3-site Langmuir fits of the isotherms. The values of the fitted parameters b and q_{sat} are specified in Table 3.

LTA consists of cages separated by windows of 4.1 Å size; see the framework structure in Figure 38. For the purposes of quantifying segregation effects we have defined the window region to be a sphere with a diameter of 4 Å, as indicated by the blue spheres in Figure 38. The diameter of the blue spheres is chosen to be slightly higher than that earlier chosen for CHA and DDR. The % probabilities are plotted in Figure 39. The observed trends are similar to that for DDR, CHA, and ERI with CO_2 exhibiting a maximum probability for location at the window regions.

One important consequence of non-homogeneous distribution of molecules in LTA is that the IAST will be less successful in predicting the component loadings in the mixture using pure component isotherm fits. For CO_2/CH_4 gas mixtures at 300 K mixture the GCMC simulations for the component loadings in equilibrium are compared the IAST predictions in Figure 40. We note that the IAST under-predicts the loading of the more weakly adsorbed CH_4 in the CO_2/CH_4 mixture. The conventional IAST calculation assumes that CH_4 molecules compete with *all* of the CO_2, making now allowance for

segregation. For example, at f = 1 MPa and 300 K, the ratio of the number of molecules of CO_2 to that of CH_4 within the entire LTA pore space is 4.8, whereas within the cage this ratio is 2.9. Put another way, segregation effects reduces the competition faced by CH_4. We also note that the predictions of the IAST become progressively worse with increasing gas phase fugacities.

For CH_4/N_2, CO_2/N_2 and CO_2/Ar mixtures, segregation effects are considerably less significant and the IAST provides a good prediction of the component loadings; see Figures 41, 42, and 43.

6. MD simulation methodology

Diffusion is simulated using Newton's equations of motion until the system properties, on average, no longer change in time. The Verlet algorithm is used for time integration. A time step of 1 fs was used in all simulations. For each simulation, *initializing* GCMC moves are used to place the molecules in the domain, minimizing the energy. Next, follows an *equilibration* stage. These are essentially the same as the production cycles, only the statistics are not yet taken into account. This removes any initial large disturbances in the system do not affect statistics. After a fixed number of initialization and equilibrium steps, the MD simulation *production* cycles start. For every cycle, the statistics for determining the mean square displacements (MSDs) are updated. The MSDs are determined for time intervals ranging from 2 fs to 1 ns. In order to do this, an order-N algorithm, as detailed in Chapter 4 of Frenkel and Smit[5] is implemented. The Nosé-Hoover thermostat is applied to all the diffusing particles.

The DLPOLY code[21] was used along with the force field implementation as described in the previous section. DL_POLY is a molecular dynamics simulation package written by W. Smith, T.R. Forester and I.T. Todorov and has been obtained from CCLRCs Daresbury Laboratory via the website.[21]

MD simulations were carried out to determine the diffusivities of both pure components and binary mixtures for a variety of molecular loadings. All simulations were carried out on clusters of PCs equipped with Intel Xeon processors running at 3.4 GHz on the Linux operating system. Each MD simulation, for a specified loading, was run for 120 h, determined to be long enough to obtain reliable

statistics for determination of the diffusivities. Several independent MD simulations were run and the results averaged.

The self-diffusivities, $D_{\mathrm{i,self}}$, were computed by analyzing the mean square displacement of each species i for each of the coordinate directions:

$$D_{i,self} = \frac{1}{2n_i} \lim_{\Delta t \to \infty} \frac{1}{\Delta t} \left\langle \left(\sum_{l=1}^{n_i} \left(\mathbf{r}_{l,i}(t + \Delta t) - \mathbf{r}_{l,i}(t) \right)^2 \right) \right\rangle \tag{2}$$

In this expression n_{i} represents the number of molecules of species i respectively, and $\mathbf{r}_{\mathrm{l,i}}(t)$ is the position of molecule l of species i at any time t. The expression (2) also defines the self-diffusivity in a n-component mixture.

For single component diffusion, the Maxwell-Stefan diffusivity was determined for each of the coordinate directions from

$$Đ_i = \frac{1}{2} \lim_{\Delta t \to \infty} \frac{1}{N_i} \frac{1}{\Delta t} \left\langle \left(\sum_{l=1}^{N_i} \left(\mathbf{r}_{l,i}(t + \Delta t) - \mathbf{r}_{l,i}(t) \right) \right)^2 \right\rangle \tag{3}$$

For DDR and ERI the reported diffusivities are the averages in x- and y- directions $Đ = \left(Đ_x + Đ_y \right)/2$. For CHA and LTA the average values calculated according to $Đ = \left(Đ_x + Đ_y + Đ_z \right)/3$ are presented. In all cases reported here, the MSD values were linear in t for $t > 10$ ps (used in data regression analysis to determine the diffusivities) and we found no evidence of single file diffusion characteristics.

The pure component M-S diffusivities are loading dependent, and we used the Reed and Ehrlich model to quantify this loading dependence [22, 23]. The Reed-Ehrlich parameters are specified in Table 5. The choice of the values for the saturation capacities $q_{\mathrm{i,sat}}$ were guided by GCMC simulations of the pure component isotherms.

The self-exchange coefficient $Đ_{\mathrm{ii}}$ were calculated from

$$Đ_{ii} = \frac{\theta_i}{\frac{1}{D_{i,self}} - \frac{1}{Đ_i}} \tag{4}$$

where θ_i is the fractional occupancy:

$$\theta_i = \frac{q_i}{q_{i,sat}} \tag{5}$$

The self-exchange coefficients for each molecule-zeolite combination was correlated in the form

$$\frac{Đ_{ii}}{Đ_i} = a_i \exp(-b_i \theta_i) \tag{6}$$

The values of a_i, and b_i, are summarized in Table 6.

Using the Maxwell-Stefan diffusion theory, the self-diffusivities in the mixture can be calculated from pure component $Đ_i$ using [23, 24]:

$$D_{1,self} = 1\Bigg/\left(\frac{1}{Đ_1} + \frac{q_1}{q_{1,sat} Đ_{11}} + \frac{q_2}{q_{2,sat} Đ_{12}}\right); \qquad D_{2,self} = 1\Bigg/\left(\frac{1}{Đ_2} + \frac{q_2}{q_{2,sat} Đ_{22}} + \frac{q_1}{q_{1,sat} Đ_{21}}\right) \tag{7}$$

The continuous solid lines in Figures 44, 45, 46, 47, 48, 49, 50, 51, 52, 53, 54, and 55 are obtained from eq. (7). These predictions are compared with the MD simulated values of the self-diffusivities in CO_2/CH_4, CO_2/N_2, CO_2/Ar, N_2/CH_4, CO_2/Ne, and (d) Ar/CH_4 mixtures in these Figures.

A visual indication of the hindrance effect exerted by CO_2 is obtained from animations of MD simulations of mixtures in DDR, CHA, ERI, and LTA[25].

7. Re-analysis of Van den Bergh [19] data for CO_2/CH_4 and N_2/CH_4 permeation across DDR membrane

Van den Bergh et al. [19] have published data for unary permeation of CO_2, CH_4, and N_2 across a DDR membrane for a set of temperatures and pressures. Also presented are data on permeation of binary CO_2/CH_4 and N_2/CH_4 mixtures with equal partial pressures at the upstream face. We re-analyse their experimental data in order to draw some important conclusions regarding the influence of segregation effects on mixture permeation. Our re-analysis of the experimental data makes use of the pure component isotherm 3-site Langmuir fits for CO_2, CH_4, and N_2 in DDR as listed in Table 2. Van

den Bergh et al. [19] have used single-site Langmuir fits of experimental data. Their experimental isotherm data is however restricted to pressures below 120 kPa and saturation was not reached in any set of data. Consequently, they have fitted their isotherms with saturation capacities of 3.4, 1.7, and 1.45 mol kg^{-1} for CO_2, CH_4, and N_2 respectively. These saturation capacities values are too low and, furthermore, they do not have the proper hierarchy. The saturation capacities should follow the trends dictated by the molar volume of the liquid phase, as emphasized by Golden and Sircar[26]. The proper hierarchy is and $N_2 > CO_2 > CH_4$. The low saturation capacities chosen by Van den Bergh et al. [19], coupled with the wrong hierarchy make their modeling of mixture permeation subject to significant errors. Our re-analysis, outlined below, does not suffer from the afore-mentioned limitations.

We begin by developing a model to describe their unary permeation data. For this purpose we use the approach developed in our earlier publication [22]. A brief summary of the approach is given below.

The Reed-Ehrlich model is used to describe the M-S diffusivity as a function of the fractional occupancy, θ_i and temperature, T:

$$Đ_i(T) = Đ_i(0)\exp(-\frac{E_{diff,i}}{RT})\frac{(1+\varepsilon_i)^{z-1}}{(1+\varepsilon_i/\phi_i)^z} \tag{8}$$

where z is the coordination number, representing the maximum number of nearest neighbors within a cage. The parameter $E_{diff,i}$ is the activation energy for diffusion of species i. The value of z is chosen to be 5, as this represents the maximum number of CO_2 molecules within a cage. The choice of this parameter is not crucial because the key parameter ϕ_i is to be fitted empirically in any event. The other parameters are defined as

$$\varepsilon_i = \frac{(\beta_i - 1 + 2\theta_i)\phi_i}{2(1-\theta_i)}; \quad \beta_i = \sqrt{1 - 4\,\theta_i(1-\theta_i)(1-1/\phi_i)} \tag{9}$$

Using the Reed-Ehrlich loading dependence, and a 3-site Langmuir fit for the pure component isotherms we define a modified driving force MDF_i

$$MDF_i \equiv \int_{f_{i,down}}^{f_{i,up}} \frac{(1+\varepsilon_i)^{z-1}}{(1+\varepsilon_i/\phi_i)^z}\frac{q_i}{f_i}df_i = \int_{f_{i,down}}^{f_{i,up}} \frac{(1+\varepsilon_i)^{z-1}}{(1+\varepsilon_i/\phi_i)^z}\left(\frac{q_{i,sat,A}b_{iA}}{1+b_{iA}f_i}+\frac{q_{i,sat,B}b_{iB}}{1+b_{iB}f_i}+\frac{q_{i,sat,C}b_{iC}}{1+b_{iC}f_i}\right)df_i \quad (10)$$

The unary permeation flux at any given T is

$$N_i(T) = \frac{\rho Đ_i(0)}{\delta}\exp(-\frac{E_{diff,i}}{RT})MDF_i \quad (11)$$

It is to be noted that eq (11) assumes each permeation experiment is carried out under isothermal conditions and there is no temperature gradient across the membrane. From the unary permeation data, $\rho Đ_i(0)/\delta$, $E_{\text{diff,i}}$ and ϕ_i can be backed out. The backed-out data are summarized in Table 7. Figure 56 shows the unary permeation data of Van den Bergh et al. [19], along with the calculations following eq (11).

For zeolites that consist of cages, separated by narrow windows, it has been argued that inter-cage hopping of molecules occur practically independent of one another[27]. The Maxwell-Stefan (M-S) diffusion equations simplify to yield a set of *uncoupled* equations

$$N_i = -\rho Đ_i \frac{q_i}{RT}\frac{d\mu_i}{dx}; \quad i = 1,2,...n \quad (12)$$

In the early work of Habgood [28], eq (12) was used to describe N_2/CH_4 mixture diffusion in LTA zeolite and for this reason we shall refer to this simplified variant of the M-S equations as the Habgood model.

For binary mixture permeation across a zeolite membrane of thickness δ, we may integrate eq (12) to obtain

$$N_i(T) = \frac{\rho}{\delta}\int_{upstream}^{downstream} Đ_i(T)\sum_{j=1}^{n}\left(\Gamma_{ij}\frac{dq_j}{dx}\right)dx; \qquad i = 1,2 \quad (13)$$

The details of the numerical procedures for calculation of the fluxes are described in earlier work[29, 30]. In carrying out the integration the loading dependence of $Đ_i$ needs to be properly accounted for using the Reed and Ehrlich approach described in the foregoing.

Let us first consider the prediction of permeation of N_2/CH_4 mixture permeation across the DDR membrane following eq. (13). The experimental data of Van den Bergh et al. [19] obtained at upstream total pressures of 101 kPa, 500 kPa, and 1000 kPa are compared with the calculations following eq. (13) in Figure 57. In these calculations the IAST was used for calculations of the component loadings in the mixture. We note that there is reasonably good agreement for the fluxes of both N_2 and CH_4 with experimental data. This fair agreement is to be ascribed to two factors. First, the IAST provides a good estimate of the component loadings in the mixture, because segregation effects have a relatively minor influence. Secondly, the Habgood approximation of the M-S equations wherein the inter-cage hops are taken to occur independently on one another is also a reasonable one. As discussed earlier, segregation effects are not strong for N_2/CH_4 mixtures in DDR and so both IAST and the M-S diffusion theory work satisfactorily.

An alternative method of plotting the same set of data of Figure 57 is shown in Figure 58, wherein the total mixture loadings at the upstream face, q_{up}, are plotted on the x-axis. The IAST calculations of the *total* mixture loadings are in excellent agreement with the GCMC mixture calculations (cf. Figure 15) and therefore there is no ambiguity in the plots presented in Figure 58.

We now consider the prediction of binary CO_2/CH_4 mixture permeation across the DDR membrane following eq. (13). The experimental data of Van den Bergh et al. [19] obtained at upstream total pressures of 101 kPa, 500 kPa, and 1000 kPa are compared with the calculations following eq. (13) in Figure 59, using the total mixture loading at the upstream face, q_{up}, as x-axis. While the model calculations of CO_2 fluxes are in reasonably good agreement with the experimental data, there are significant deviations of the predictions of the CH_4 from experiment. Let us analyse the reasons behind these deviations. The first candidate for consideration is the use of the IAST. As shown in Figures 12 and 13, the IAST *under*predicts the loading of CH_4 when compared to GCMC simulations. Use of the proper values of the equilibrium loadings for CH_4 using GCMC mixture simulations will only serve to *increase* the deviations of the model calculations from experimental data. The inescapable conclusion is therefore that the assumption that the diffusivity $Đ_i$ for CH_4 in the mixture is the same as that for pure

component (calculated at the same total occupancy, of course) is open to question and debate. The presence of strongly adsorbed CO_2 at the window regions hinder the inter-cage transport of CH_4.

8. Comparison of permeation selectivities of zeolites

From the GCMC and MD simulation data discussed in the foregoing, we can screen the four cage-type zeolites on the selectivity for permeation across zeolite membranes for CO_2/CH_4, N_2/CH_4, CO_2/N_2, and CO_2/Ar mixtures. The permeation selectivity is defined by

$$\alpha_{perm} = \frac{N_1/N_2}{f_1/f_2} \tag{14}$$

For *screening* purposes we consider an equimolar gas mixture in the upstream compartment, i.e. $f_1 = f_2$, take the downstream loadings to be vanishingly small, and approximate eq (14) by

$$\alpha_{perm} = \frac{D_{1,self}}{D_{2,self}}\frac{q_1}{q_2} = \alpha_{diff}\alpha_{sorp} \tag{15}$$

Where the sorption selectivity α_{sorp} is defined as the ratio of the molar loadings q_i of species 1 and 2 at the upstream face of the membrane

$$\alpha_{sorp} = \frac{q_1}{q_2} \tag{16}$$

The diffusion selectivity α_{diff} is the ratio of the self-diffusivities of components 1 and 2, i.e.

$$\alpha_{diff} = \frac{D_{1,self}}{D_{2,self}} \tag{17}$$

MD simulations of the self-diffusivities for equimolar mixtures, $q_1 = q_2$, reported in Figures 44, 45, 46, 47, 48, 49, 50, 51, 52, 53, 54, and 55 are used for this purpose.

Figure 60 summarizes the data on sorption selectivity, diffusion selectivity, and permeation selectivity for separation of CO_2/CH_4, N_2/CH_4, CO_2/N_2, and CO_2/Ar mixtures across DDR, CHA, ERI, and LTA membranes.

9. References

[1] C. Baerlocher, L.B. McCusker, Database of Zeolite Structures, International Zeolite Association, http://www.iza-structure.org/databases/, 26 June 2001.

[2] E. Jaramillo, S.M. Auerbach, New force field for Na cations in faujasite-type zeolites, J. Phys. Chem. B 103 (1999) 9589-9594.

[3] S. Calero, D. Dubbeldam, R. Krishna, B. Smit, T.J.H. Vlugt, J.F.M. Denayer, J.A. Martens, T.L.M. Maesen, Understanding the role of sodium during adsorption. A force field for alkanes in sodium exchanged faujasites, J. Am. Chem. Soc. 126 (2004) 11377-11386.

[4] J.P. Ryckaert, A. Bellemans, Molecular dynamics of liquid alkanes, Faraday Discuss. Chem. Soc. 66 (1978) 95-106.

[5] D. Frenkel, B. Smit, Understanding molecular simulations: from algorithms to applications, Academic Press, 2nd Edition, San Diego, 2002.

[6] D. Dubbeldam, S. Calero, T.J.H. Vlugt, R. Krishna, T.L.M. Maesen, B. Smit, United Atom Forcefield for Alkanes in Nanoporous Materials, J. Phys. Chem. B 108 (2004) 12301-12313.

[7] J.G. Harris, K.H. Yung, Carbon Dioxide's Liquid-Vapor Coexistence Curve And Critical Properties as Predicted by a Simple Molecular Model, J. Phys. Chem. 99 (1995) 12021-12024.

[8] C.S. Murthy, K. Singer, M.L. Klein, I.R. McDonald, Pairwise additive effective potentials for nitrogen, Mol. Phys. 41 (1980) 1387-1399.

[9] K. Makrodimitris, G.K. Papadopoulos, D.N. Theodorou, Prediction of permeation properties of CO_2 and N_2 through silicalite via molecular simulations, J. Phys. Chem. B 105 (2001) 777-788.

[10] A.G. Bezus, A.V. Kiselev, A.A. Lopatkin, P.Q. Du, Molecular statistical calculation of the thermodynamic adsorption characteristics of zeolites using the atom-atom approximation. Part 1. Adsorption of methane by zeolite sodium-X, J.Chem.Soc., Faraday Trans. II 74 (1978) 367-379.

[11] A.V. Kiselev, A.A. Lopatkin, A.A. Shul'ga, Molecular statistical calculation of gas adsorption by silicalite, Zeolites 5 (1985) 261-267.

[12] A.I. Skoulidas, D.S. Sholl, Transport diffusivities of CH_4, CF_4, He, Ne, Ar, Xe, and SF_6 in silicalite from atomistic simulations, J. Phys. Chem. B 106 (2002) 5058-5067.

[13] O. Talu, A.L. Myers, Reference potentials for adsorption of helium, argon, methane and krypton in high-silica zeolites, Colloids Surf., A 187-188 (2001) 83-93.

[14] T.J.H. Vlugt, R. Krishna, B. Smit, Molecular simulations of adsorption isotherms for linear and branched alkanes and their mixtures in silicalite, J. Phys. Chem. B 103 (1999) 1102-1118.

[15] T.J.H. Vlugt, BIGMAC, University of Amsterdam, http://molsim.chem.uva.nl/bigmac/, 1 November 2000.

[16] E. García-Pérez, J.B. Parra, C.O. Ania, A. García-Sánchez, J.M. Van Baten, R. Krishna, D. Dubbeldam, S. Calero, A computational study of CO_2, N_2 and CH_4 adsorption in zeolites, Adsorption 13 (2007) 469-476.

[17] S. Himeno, T. Tomita, K. Suzuki, S. Yoshida, Characterization and selectivity for methane and carbon dioxide adsorption on the all-silica DD3R zeolite, Microporous Mesoporous Mater. 98 (2007) 62-69.

[18] S. Himeno, S. Shimura, S. Sakurai, Light gas adsorption of all-silica DD3R zeolite: Computational and experimental investigation, 9th International Conference on Fundamentals of Adsorption, Giardini Naxos, Sicily, Italy, 2007.

[19] J. van den Bergh, W. Zhu, J.C. Groen, F. Kapteijn, J.A. Moulijn, K. Yajima, K. Nakayama, T. Tomita, S. Yoshida, Natural Gas Purification with a DDR Zeolite Membrane; Permeation Modelling with Maxwell-Stefan Equations, Stud. Surf. Sci. Catal. 170 (2007) 1021-1027.

[20] A.L. Myers, J.M. Prausnitz, Thermodynamics of mixed gas adsorption, A.I.Ch.E.J. 11 (1965) 121-130.
[21] W. Smith, T.R. Forester, I.T. Todorov, The DL_POLY Molecular Simulation Package, Warrington, England, http://www.cse.clrc.ac.uk/msi/software/DL_POLY/index.shtml, March 2006.
[22] R. Krishna, J.M. van Baten, E. García-Pérez, S. Calero, Incorporating the loading dependence of the Maxwell-Stefan diffusivity in the modeling of CH_4 and CO_2 permeation across zeolite membranes, Ind. Eng. Chem. Res. 46 (2007) 2974-2986.
[23] R. Krishna, J.M. van Baten, Insights into diffusion of gases in zeolites gained from molecular dynamics simulations, Microporous Mesoporous Mater. (2007) DOI:10.1016/j.micromeso.2007.04.036
[24] R. Krishna, J.M. van Baten, Diffusion of alkane mixtures in zeolites. Validating the Maxwell-Stefan formulation using MD simulations, J. Phys. Chem. B 109 (2005) 6386-6396.
[25] J.M. van Baten, R. Krishna, MD animations of diffusion in zeolites, University of Amsterdam, Amsterdam, http://www.science.uva.nl/research/cr/animateMD/, 30 October 2007.
[26] T.C. Golden, S. Sircar, Gas Adsorption on Silicalite, J. Colloid Interface Sci. 162 (1994) 182-188.
[27] R. Krishna, J.M. van Baten, E. García-Pérez, S. Calero, Diffusion of CH_4 and CO_2 in MFI, CHA and DDR zeolites, Chem. Phys. Lett. 429 (2006) 219-224.
[28] H.W. Habgood, The kinetics of molecular sieve action. Sorption of nitrogen-methane mixtures by Linde molecular sieve 4A, Canad. J. Chem. 36 (1958) 1384-1397.
[29] R. Krishna, R. Baur, Modelling issues in zeolite based separation processes, Sep. Purif. Technol. 33 (2003) 213-254.
[30] R. Krishna, R. Baur, Diffusion, Adsorption and Reaction in Zeolites: Modelling and Numerical Issues, University of Amsterdam, Amsterdam, http://www.science.uva.nl/research/cr/zeolite/, 11 November 2004.

Table 1. Summary of force field used in GCMC and MD simulations

The interaction between adsorbates was calculated using Lennard-Jones potentials and electrostatic interactions using an Ewald summation method. For adsorbate-adsorbate interactions, Lorentz-Berthelot mixing rules were applied for σ and ε/k_B. Leonard-Jones interaction with the zeolite was only taken σ and ε/k_B and epsilon for the adsorbates and for the interaction with the adsorbates and with the zeolites. The charges are also shown for the pseudo atoms.

(pseudo-) atom	Atom-atom σ / Å	Atom-atom ε/k_B / K	Atom - O in zeolite σ / Å	Atom - O in zeolite ε/k_B / K	charge
CH_4	3.72	158.5	3.47	115	0
C (CO_2)	2.757	28.129	2.7815	50.2	0.6512
O (CO_2)	3.033	80.507	2.9195	84.93	-0.3256
N (N_2)	3.32	36.4	3.06	58.25	-0.40484
Ar	3.42	124.07	3.17	95.61	0
Ne	2.789	35.7	2.798	56.87	0
Kr	3.636	166.4	3.45	109.6	0
Ar	3.42	124.07	3.17	95.61	0

The molecule geometries were fixed. The bond angle for CO_2 is 180°. For N_2, a point charge is located in the middle between the two atoms, that is twice the magnitude of the charges on N, and opposite in sign, so that the total molecule charge is zero. The following table shows the bond lengths that were used:

bond	bond length / Å
N-N (N_2)	1.098
C-O (CO_2)	1.16

The zeolite atoms are considered immobile. The following table shows the charges used for the zeolite atoms:

atom	charge
$O_{Zeolite}$	-1.025
$Si_{Zeolite}$	2.05

Table 2. Temperature dependent 3-site Langmuir parameters for DDR

$$q = \frac{q_{sat,A} b_A f}{1 + b_A f} + \frac{q_{sat,B} b_B f}{1 + b_B f} + \frac{q_{sat,C} b_C f}{1 + b_C f}$$

For CO_2: $b_A = 7.8 \times 10^{-11} \exp(\frac{3400}{T})$; $q_{sat,A} = 3.0$ mol/kg ;

$b_B = 2 \times 10^{-13} \exp(\frac{3800}{T})$; $q_{sat,B} = 1.0$ mol/kg ; $b_C = 1.9 \times 10^{-14} \exp(\frac{3450}{T})$; $q_{sat,C} = 0.6$ mol/kg

For CH_4: $b_A = 2.39 \times 10^{-9} \exp(\frac{2200}{T})$; $q_{sat,A} = 1.6$ mol/kg ;

$b_B = 1.24 \times 10^{-11} \exp(\frac{2200}{T})$; $q_{sat,B} = 1.6$ mol/kg ; $b_C = 1.27 \times 10^{-12} \exp(\frac{1000}{T})$; $q_{sat,C} = 1.0$ mol/kg

For N_2: $b_A = 1.57 \times 10^{-9} \exp(\frac{1650}{T})$; $q_{sat,A} = 1.8$ mol/kg ;

$b_B = 4.5 \times 10^{-11} \exp(\frac{1650}{T})$; $q_{sat,B} = 1.8$ mol/kg ; $b_C = 3 \times 10^{-13} \exp(\frac{1650}{T})$; $q_{sat,C} = 1.8$ mol/kg

For Ar: $b_A = 2.065 \times 10^{-9} \exp(\frac{1500}{T})$; $q_{sat,A} = 2.1$ mol/kg ;

$b_B = 2.5 \times 10^{-9} \exp(\frac{700}{T})$; $q_{sat,B} = 1.3$ mol/kg ; $b_C = 1.08 \times 10^{-10} \exp(\frac{700}{T})$; $q_{sat,C} = 2$ mol/kg

Table 3. Three-site Langmuir parameters for pure component isotherms in CHA , ERI, and LTA. The saturation capacity, q_{sat}, has the units of mol kg^{-1}. The Langmuir parameters, b, have the units of Pa^{-1}.

Zeolite	Molecule	Temperature, T/K	Three-Site Langmuir parameters					
			b_A	$q_{sat,A}$	b_B	$q_{sat,B}$	b_C	$q_{sat,C}$
CHA	CO_2	273	1.61×10^{-5}	7	1.81×10^{-7}	1.9	5.11×10^{-9}	1.3
CHA	CH_4	273	2.89×10^{-6}	2.9	1.32×10^{-8}	4.3	2.21×10^{-7}	1.12
CHA	N_2	273	3.06×10^{-7}	4.6	1.1×10^{-8}	3.5	7.57×10^{-12}	2.1
CHA	CO_2	300	5.2×10^{-6}	7	4.64×10^{-8}	1.9	1.48×10^{-9}	1.3
CHA	CH_4	300	1.6×10^{-6}	2.9	2.24×10^{-8}	4.3	5.58×10^{-10}	1.12
CHA	N_2	300	2.06×10^{-7}	4.6	5.54×10^{-9}	3.5	9.3×10^{-12}	2.1
CHA	Ar	300	1.89×10^{-7}	3.5	4.65×10^{-8}	3.5	8.81×10^{-10}	3.2
ERI	CO_2	273	9.34×10^{-6}	5.4	4.71×10^{-8}	1.7	3.73×10^{-10}	1.2
ERI	CH_4	273	4.42×10^{-6}	2.7	2.05×10^{-8}	2.7	5.3×10^{-11}	1.5
ERI	N_2	273	7.27×10^{-7}	3.5	4.56×10^{-9}	3.2	4.81×10^{-12}	1.7
ERI	CO_2	300	3.46×10^{-6}	5.4	1.47×10^{-8}	1.7	9.19×10^{-11}	1.2
ERI	CH_4	300	1.97×10^{-6}	2.7	1.12×10^{-8}	2.7	4×10^{-11}	1.5
ERI	N_2	300	4.31×10^{-7}	3.5	2.67×10^{-9}	3.2	3.49×10^{-12}	1.7
ERI	Ar	300	1.62×10^{-7}	5	4.05×10^{-9}	2	1.26×10^{-10}	2
LTA	CO_2	300	1.08×10^{-6}	8	6.58×10^{-10}	2.3	-	-
LTA	CH_4	300	4.09×10^{-7}	5.4	6.98×10^{-9}	3	1.85×10^{-10}	1.8
LTA	N_2	300	1.36×10^{-7}	4.5	8.27×10^{-9}	4.5	2.78×10^{-11}	2
LTA	Ar	300	7.32×10^{-8}	8.8	4.4×10^{-10}	3.7	-	-

Table 4. Selectivity in mixtures, determined from the statistics on location of molecules within cages only, and within the entire pore structure of DDR, CHA, ERI, and LTA. The data obtained for equimolar binary mixtures at partial fugacities of 1 MPa.

Zeolite	Temperature/K	Mixture	Selectivity within cages	Selectivity in total pore structure
DDR	223	CO_2/CH_4	18.6	27.7
DDR	273	CO_2/CH_4	4.3	7.2
DDR	300	CO_2/CH_4	2.9	5
DDR	223	CH_4/N_2	9.1	6.1
DDR	273	CH_4/N_2	7.6	6.5
DDR	300	CH_4/N_2	6.6	5.9
DDR	300	CO_2/N_2	23.2	36.1
DDR	300	CO_2/Ar	18.8	29.3
CHA	300	CO_2/CH_4	13.3	19.3
CHA	300	CH_4/N_2	4.7	4.2
CHA	300	CO_2/N_2	62	74
CHA	300	CO_2/Ar	51	59
ERI	300	CO_2/CH_4	3.5	5.4
ERI	300	CH_4/N_2	3.9	3.7
ERI	300	CO_2/N_2	14.9	21.5
ERI	300	CO_2/Ar	16.5	22
LTA	300	CO_2/CH_4	2.9	4.8
LTA	300	CH_4/N_2	3.9	3.5
LTA	300	CO_2/N_2	14.5	21.5
LTA	300	CO_2/Ar	11.4	17

Table 5. Reed-Ehrlich parameters for a variety of molecules in DDR, CHA, ERI, and LTA zeolites.

Zeolite	Molecule	Saturation capacity, $q_{i,sat}$ / mol/kg	$Đ_i(0)$ / 10^{-8} m^2 s^{-1}	z	ϕ_i
CHA	CO_2	9.71	0.21	5	1.47
CHA	N_2	9.71	0.35	5	$2.11\exp(-0.34\theta_i)$
CHA	Ar	9.71	0.285	5	1.64
CHA	Ne	27.7	1.74	5	1.31
CHA	CH_4	8.32	2.1×10^{-3}	5	$4.55\exp(-0.98\theta_i)$
DDR	Ne	14	1.1	5	$1.46\exp(-0.2\theta_i)$
DDR	CO_2	4.6	0.113	5	1.2
DDR	N_2	5.4	0.16	5	$3.7\exp(-0.95\theta_i)$
DDR	Ar	5.4	0.075	5	$3.5\exp(-0.74\theta_i)$
DDR	CH_4	4.2	4.76×10^{-5}	5	$6\exp(-0.2\theta_i)$
ERI	CO_2	8	0.14	5	$1.75\exp(-0.07\theta_i)$
ERI	N_2	9	0.19	5	$3.4\exp(-0.7\theta_i)$
ERI	Ar	5.5	0.14	5	$2.7\exp(-0.4\theta_i)$
ERI	Ne	22	1.4	5	$1.43\exp(-0.18\theta_i)$
ERI	CH_4	4.16	1.25×10^{-4}	5	$8.8\exp(-0.53\theta_i)$
LTA	CO_2	12	0.4	5	$0.75\exp(-0.5\theta_i)$
LTA	N_2	12.5	0.8	5	$1.5\exp(-0.15\theta_i)$
LTA	Ar	12.5	0.58	5	1.5
LTA	Ne	35	1.83	5	1.22
LTA	CH_4	4.16	0.018	5	$5.9\exp(-0.64\theta_i)$

Table 6. Correlation parameters a_i and b_i describing self-exchange coefficients $Đ_{ii}$ defined by Eq. (4) for a variety of molecules in DDR, CHA, ERI, and LTA zeolites, determined from MD simulations of pure component $Đ_i$ and $D_{i,self}$.

Zeolite	Molecule	a_i	b_i
CHA	CO_2	1.5	1.3
CHA	N_2	3.2	2.7
CHA	Ar	2.6	1.6
CHA	Ne	0.7	1.3
CHA	CH_4	5	0
DDR	Ne	1	2.5
DDR	CO_2	1.6	1.7
DDR	N_2	3.2	4
DDR	Ar	4	3
DDR	CH_4	5	0
ERI	CO_2	1	1.4
ERI	N_2	1.5	1.5
ERI	Ar	4.5	3
ERI	Ne	0.65	0
ERI	CH_4	5	0
LTA	CO_2	2	0
LTA	N_2	2	2.1
LTA	Ar	2.4	2
LTA	Ne	0.65	1.7
LTA	CH_4	20	4

Table 7. Unary permeation parameters for DDR membrane backed out from the data of Van den Bergh et al.[22].

Molecule	$\rho \text{Đ}_i(0)/\delta$ 10^{-3} kg m^{-2} s^{-1}	$E_{\text{diff,i}}$ kJ mol^{-1}	ϕ_i	z
CO_2	933	13.63	$1.5\exp(0.4\theta_i)$	5
CH_4	50	19.54	$6\exp(0.25\theta_i)$	5
N_2	123	8.06	$1.7\exp(0.6\theta_i)$	5

10. Captions for Figures

Figure 1. Pure component isotherm data for CO_2, CH_4 and N_2 in DDR at 220 K, 252 K, 273 K, 300 K, and 348 K. The filled symbols are GCMC simulation results. The open symbols are experimental data of Himeno et al.[17, 18]. The continuous solid lines are 3-site Langmuir fits with T-dependent parameters b and q_{sat} as specified in Table 2.

Figure 2. Pure component isotherm data for CO_2, CH_4 and N_2 in DDR at 373 K. Also shown is equilibrium data for pure Ar at 300 K, and for pure CO_2, CH_4 and N_2 at constant gas phase fugacities of 101 kPa, 1000 kPa, and 1500 kPa, and varying T. The filled symbols are GCMC simulation results. The open symbols are experimental data of Himeno et al.[17, 18]. The continuous solid lines are 3-site Langmuir fits with T-dependent parameters b and q_{sat} as specified in Table 2.

Figure 3. Framework structure of DDR, top and side views. The blue spheres of 3 Å diameter are taken to indicate the window region.

Figure 4. Probability density plots for locations of CH_4 in DDR at bulk gas pressure of 1 MPa and T = 273 K.

Figure 5. Probability density plots for locations of Ar in DDR at bulk gas pressure of 1 MPa and $T = 273$ K.

Figure 6. Probability density plots for locations of N_2 in DDR at bulk gas pressure of 1 MPa and $T = 273$ K.

Figure 7. Probability density plots for locations of CO_2 in DDR at bulk gas pressure of 1 MPa and $T = 273$ K.

Figure 8. %Probability for adsorption of component in the window region of DDR as function of the molecular diameter for CH_4, Ar, N_2, CO_2, Ne, and Kr at 273 K and 300 K.

Figure 9. Cartoon showing the approximate molecular dimensions of Ne, Ar, Kr, N_2, CO_2, and CH_4. The molecular diameters are estimated on the basis of the Lennard-Jones size parameters σ for molecule-molecule interactions. The molecular lengths are estimated on the basis of the bond lengths.

Figure 10. Probability density plots for CO_2/CH_4 mixtures in DDR obtained with partial fugacities $f_1 = f_2 = 1$ MPa and $T = 273$ K.

Figure 11. Probability density plots for N_2/CH_4 mixtures in DDR obtained with partial fugacities $f_1 = f_2 = 1$ MPa and $T = 273$ K.

Figure 12. GCMC simulations for the component loadings in equilibrium with equimolar CO_2/CH_4 gas mixtures in DDR at 223 K, 273 K, 300 K, and 373 K. The continuous solid lines represent calculations of the IAST[20] using 3-site Langmuir fits of pure component isotherms with *T*-dependent parameters *b* and q_{sat} as specified in Table 2.

Figure 13. GCMC simulations for the component loadings in equilibrium with equimolar CO_2/CH_4 gas mixtures in DDR at partial gas phase fugacities of 50.5 kPa, 250 kPa, and 500 kPa and varying *T*. The continuous solid lines represent calculations of the IAST[20] using 3-site Langmuir fits of pure component isotherms with *T*-dependent parameters *b* and q_{sat} as specified in Table 2.

Figure 14. GCMC simulations for the component loadings in equilibrium with equimolar N_2/CH_4 gas mixtures in DDR at 223 K, 273 K, and 300 K. The continuous solid lines represent calculations of the IAST[20] using 3-site Langmuir fits of pure component isotherms with *T*-dependent parameters *b* and q_{sat} as specified in Table 2.

Figure 15. GCMC simulations for the component loadings in equilibrium with equimolar N_2/CH_4 gas mixtures in DDR at partial gas phase fugacities of 50.5 kPa, 250 kPa, and 500 kPa and varying *T*. The continuous solid lines represent calculations of the IAST[20] using 3-site Langmuir fits of pure component isotherms with *T*-dependent parameters *b* and q_{sat} as specified in Table 2.

Figure 16. GCMC simulations for the component loadings in equilibrium with equimolar CO_2/N_2 gas mixtures in DDR at 300 K. The continuous solid lines represent calculations of the IAST[20] using 3-site Langmuir fits of pure component isotherms with *T*-dependent parameters *b* and q_{sat} as specified in Table 2.

Figure 17. GCMC simulations for the component loadings in equilibrium with equimolar CO_2/N_2 gas mixtures in DDR at partial gas phase fugacities of 50.5 kPa, 250 kPa, and 500 kPa and varying *T*. The continuous solid lines represent calculations of the IAST[20] using 3-site Langmuir fits of pure component isotherms with *T*-dependent parameters *b* and q_{sat} as specified in Table 2.

Figure 18. GCMC simulations for the component loadings in equilibrium with equimolar CO_2/Ar gas mixtures in DDR at 300 K. The continuous solid lines represent calculations of the IAST[20] using 3-site Langmuir fits of pure component isotherms with *T*-dependent parameters *b* and q_{sat} as specified in Table 2.

Figure 19. Pure component isotherm data for CO_2, CH_4 and N_2 in CHA at 273 K and 300 K. The filled symbols are GCMC simulation results. The continuous solid lines are 3-site Langmuir fits with parameters specified in Table 3.

Figure 20. Framework structure of CHA, top and side views. The blue spheres of 3 Å diameter are taken to indicate the window region.

Figure 21. Probability density plots for locations of CH_4 in CHA at total bulk gas pressure of 1 MPa and $T = 300$ K.

Figure 22. Probability density plots for locations of Ar in CHA at total bulk gas pressure of 1 MPa and $T = 300$ K.

Figure 23. Probability density plots for locations of N_2 in CHA at total bulk gas pressure of 1 MPa and $T = 300$ K.

Figure 24. Probability density plots for locations of CO_2 in CHA at total bulk gas pressure of 1 MPa and T = 300 K.

Figure 25. %Probability for adsorption of component in the window region of CHA as function of the molecular diameter of CH_4, Ar, N_2, CO_2, Ne, and Kr.

Figure 26. GCMC simulations for the component loadings in equilibrium with equimolar CO_2/CH_4, gas mixtures in CHA at 273 K and 300 K. The continuous solid lines represent calculations of the IAST[20] using 3-site Langmuir fits of pure component isotherms with fitted parameter values as given in Table 3.

Figure 27. GCMC simulations for the component loadings in equilibrium with equimolar N_2/CH_4 gas mixtures in CHA at 300 K. The continuous solid lines represent calculations of the IAST[20] using 3-site Langmuir fits of pure component isotherms with fitted parameter values as given in Table 3.

Figure 28. GCMC simulations for the component loadings in equilibrium with equimolar CO_2/N_2 gas mixtures in CHA at 300 K. The continuous solid lines represent calculations of the IAST[20] using 3-site Langmuir fits of pure component isotherms with fitted parameter values as given in Table 3.

Figure 29. GCMC simulations for the component loadings in equilibrium with equimolar CO_2/Ar gas mixtures in CHA at 300 K. The continuous solid lines represent calculations of the IAST[20] using 3-site Langmuir fits of pure component isotherms with fitted parameter values as given in Table 3.

Figure 30. Pure component isotherm data for CO_2, CH_4, Ar, and N_2 in ERI at 273 K, and 300 K. The filled symbols are GCMC simulation results. The continuous solid lines are 3-site Langmuir fits with parameters specified in Table 3.

Figure 31. Framework structure of ERI. The blue spheres of 4 Å diameter are taken to indicate the window region.

Figure 32. %Probability for adsorption of component in the window region of ERI as function of the molecular diameter of CH_4, Ar, N_2, CO_2, Ne, and Kr.

Figure 33. GCMC simulations for the component loadings in equilibrium with equimolar CO_2/CH_4, gas mixtures in ERI at 273 K and 300 K. The continuous solid lines represent calculations of the IAST[20] using 3-site Langmuir fits of pure component isotherms with fitted parameter values as given in Table 3.

Figure 34. GCMC simulations for the component loadings in equilibrium with equimolar N_2/CH_4 gas mixtures in ERI at 300 K. The continuous solid lines represent calculations of the IAST[20] using 3-site Langmuir fits of pure component isotherms with fitted parameter values as given in Table 3.

Figure 35. GCMC simulations for the component loadings in equilibrium with equimolar CO_2/N_2 gas mixtures in ERI at 300 K. The continuous solid lines represent calculations of the IAST[20] using 3-site Langmuir fits of pure component isotherms with fitted parameter values as given in Table 3.

Figure 36. GCMC simulations for the component loadings in equilibrium with equimolar CO_2/Ar gas mixtures in ERI at 300 K. The continuous solid lines represent calculations of the IAST[20] using 3-site Langmuir fits of pure component isotherms with fitted parameter values as given in Table 3.

Figure 37. Pure component isotherm data for CO_2, CH_4, Ar, and N_2 in LTA at 300 K. The filled symbols are GCMC simulation results. The continuous solid lines are 3-site Langmuir fits with parameters specified in Table 3.

Figure 38. Framework structure of LTA. The blue spheres of 4 Å diameter are taken to indicate the window region.

Figure 39. %Probability for adsorption of component in the window region of LTA as function of the molecular diameter of CH_4, Ar, N_2, CO_2, Ne, and Kr.

Figure 40. GCMC simulations for the component loadings in equilibrium with equimolar CO_2/CH_4, gas mixtures in LTA at 300 K. The continuous solid lines represent calculations of the IAST[20] using 3-site Langmuir fits of pure component isotherms with fitted parameter values as given in Table 3.

Figure 41. GCMC simulations for the component loadings in equilibrium with equimolar N_2/CH_4 gas mixtures in LTA at 300 K. The continuous solid lines represent calculations of the IAST[20] using 3-site Langmuir fits of pure component isotherms with fitted parameter values as given in Table 3.

Figure 42. GCMC simulations for the component loadings in equilibrium with equimolar CO_2/N_2 gas mixtures in LTA at 300 K. The continuous solid lines represent calculations of the IAST[20] using 3-site Langmuir fits of pure component isotherms with fitted parameter values as given in Table 3.

Figure 43. GCMC simulations for the component loadings in equilibrium with equimolar CO_2/Ar gas mixtures in LTA at 300 K. The continuous solid lines represent calculations of the IAST[20] using 3-site Langmuir fits of pure component isotherms with fitted parameter values as given in Table 3.

Figure 44. MD simulations of self-diffusivities in CO_2/CH_4 and CO_2/N_2 gas mixtures in DDR at 300 K.

Figure 45. MD simulations of self-diffusivities in CO_2/Ar and CH_4/N_2 gas mixtures in DDR at 300 K.

Figure 46. MD simulations of self-diffusivities in CO_2/Ne and CH_4/Ar gas mixtures in DDR at 300 K.

Figure 47. MD simulations of self-diffusivities in CO_2/CH_4 and CO_2/N_2 gas mixtures in CHA at 300 K.

Figure 48. MD simulations of self-diffusivities in CO_2/Ar and CH_4/N_2 gas mixtures in CHA at 300 K.

Figure 49. MD simulations of self-diffusivities in CO_2/Ne and CH_4/Ar mixtures in CHA at 300 K.

Figure 50. MD simulations of self-diffusivities in CO_2/CH_4 and CO_2/N_2 gas mixtures in ERI at 300 K.

Figure 51. MD simulations of self-diffusivities in CO_2/Ar and CH_4/N_2 gas mixtures in ERI at 300 K.

Figure 52. MD simulations of self-diffusivities in CO_2/Ne and CH_4/Ar mixtures in ERI at 300 K.

Figure 53. MD simulations of self-diffusivities in CO_2/CH_4 and CO_2/N_2 gas mixtures in LTA at 300 K.

Figure 54. MD simulations of self-diffusivities in CO_2/Ar and CH_4/N_2 gas mixtures in LTA at 300 K.

Figure 55. MD simulations of self-diffusivities in CO_2/Ne and CH_4/Ar mixtures in LTA at 300 K.

Figure 56. Unary permeation fluxes of CO_2, CH_4, and N_2 across a DDR membrane at specified upstream pressures and varying *T*. The experimental data of Van den Bergh et al. [19] are denoted by filled symbols. The continuous solid lines represent the model calculations using eq. (11). Further data inputs are as given in Table 2 and Table 7.

Figure 57. Component fluxes for binary N_2/CH_4 mixture permeation across DDR membrane, for upstream pressures of 101 kPa, 500 kPa, and 1000 kPa. The experimental data of Van den Bergh et al. [19] are denoted by filled symbols. The continuous solid lines represent the model calculations using eq. (13). Further data inputs are as given in Table 2 and Table 7. The IAST is used for calculation of adsorption equilibrium in the mixture.

Figure 58. This contains the same information as in Figure 57 with the total mixture loading plotted on the x-axes.

Figure 59. Component fluxes for binary CO_2/CH_4 mixture permeation across DDR membrane, for upstream pressures of 101 kPa, 500 kPa, and 1000 kPa. The experimental data of Van den Bergh et al. [19] are denoted by filled symbols. The continuous solid lines represent the model calculations using eq. (13). Further data inputs are as given in Table 2 and Table 7. The IAST is used for calculation of adsorption equilibrium in the mixture.

Figure 60. Sorption selectivity, diffusion selectivity, and permeation selectivity for separation of CO_2/CH_4, N_2/CH_4, CO_2/N_2, and CO_2/Ar mixtures across DDR, CHA, ERI, and LTA membranes.

Figure 1

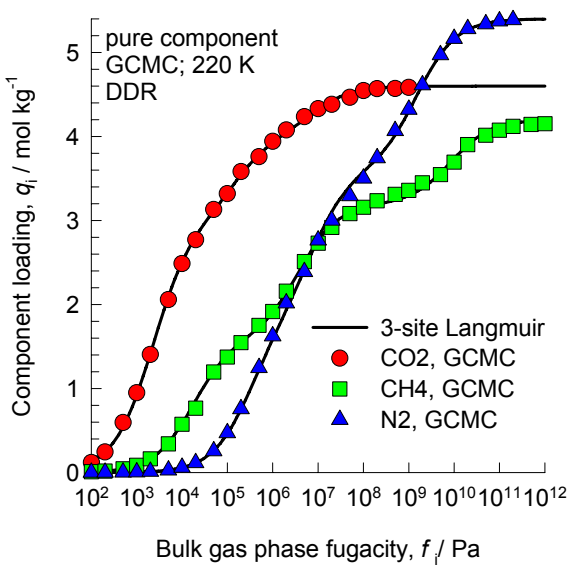
pure component
GCMC; 220 K
DDR
3-site Langmuir
CO2, GCMC
CH4, GCMC
N2, GCMC
Component loading, q_i / mol kg^{-1}
Bulk gas phase fugacity, f_i / Pa

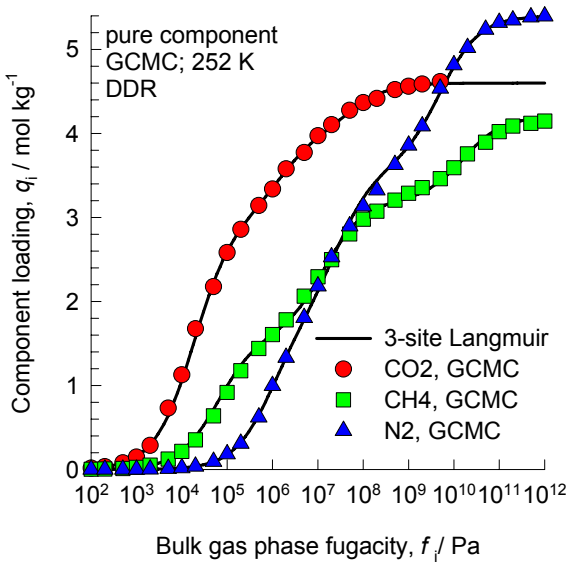
pure component
GCMC; 252 K
DDR
3-site Langmuir
CO2, GCMC
CH4, GCMC
N2, GCMC
Component loading, q_i / mol kg^{-1}
Bulk gas phase fugacity, f_i / Pa

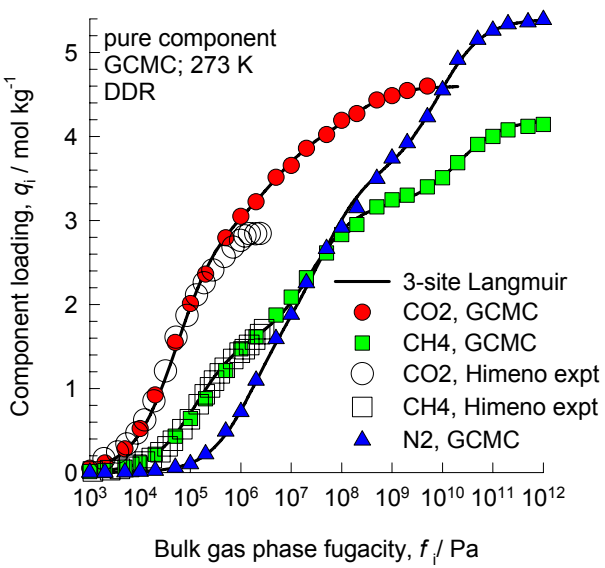
pure component
GCMC; 273 K
DDR
3-site Langmuir
CO2, GCMC
CH4, GCMC
CO2, Himeno expt
CH4, Himeno expt
N2, GCMC
Component loading, q_i / mol kg^{-1}
Bulk gas phase fugacity, f_i / Pa

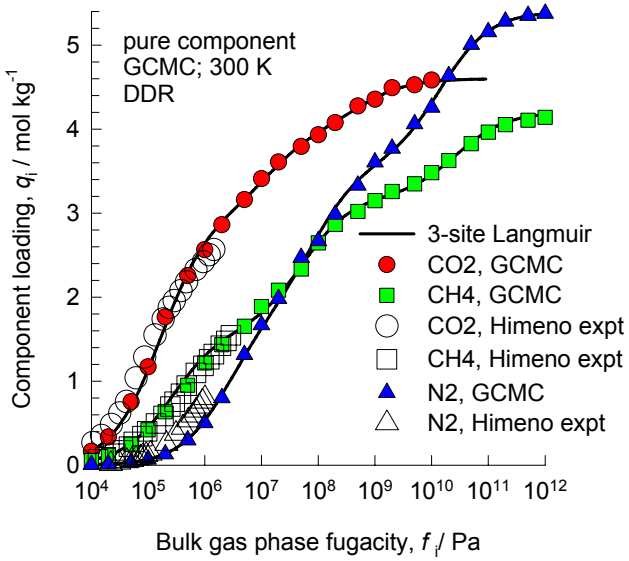
pure component
GCMC; 300 K
DDR
3-site Langmuir
CO2, GCMC
CH4, GCMC
CO2, Himeno expt
CH4, Himeno expt
N2, GCMC
N2, Himeno expt
Component loading, q_i / mol kg^{-1}
Bulk gas phase fugacity, f_i / Pa

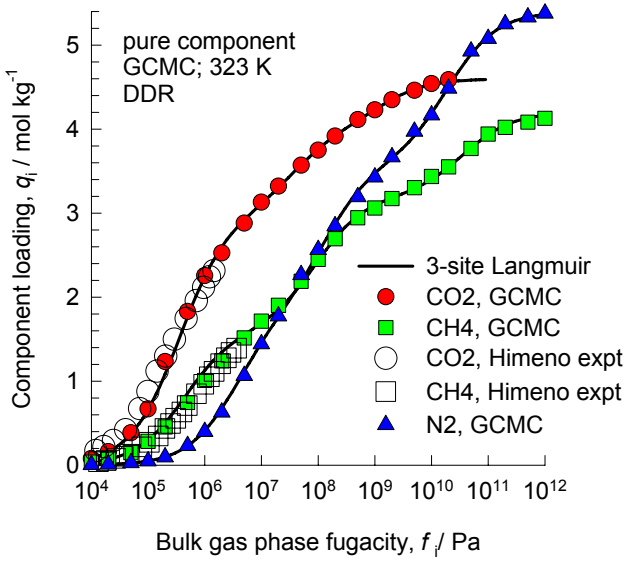
pure component
GCMC; 323 K
DDR
3-site Langmuir
CO2, GCMC
CH4, GCMC
CO2, Himeno expt
CH4, Himeno expt
N2, GCMC
Component loading, q_i / mol kg^{-1}
Bulk gas phase fugacity, f_i / Pa

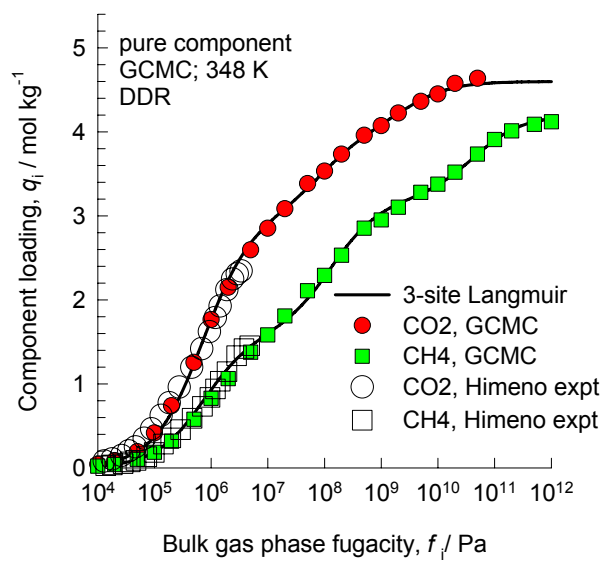
pure component
GCMC; 348 K
DDR
3-site Langmuir
CO2, GCMC
CH4, GCMC
CO2, Himeno expt
CH4, Himeno expt
Component loading, q_i / mol kg^{-1}
Bulk gas phase fugacity, f_i / Pa

Figure 2

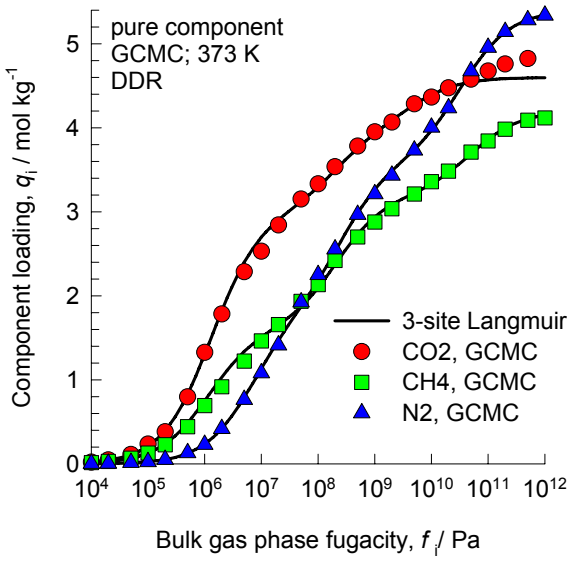
pure component
GCMC; 373 K
DDR
3-site Langmuir
CO2, GCMC
CH4, GCMC
N2, GCMC
Component loading, q_i / mol kg^{-1}
Bulk gas phase fugacity, f_i / Pa

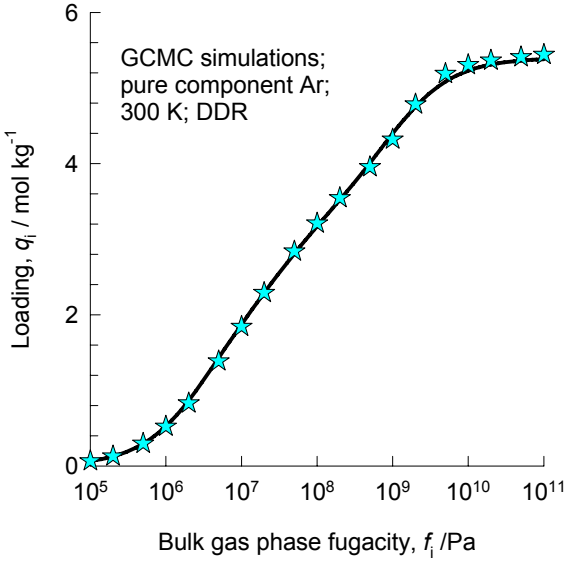
GCMC simulations;
pure component Ar;
300 K; DDR
Loading, q_i / mol kg^{-1}
Bulk gas phase fugacity, f_i /Pa

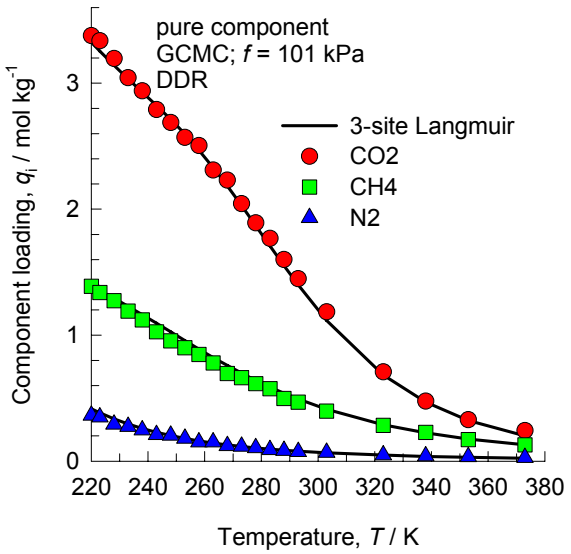
pure component
GCMC; f = 101 kPa
DDR
3-site Langmuir
CO2
CH4
N2
Component loading, q_i / mol kg^{-1}
Temperature, T / K

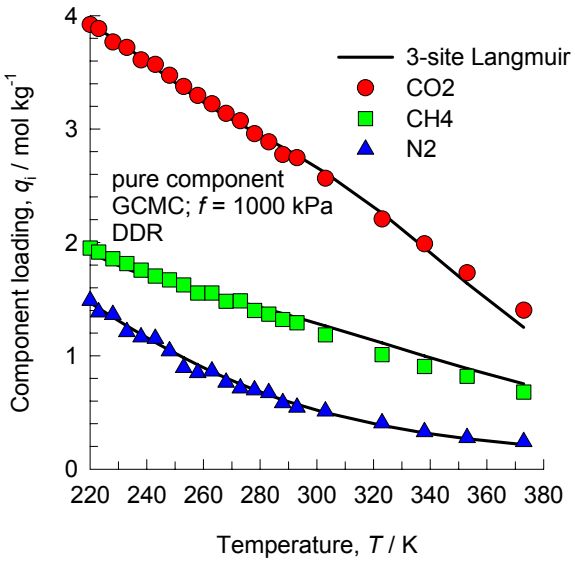
3-site Langmuir
CO2
CH4
N2
pure component
GCMC; f = 1000 kPa
DDR
Component loading, q_i / mol kg^{-1}
Temperature, T / K

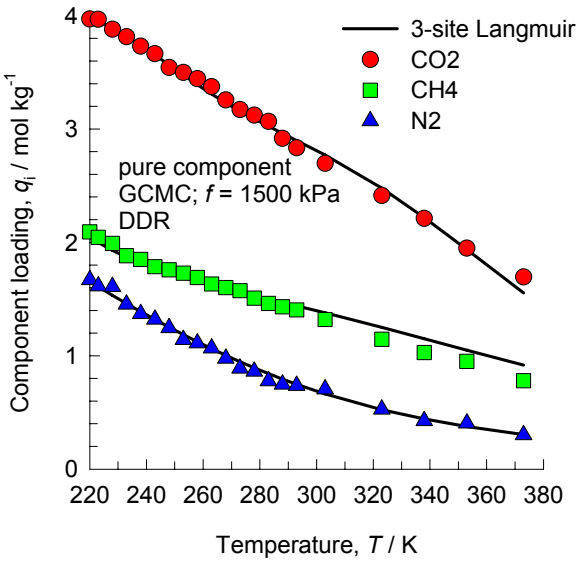
3-site Langmuir
CO2
CH4
N2
pure component
GCMC; f = 1500 kPa
DDR
Component loading, q_i / mol kg^{-1}
Temperature, T / K

DDR (all silica)

Figure 3

Side-on view

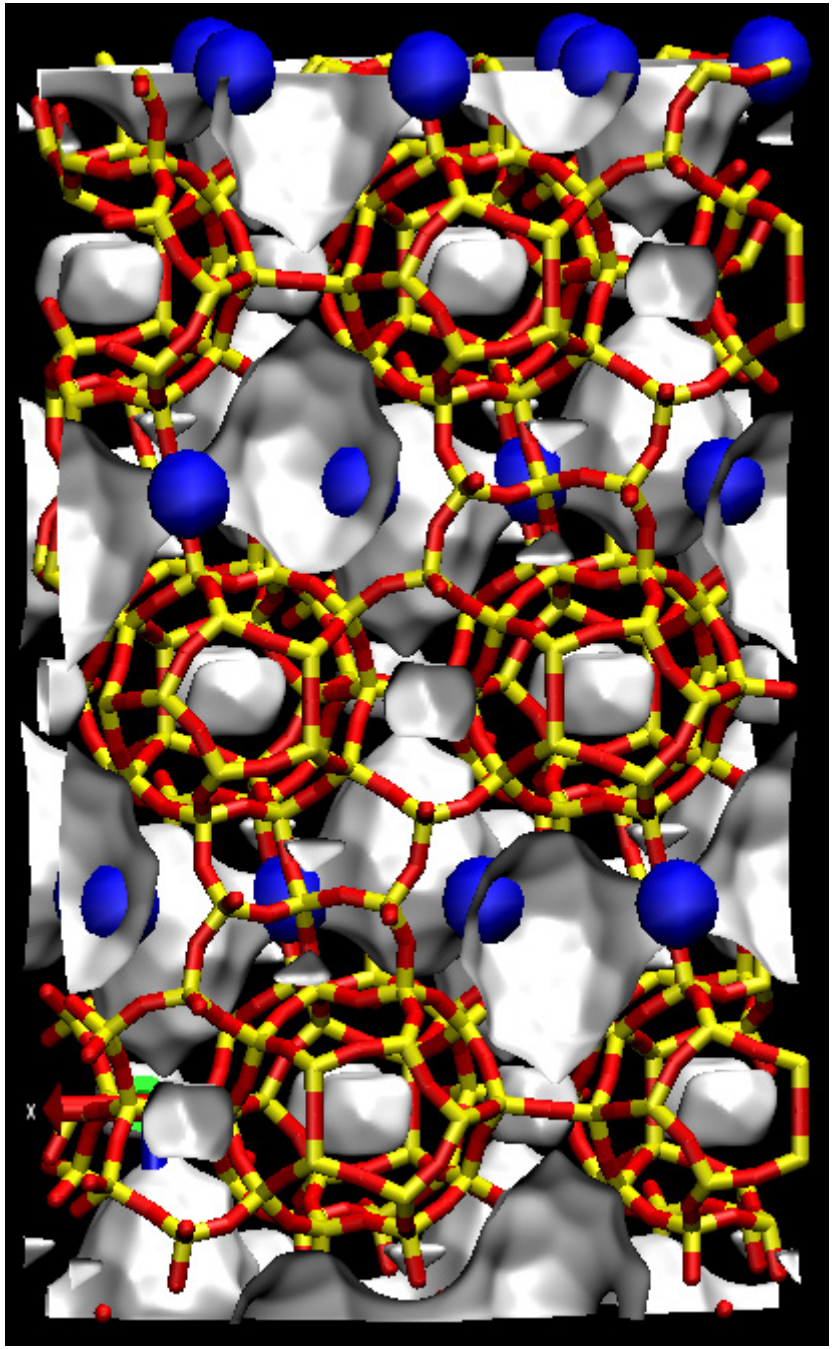

Window of DDR

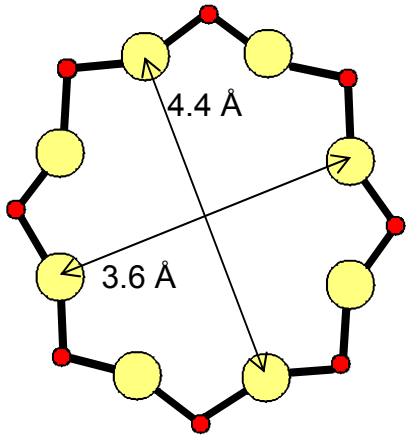

Blue spheres of 3 Å diameter

Top-down view

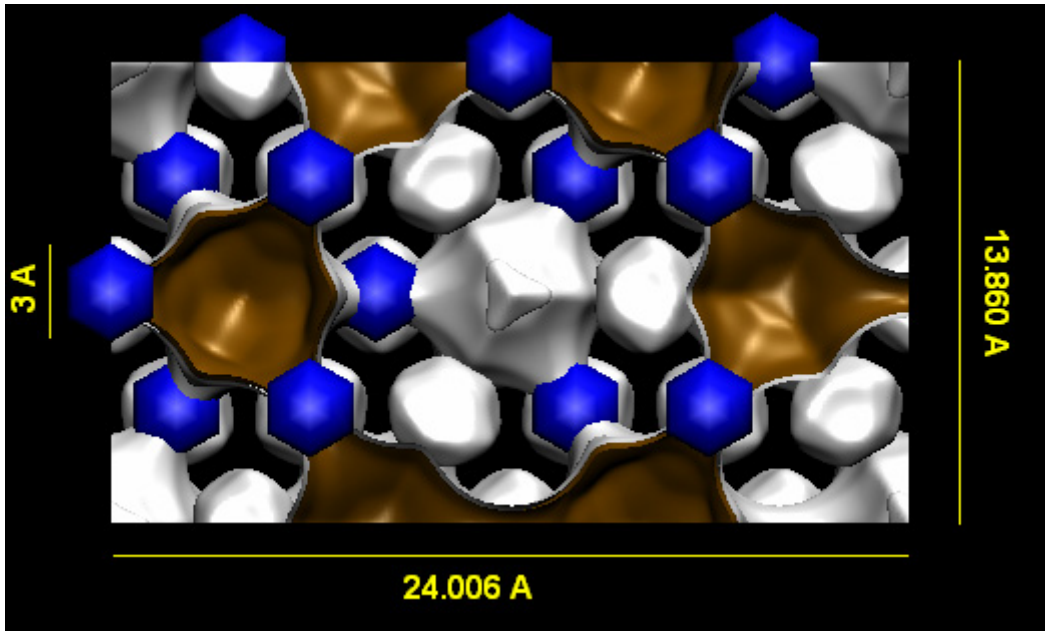

Figure 4

Probability density plot
of CH4 in DDR
f = 1 MPa, *T* = 273 K

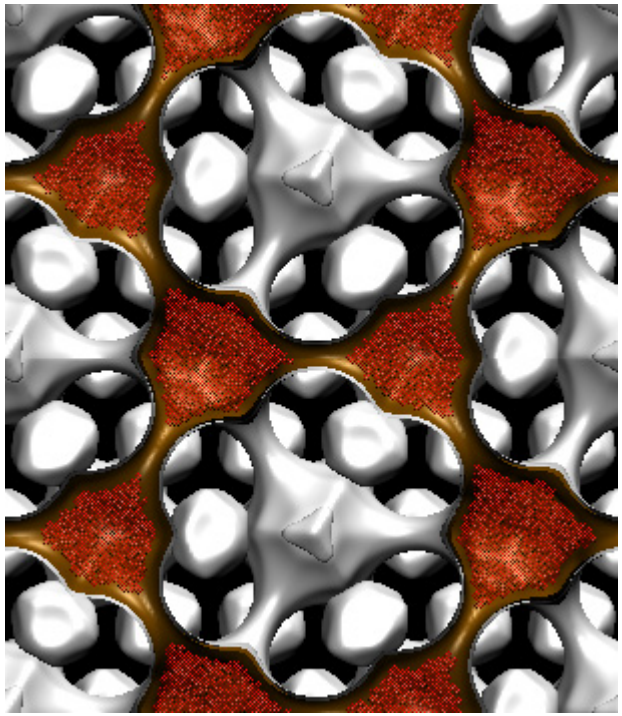

Figure 5

Probability density plot
of Ar in DDR
f = 1 MPa, T = 273 K

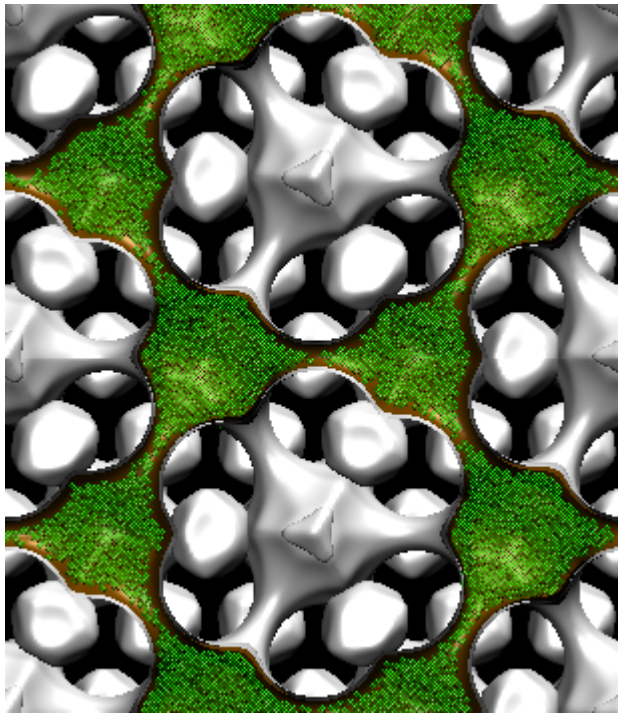

Figure 6

Probability density plot
of N2 in DDR
f = 1 MPa, *T* = 273 K

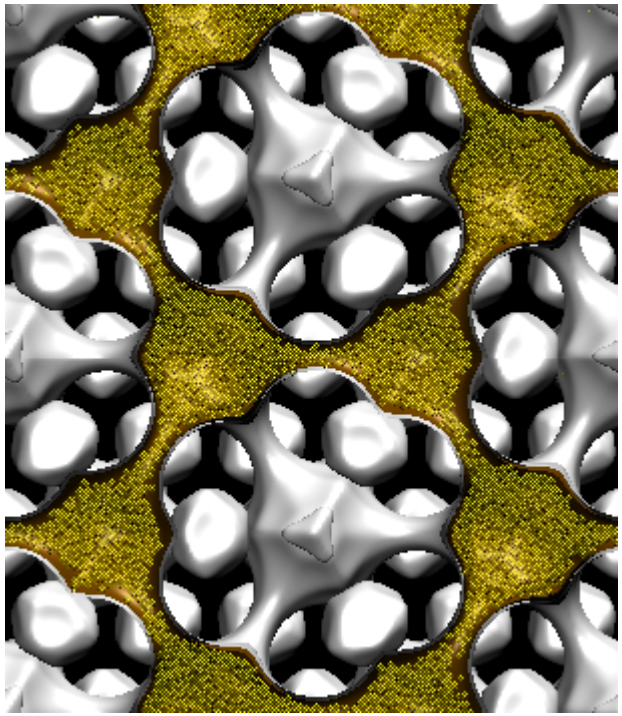

Figure 7

Probability density plot
of CO2 in DDR
f = 1 MPa, *T* = 273 K

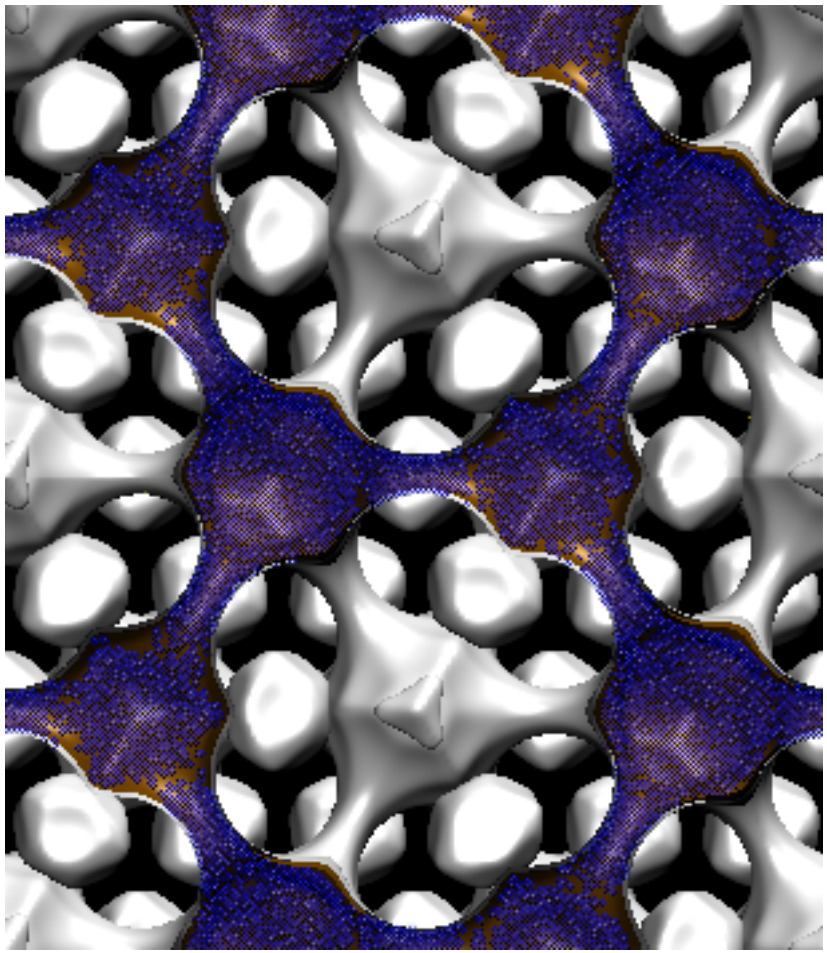

Figure 8

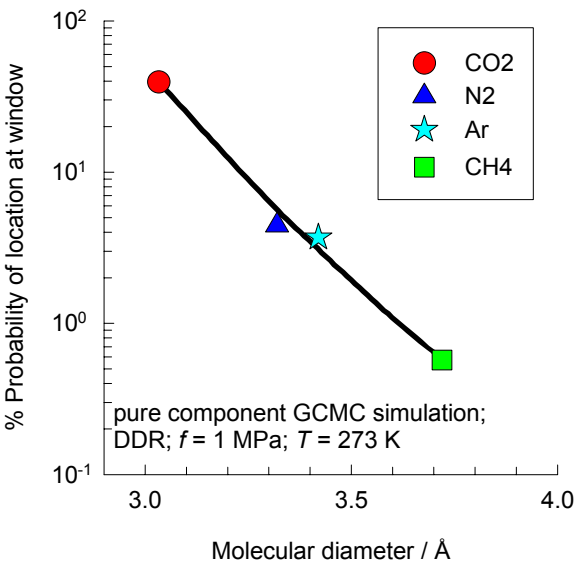
% Probability of location at window
10^2
10^1
10^0
10^{-1}
3.0
3.5
4.0
Molecular diameter / Å
CO2
N2
Ar
CH4
pure component GCMC simulation;
DDR; *f* = 1 MPa; *T* = 273 K

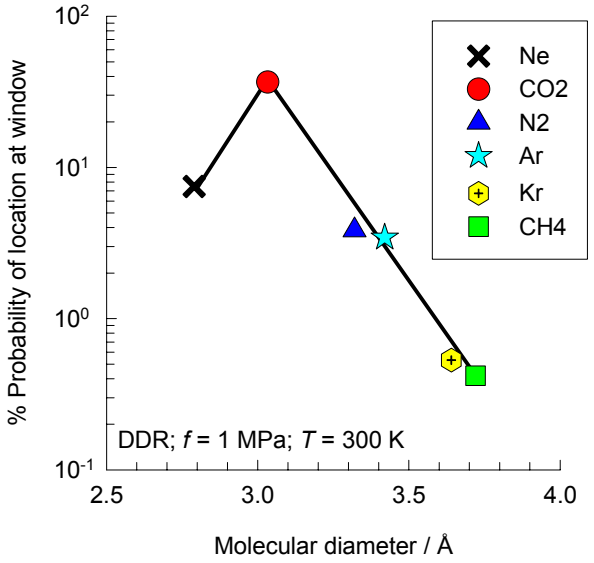
% Probability of location at window
10^2
10^1
10^0
10^{-1}
2.5
3.0
3.5
4.0
Molecular diameter / Å
Ne
CO2
N2
Ar
Kr
CH4
DDR; *f* = 1 MPa; *T* = 300 K

Figure 9

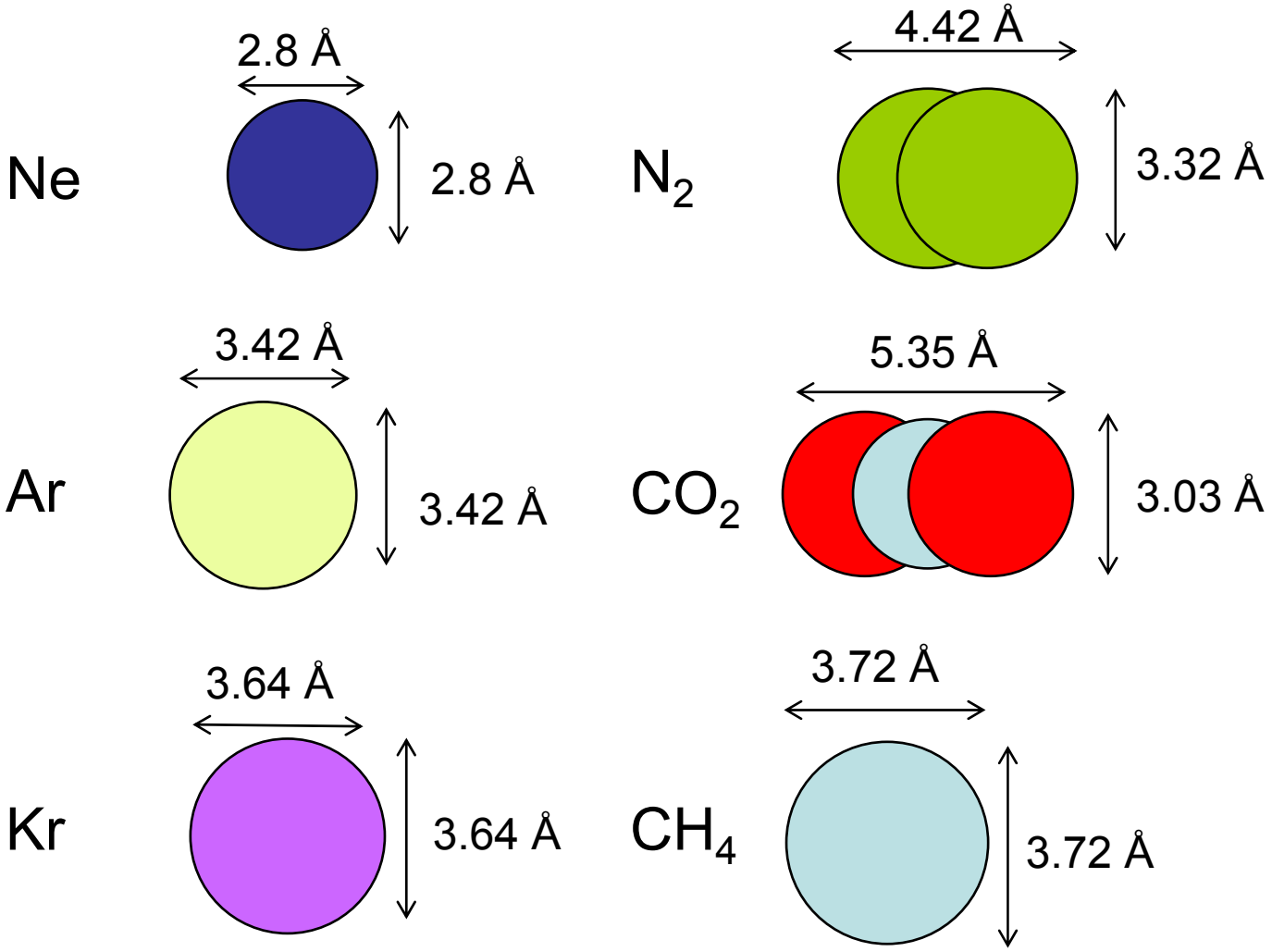
Ne
2.8 Å
2.8 Å
N_2
4.42 Å
3.32 Å
Ar
3.42 Å
3.42 Å
CO_2
5.35 Å
3.03 Å
Kr
3.64 Å
3.64 Å
CH_4
3.72 Å
3.72 Å

Probability density plot
of CH4-CO2 mixture in DDR
$f_1 = f_2$ =1 MPa, T = 273 K

Figure 10

Red dots = CH4
Blue dots = CO2

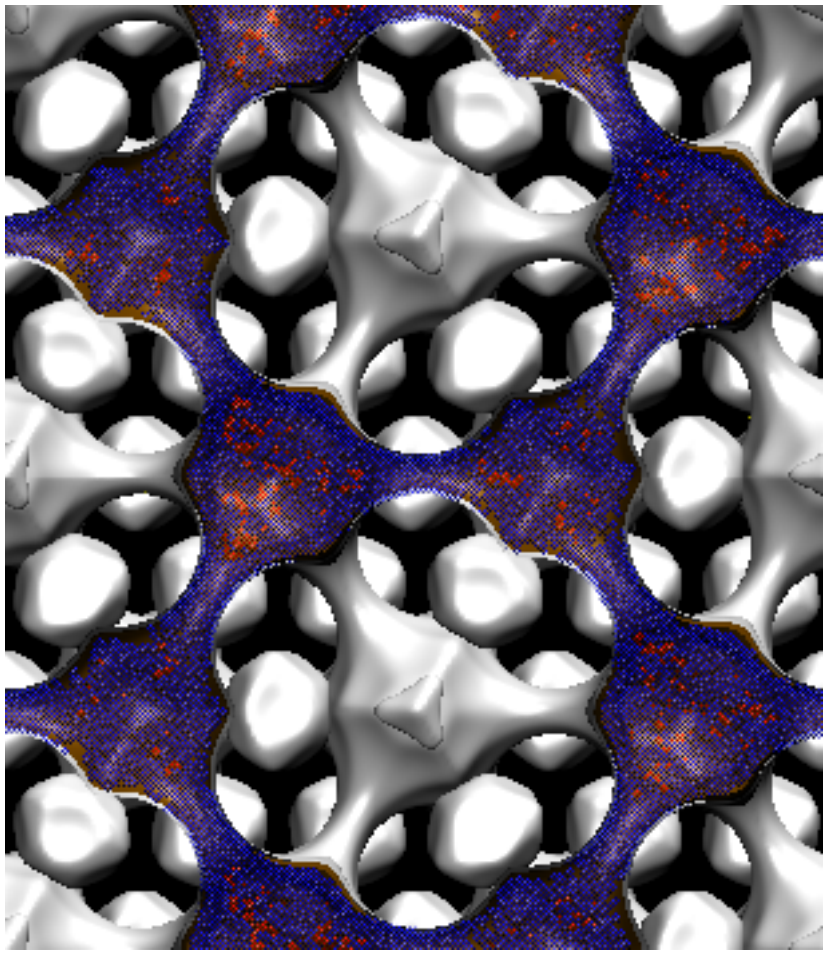

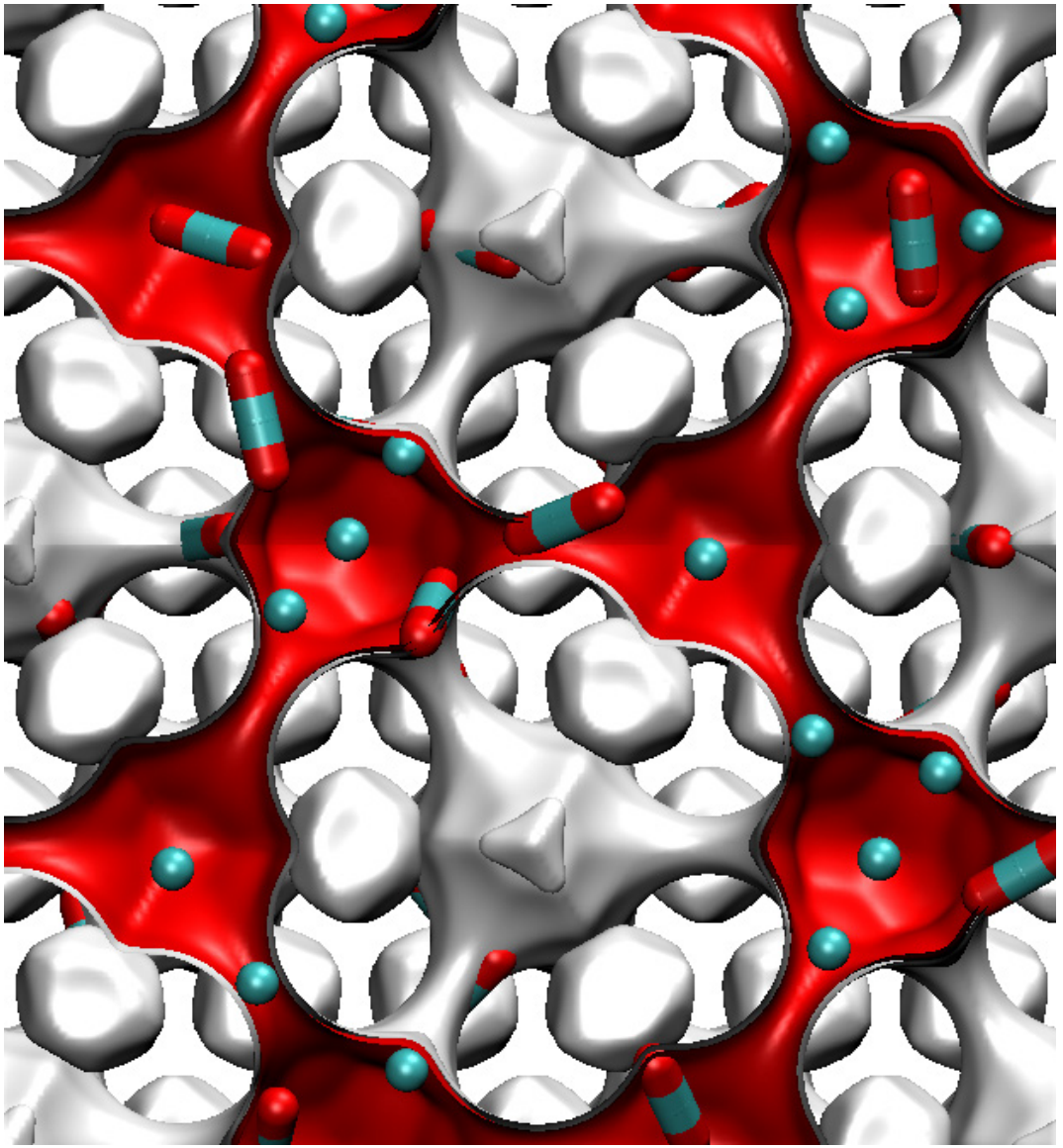

Probability density plot
of CH4-N2 mixture in DDR
$f_1 = f_2$ =1 MPa, T = 273 K

Figure 11

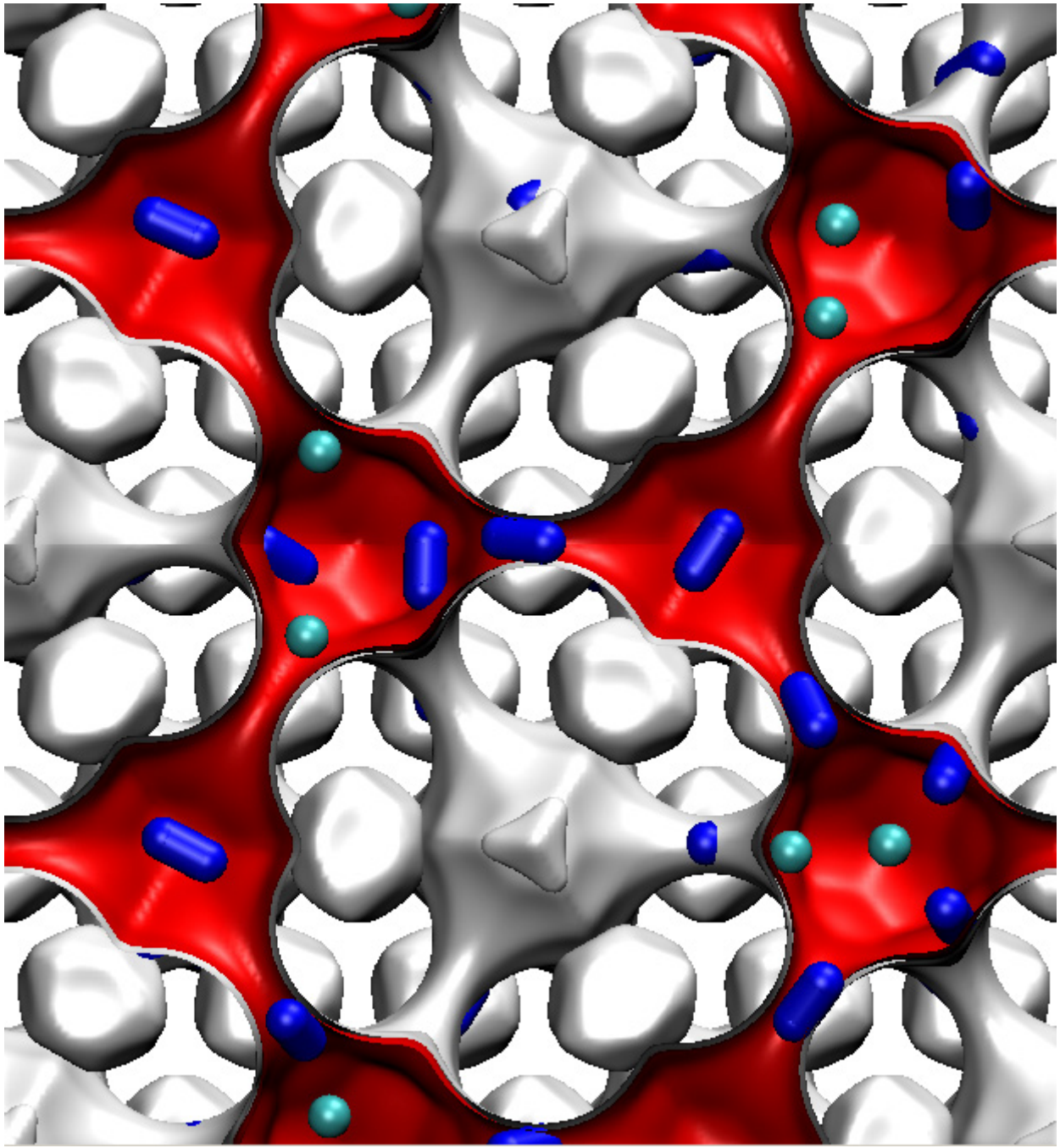

Red dots = CH4
Yellow dots = N2

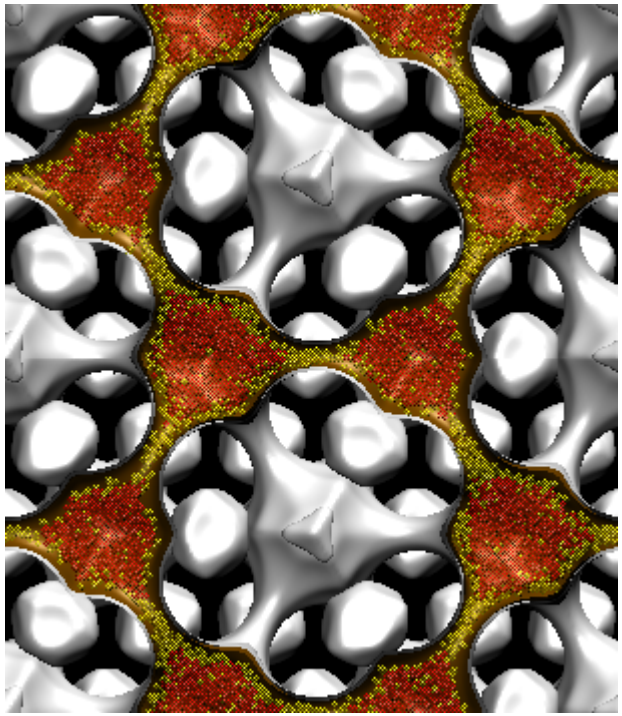

Figure 12

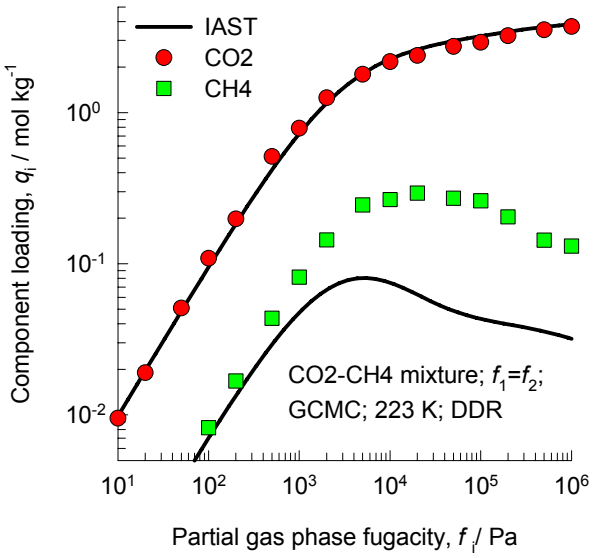
IAST
CO2
CH4
CO2-CH4 mixture; f_1=f_2;
GCMC; 223 K; DDR
Component loading, q_i / mol kg^{-1}
Partial gas phase fugacity, f_i / Pa

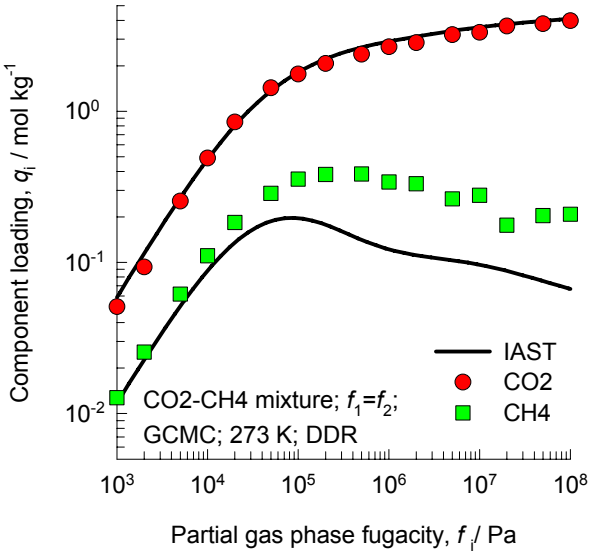
CO2-CH4 mixture; f_1=f_2;
GCMC; 273 K; DDR
IAST
CO2
CH4
Component loading, q_i / mol kg^{-1}
Partial gas phase fugacity, f_i / Pa

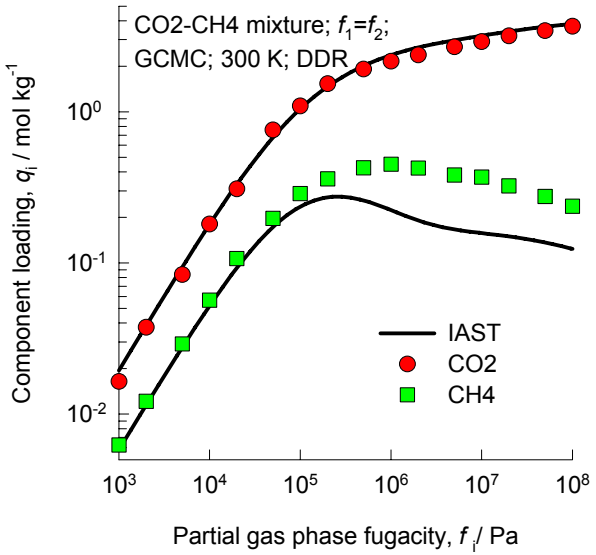
CO2-CH4 mixture; f_1=f_2;
GCMC; 300 K; DDR
IAST
CO2
CH4
Component loading, q_i / mol kg^{-1}
Partial gas phase fugacity, f_i / Pa

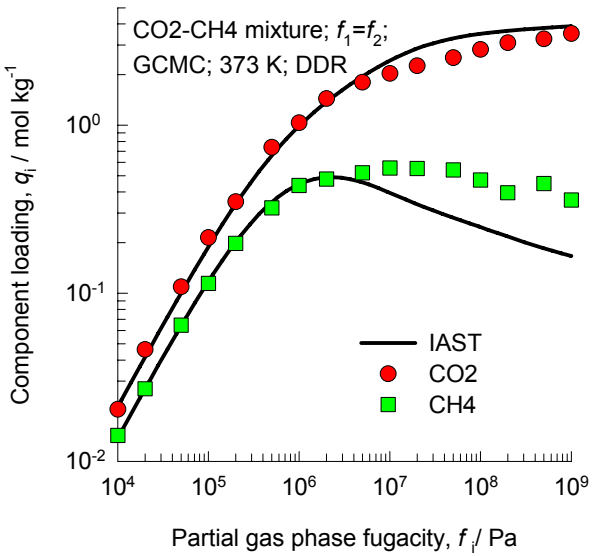
CO2-CH4 mixture; f_1=f_2;
GCMC; 373 K; DDR
IAST
CO2
CH4
Component loading, q_i / mol kg^{-1}
Partial gas phase fugacity, f_i / Pa

Figure 13

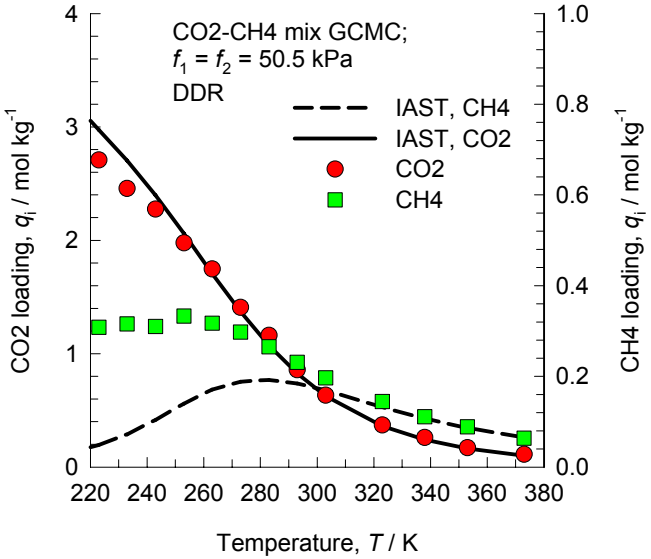
CO2-CH4 mix GCMC;
$f_1 = f_2$ = 50.5 kPa
DDR
IAST, CH4
IAST, CO2
CO2
CH4
CO2 loading, q_i / mol kg^{-1}
CH4 loading, q_i / mol kg^{-1}
Temperature, T / K

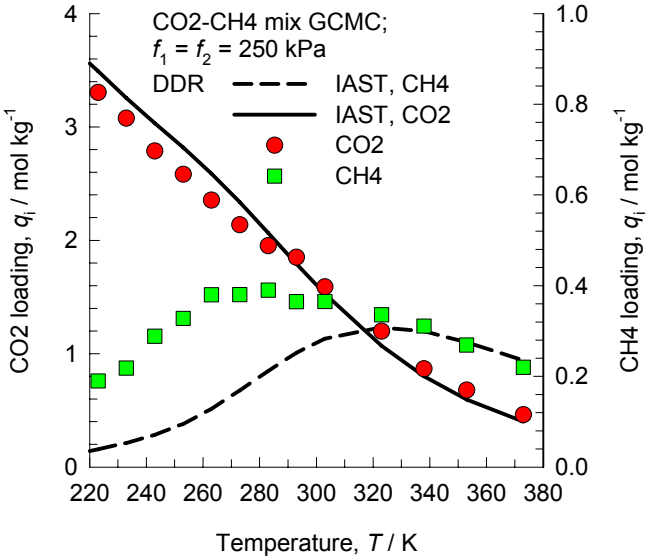
CO2-CH4 mix GCMC;
$f_1 = f_2$ = 250 kPa
DDR
IAST, CH4
IAST, CO2
CO2
CH4
CO2 loading, q_i / mol kg^{-1}
CH4 loading, q_i / mol kg^{-1}
Temperature, T / K

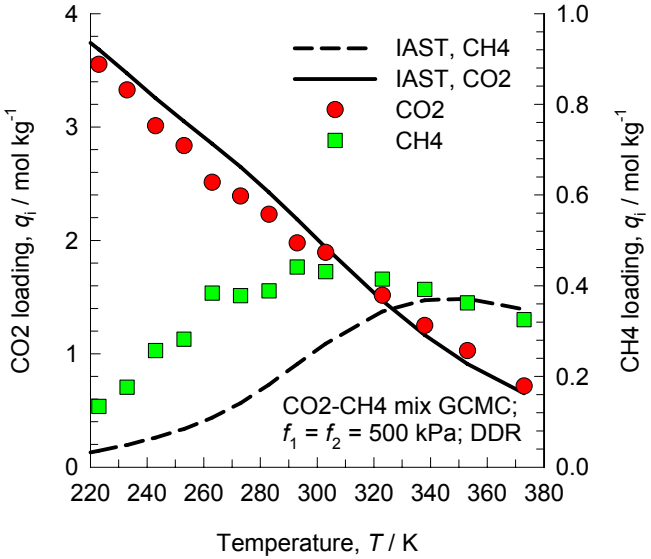
IAST, CH4
IAST, CO2
CO2
CH4
CO2-CH4 mix GCMC;
$f_1 = f_2$ = 500 kPa; DDR
CO2 loading, q_i / mol kg^{-1}
CH4 loading, q_i / mol kg^{-1}
Temperature, T / K

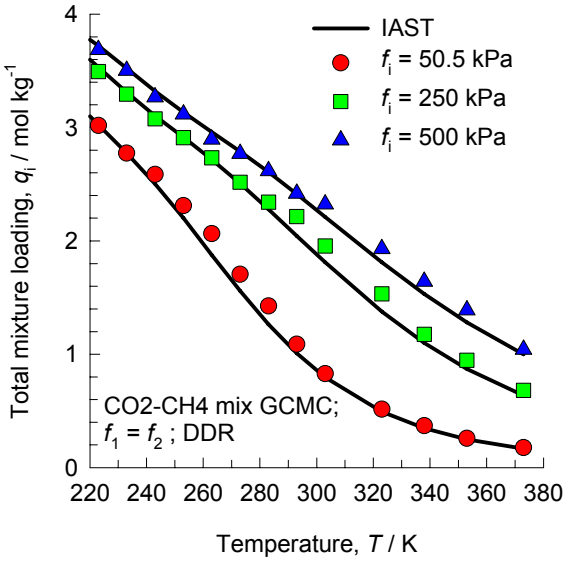
IAST
f_i = 50.5 kPa
f_i = 250 kPa
f_i = 500 kPa
CO2-CH4 mix GCMC;
$f_1 = f_2$; DDR
Total mixture loading, q_i / mol kg^{-1}
Temperature, T / K

Figure 14

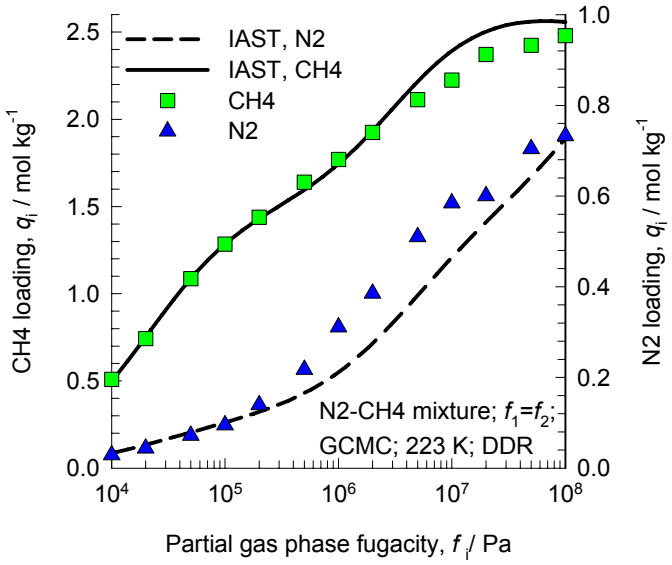
IAST, N2
IAST, CH4
CH4
N2
N2-CH4 mixture; f_1=f_2;
GCMC; 223 K; DDR
CH4 loading, q_i / mol kg^{-1}
N2 loading, q_i / mol kg^{-1}
Partial gas phase fugacity, f_i / Pa

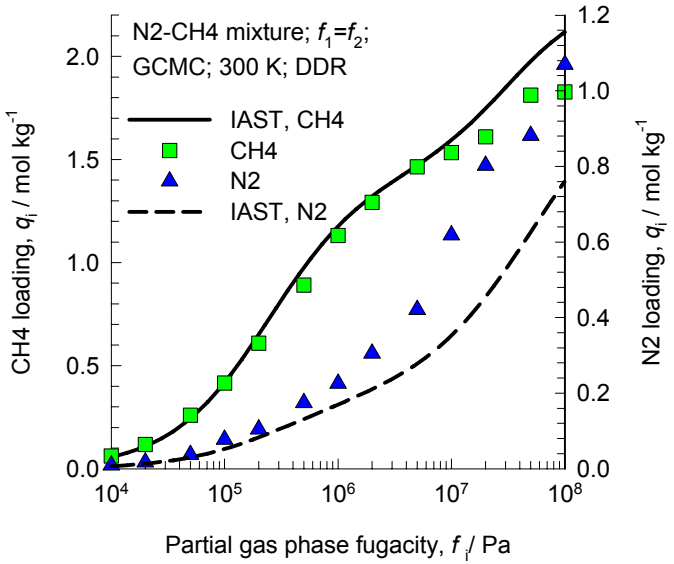
N2-CH4 mixture; f_1=f_2;
GCMC; 300 K; DDR
IAST, CH4
CH4
N2
IAST, N2
CH4 loading, q_i / mol kg^{-1}
N2 loading, q_i / mol kg^{-1}
Partial gas phase fugacity, f_i / Pa

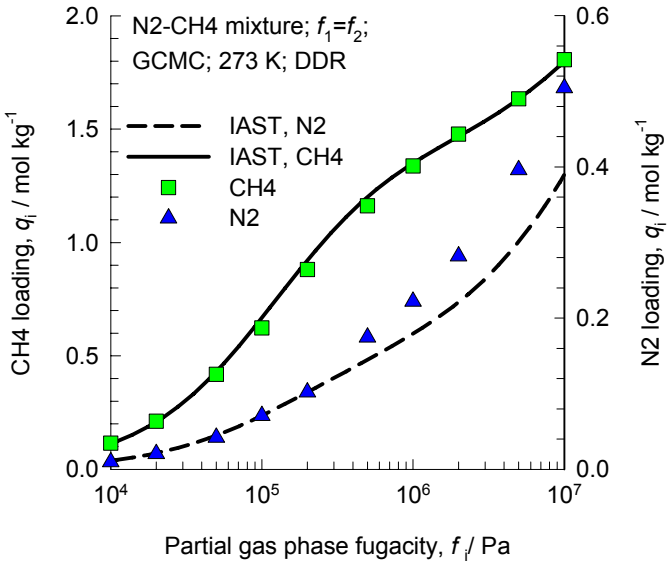
N2-CH4 mixture; f_1=f_2;
GCMC; 273 K; DDR
IAST, N2
IAST, CH4
CH4
N2
CH4 loading, q_i / mol kg^{-1}
N2 loading, q_i / mol kg^{-1}
Partial gas phase fugacity, f_i / Pa

Figure 15

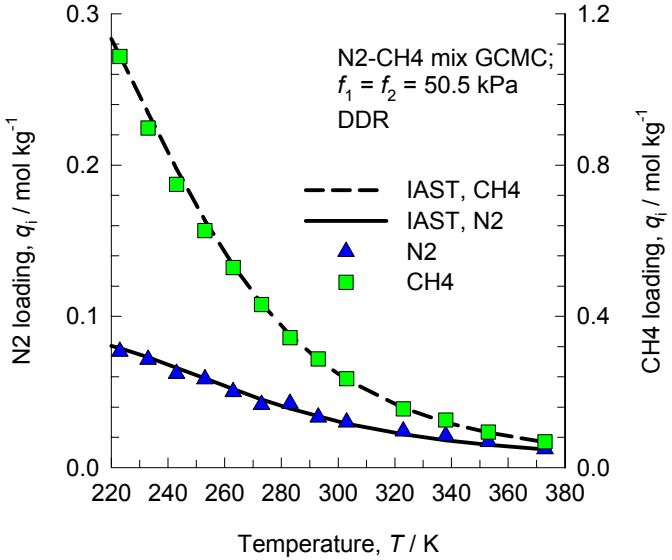
N2-CH4 mix GCMC;
$f_1 = f_2$ = 50.5 kPa
DDR
IAST, CH4
IAST, N2
N2
CH4
N2 loading, q_i / mol kg^{-1}
CH4 loading, q_i / mol kg^{-1}
Temperature, T / K

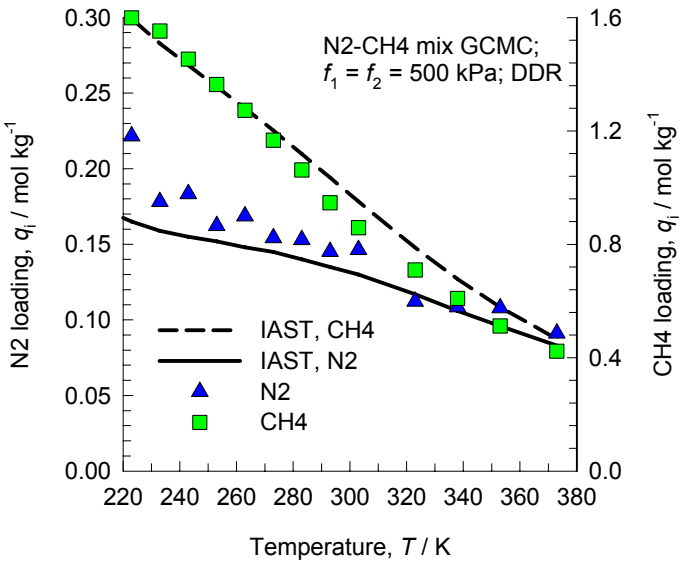
N2-CH4 mix GCMC;
$f_1 = f_2$ = 500 kPa; DDR
IAST, CH4
IAST, N2
N2
CH4
N2 loading, q_i / mol kg^{-1}
CH4 loading, q_i / mol kg^{-1}
Temperature, T / K

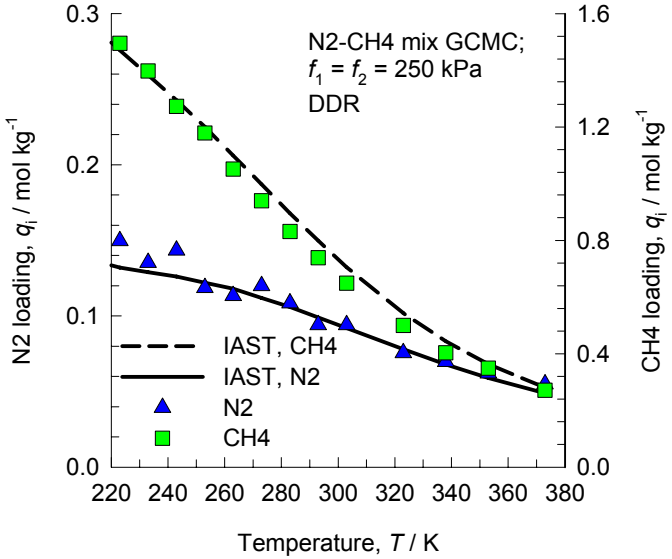
N2-CH4 mix GCMC;
$f_1 = f_2$ = 250 kPa
DDR
IAST, CH4
IAST, N2
N2
CH4
N2 loading, q_i / mol kg^{-1}
CH4 loading, q_i / mol kg^{-1}
Temperature, T / K

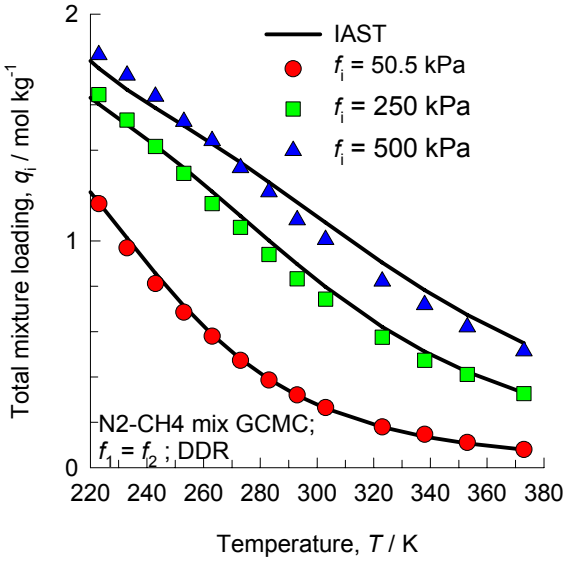
IAST
f_i = 50.5 kPa
f_i = 250 kPa
f_i = 500 kPa
N2-CH4 mix GCMC;
$f_1 = f_2$; DDR
Total mixture loading, q_i / mol kg^{-1}
Temperature, T / K

Figure 16

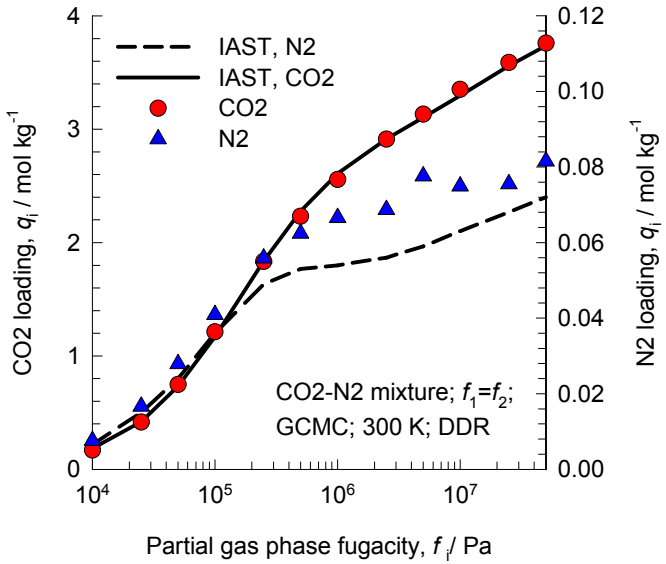
IAST, N2
IAST, CO2
CO2
N2
CO2-N2 mixture; f_1=f_2;
GCMC; 300 K; DDR
CO2 loading, q_i / mol kg^{-1}
N2 loading, q_i / mol kg^{-1}
Partial gas phase fugacity, f_i / Pa
0
1
2
3
4
0.00
0.02
0.04
0.06
0.08
0.10
0.12
10^4
10^5
10^6
10^7

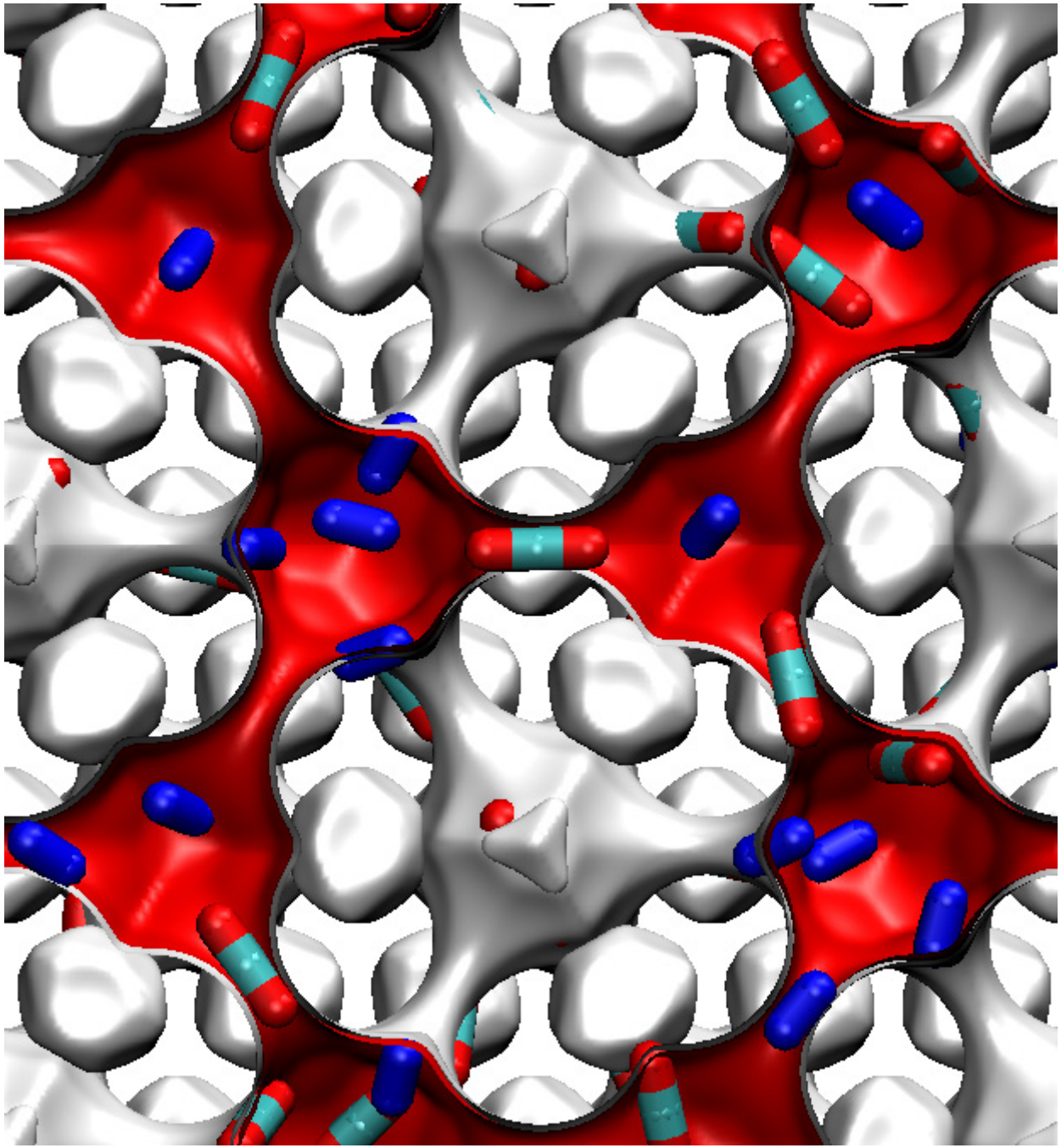

Figure 17

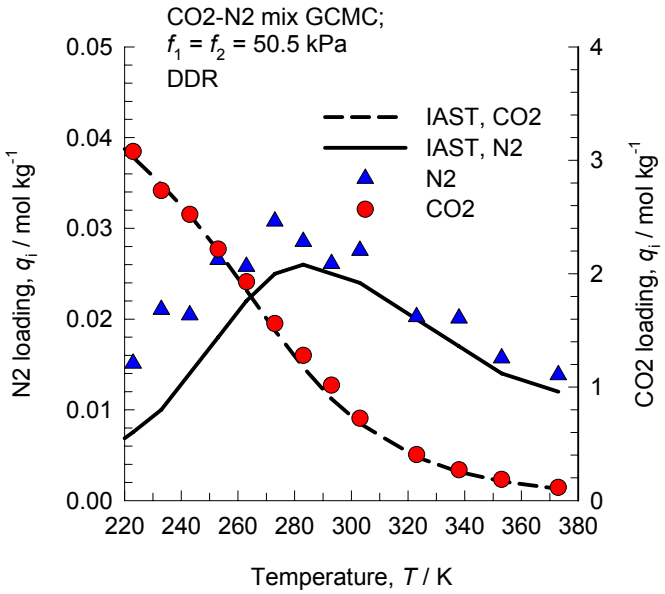
CO2-N2 mix GCMC;
$f_1 = f_2$ = 50.5 kPa
DDR
IAST, CO2
IAST, N2
N2
CO2
N2 loading, q_i / mol kg^{-1}
CO2 loading, q_i / mol kg^{-1}
Temperature, T / K

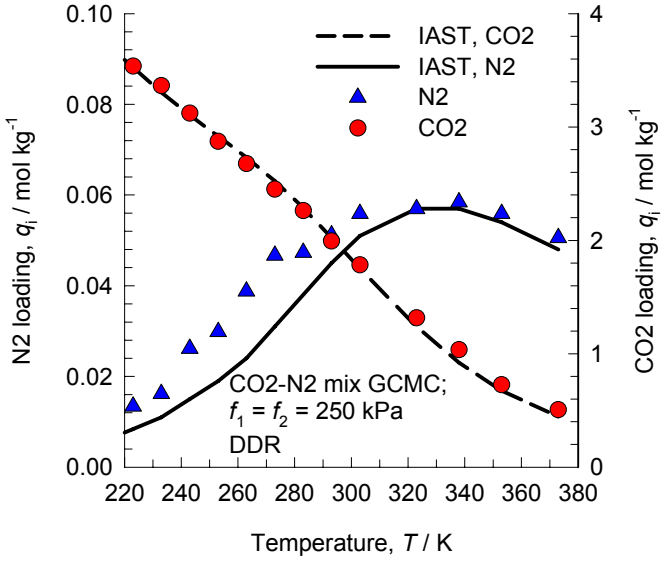
IAST, CO2
IAST, N2
N2
CO2
CO2-N2 mix GCMC;
$f_1 = f_2$ = 250 kPa
DDR
N2 loading, q_i / mol kg^{-1}
CO2 loading, q_i / mol kg^{-1}
Temperature, T / K

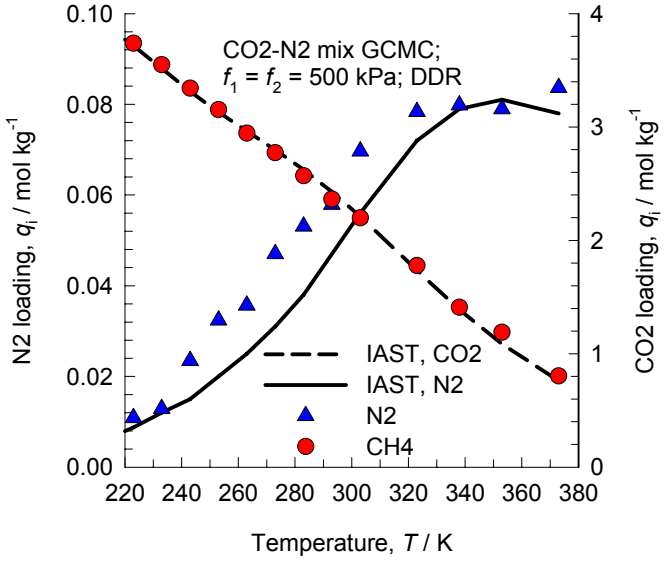
CO2-N2 mix GCMC;
$f_1 = f_2$ = 500 kPa; DDR
IAST, CO2
IAST, N2
N2
CH4
N2 loading, q_i / mol kg^{-1}
CO2 loading, q_i / mol kg^{-1}
Temperature, T / K

Figure 18

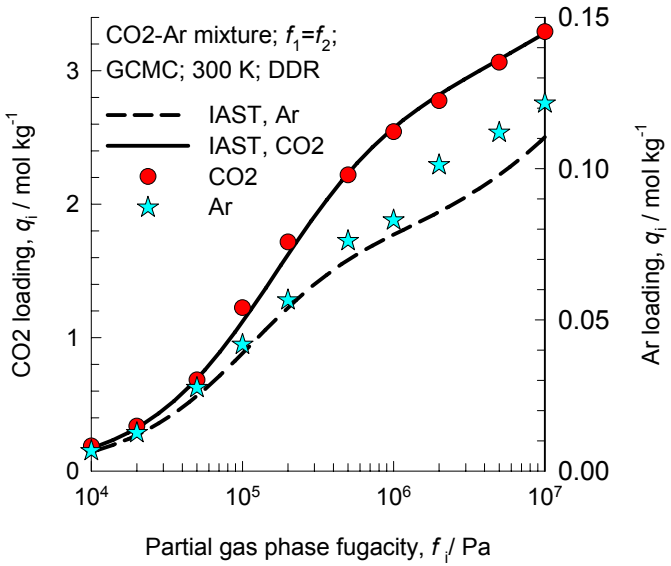
CO2-Ar mixture; f_1=f_2;
GCMC; 300 K; DDR
IAST, Ar
IAST, CO2
CO2
Ar
CO2 loading, q_i / mol kg^{-1}
Ar loading, q_i / mol kg^{-1}
Partial gas phase fugacity, f_i / Pa
0
1
2
3
0.00
0.05
0.10
0.15
10^4
10^5
10^6
10^7

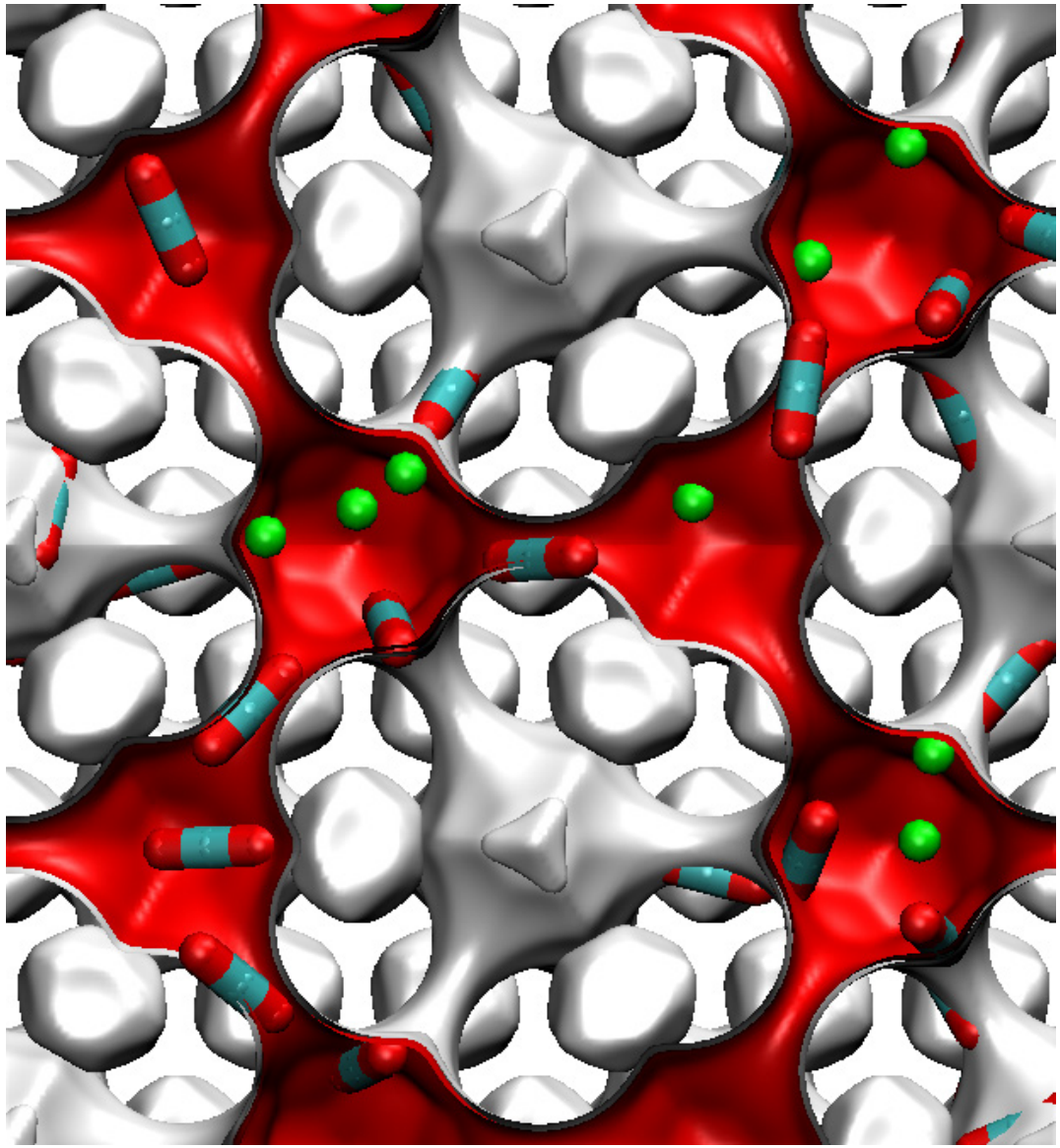

Figure 19

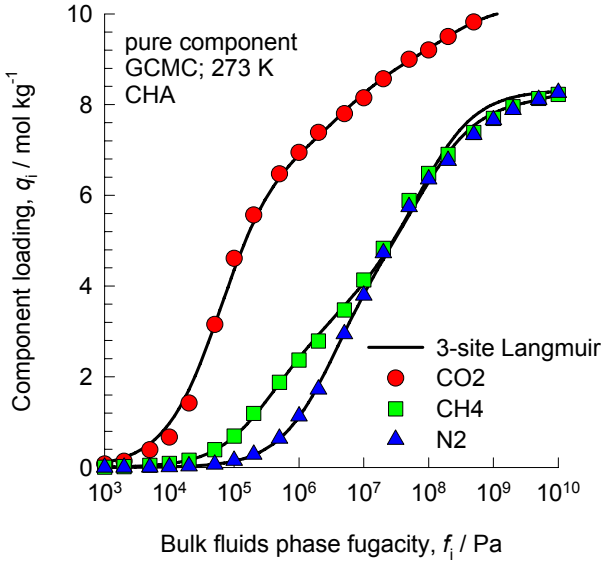
pure component
GCMC; 273 K
CHA
3-site Langmuir
CO2
CH4
N2
Component loading, q_i / mol kg^{-1}
Bulk fluids phase fugacity, f_i / Pa

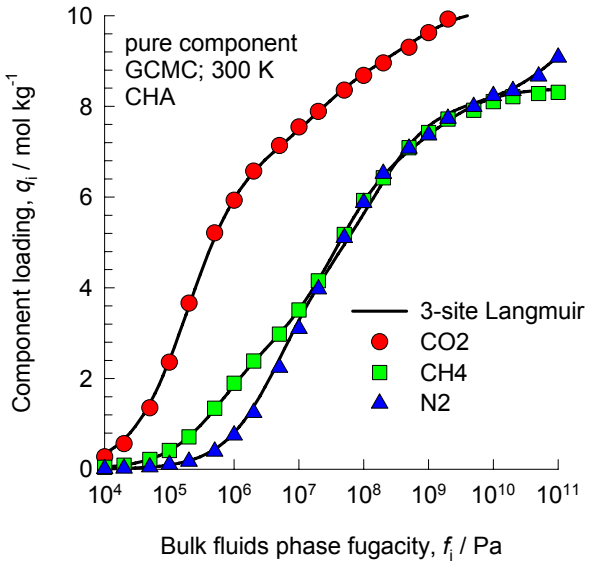
pure component
GCMC; 300 K
CHA
3-site Langmuir
CO2
CH4
N2
Component loading, q_i / mol kg^{-1}
Bulk fluids phase fugacity, f_i / Pa

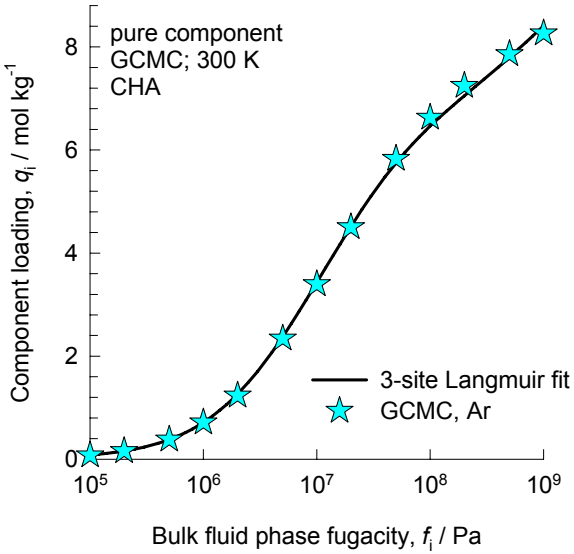
pure component
GCMC; 300 K
CHA
3-site Langmuir fit
GCMC, Ar
Component loading, q_i / mol kg^{-1}
Bulk fluid phase fugacity, f_i / Pa

CHA (all silica)

Figure 20

Window of CHA

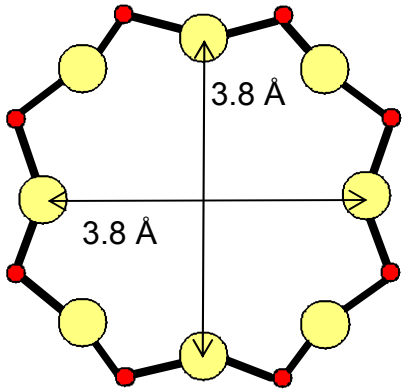

Side-on view

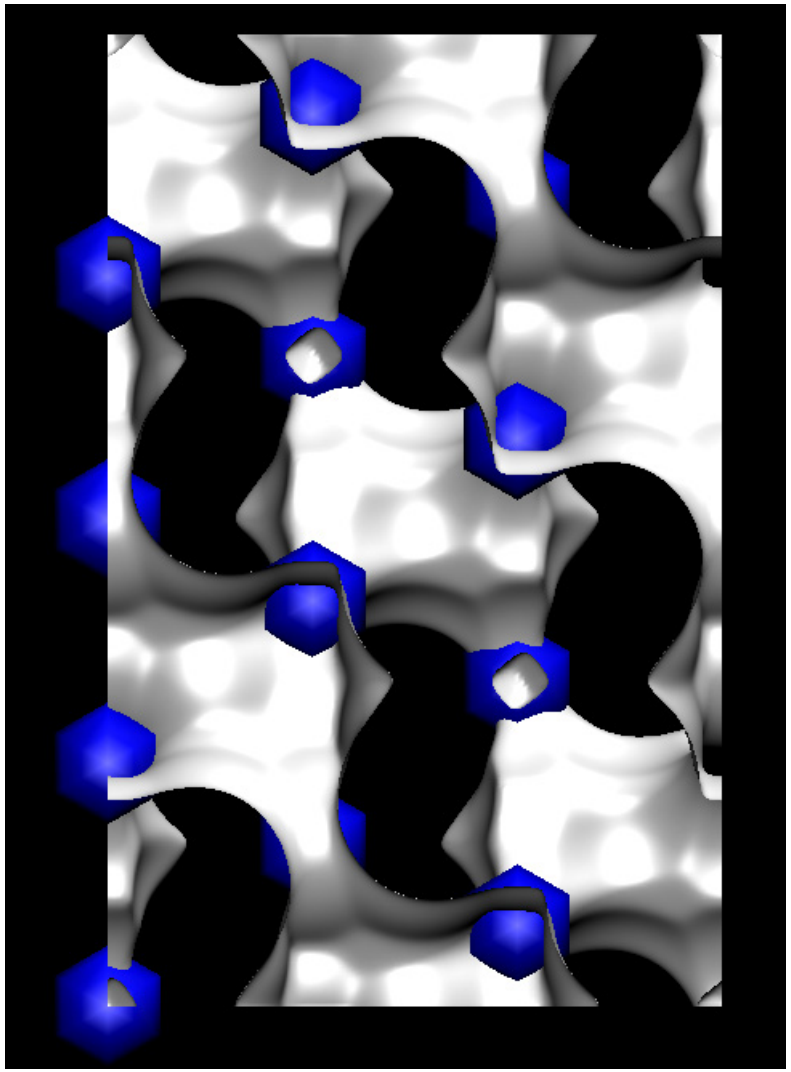

Top-down view

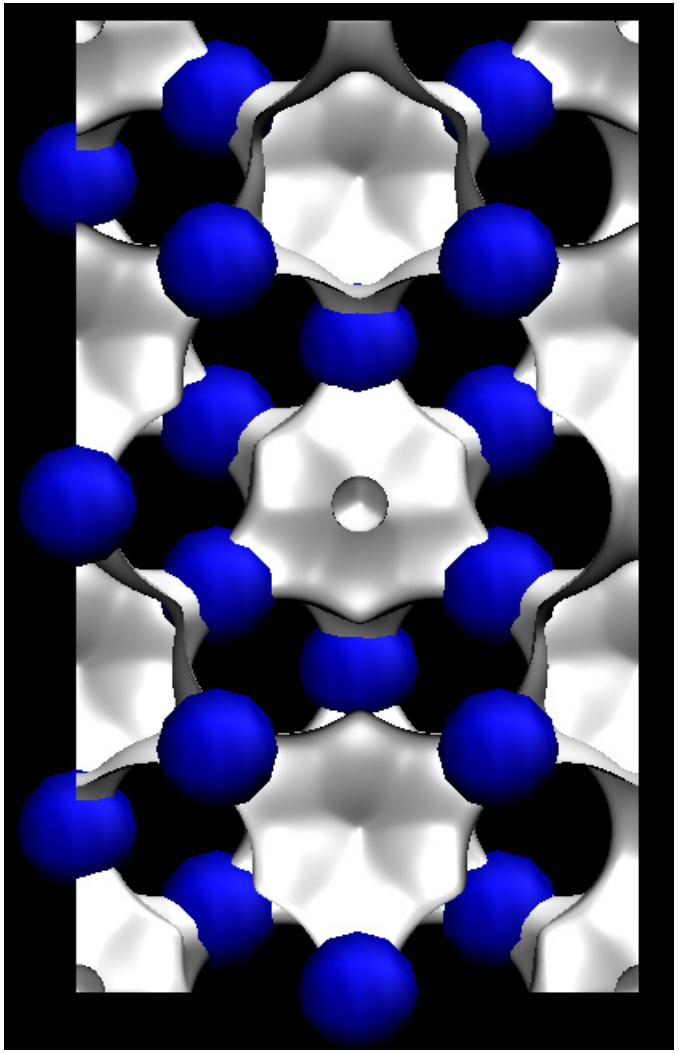

Blue spheres
of 3 Å diameter

Probability density plot
of CH4 in CHA
f = 1 MPa, *T* = 300 K

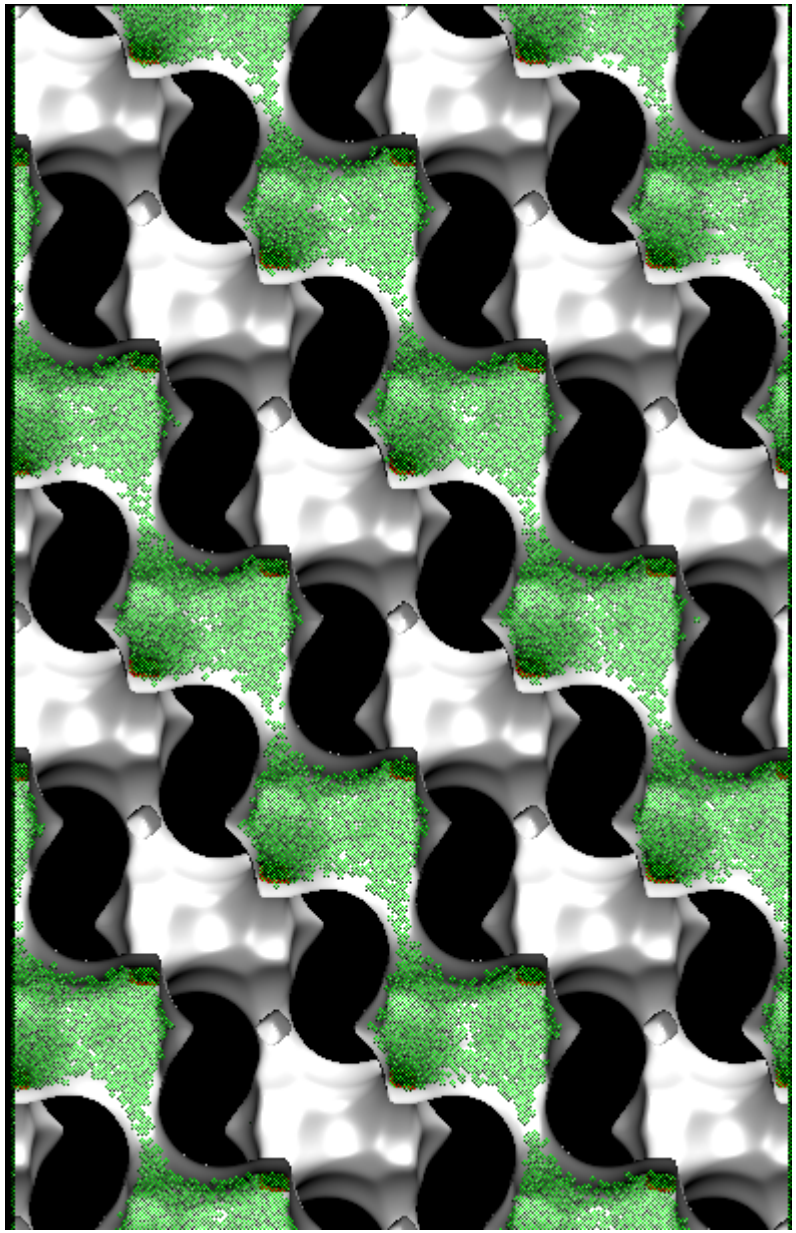

Probability density plot
of Ar in CHA
f = 1 MPa, T = 300 K

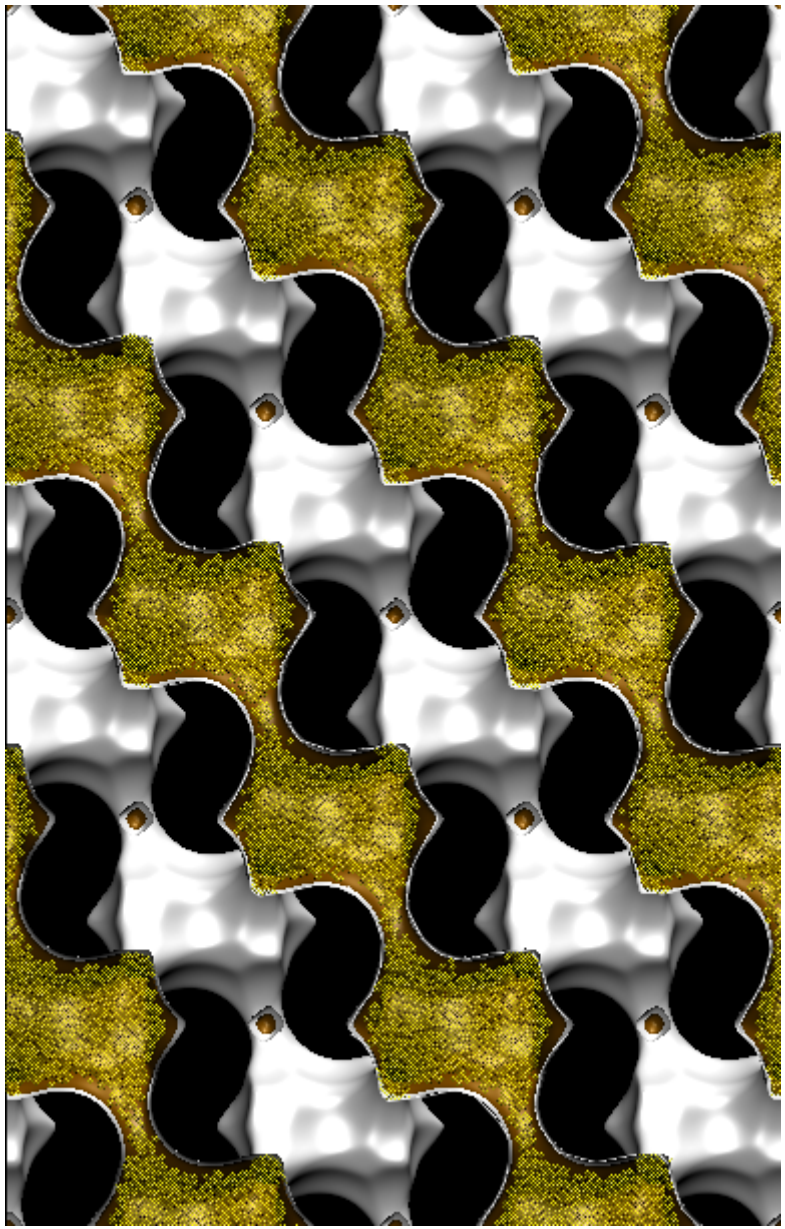

Probability density plot
of N2 in CHA
f = 1 MPa, T = 300 K

Probability density plot
of CO2 in CHA
f = 1 MPa, *T* = 300 K

Figure 25

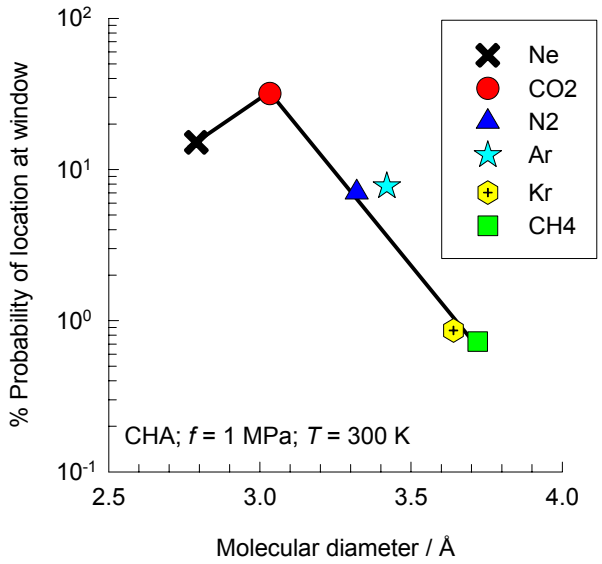
% Probability of location at window
10^2
10^1
10^0
10^{-1}
2.5
3.0
3.5
4.0
Molecular diameter / Å
Ne
CO2
N2
Ar
Kr
CH4
CHA; f = 1 MPa; T = 300 K

Figure 26

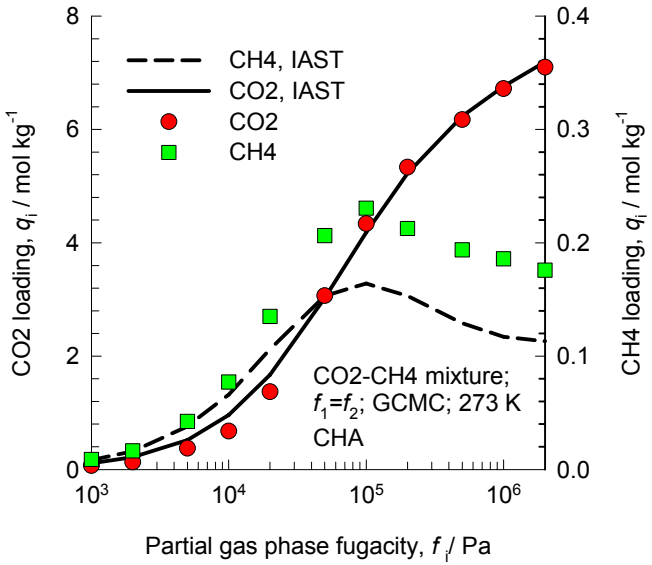
CH4, IAST
CO2, IAST
CO2
CH4
CO2-CH4 mixture;
f_1=f_2; GCMC; 273 K
CHA
CO2 loading, q_i / mol kg^{-1}
CH4 loading, q_i / mol kg^{-1}
Partial gas phase fugacity, f_i / Pa

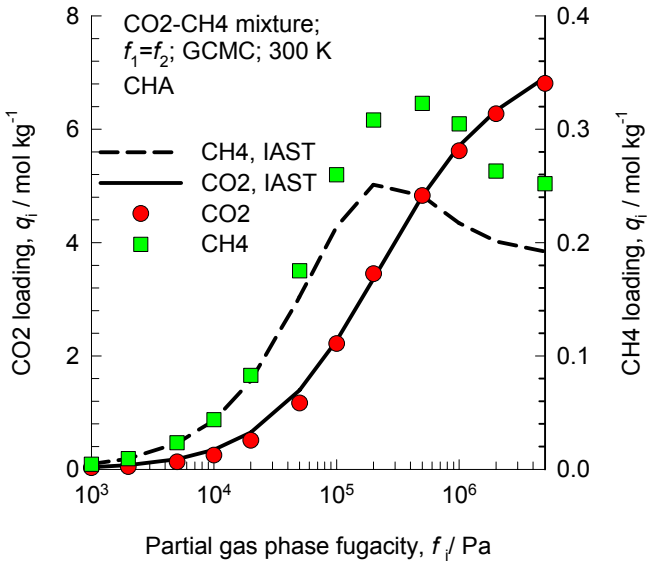
CO2-CH4 mixture;
f_1=f_2; GCMC; 300 K
CHA
CH4, IAST
CO2, IAST
CO2
CH4
CO2 loading, q_i / mol kg^{-1}
CH4 loading, q_i / mol kg^{-1}
Partial gas phase fugacity, f_i / Pa

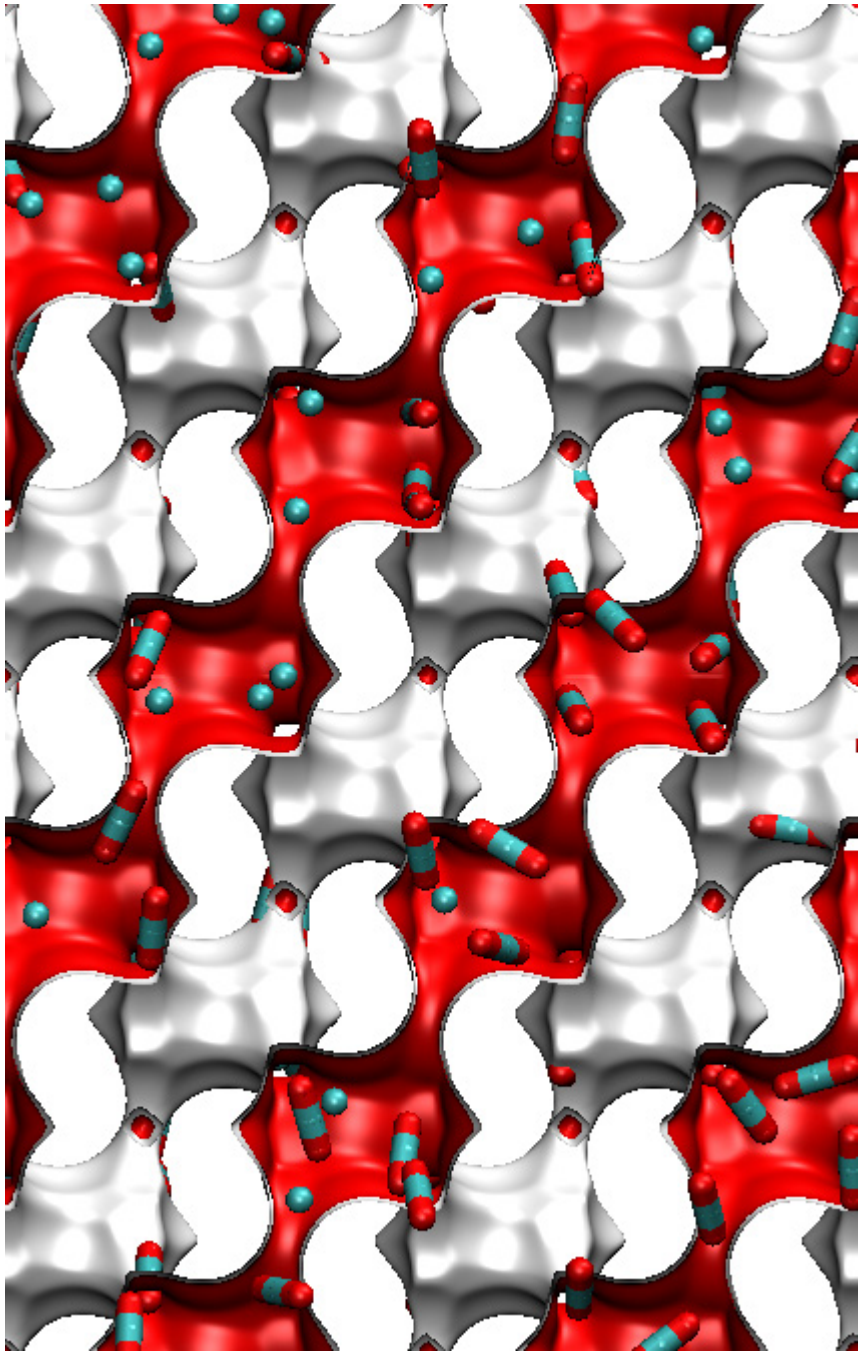

Figure 27

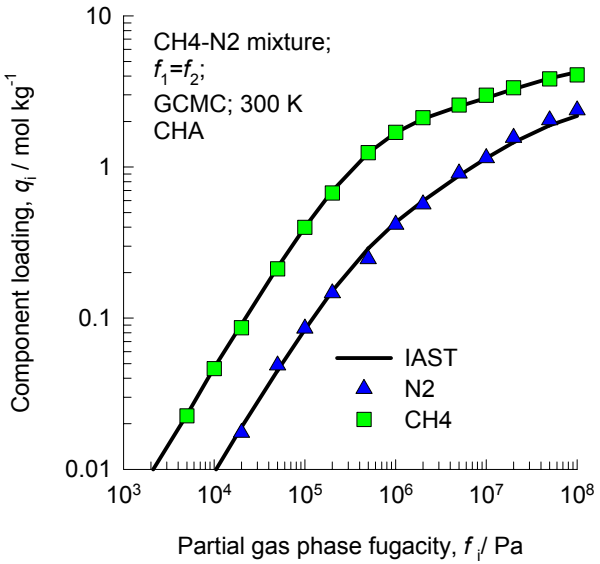
CH4-N2 mixture;
f_1=f_2;
GCMC; 300 K
CHA
IAST
N2
CH4
Component loading, q_i / mol kg^{-1}
Partial gas phase fugacity, f_i / Pa
10
1
0.1
0.01
10^3
10^4
10^5
10^6
10^7
10^8

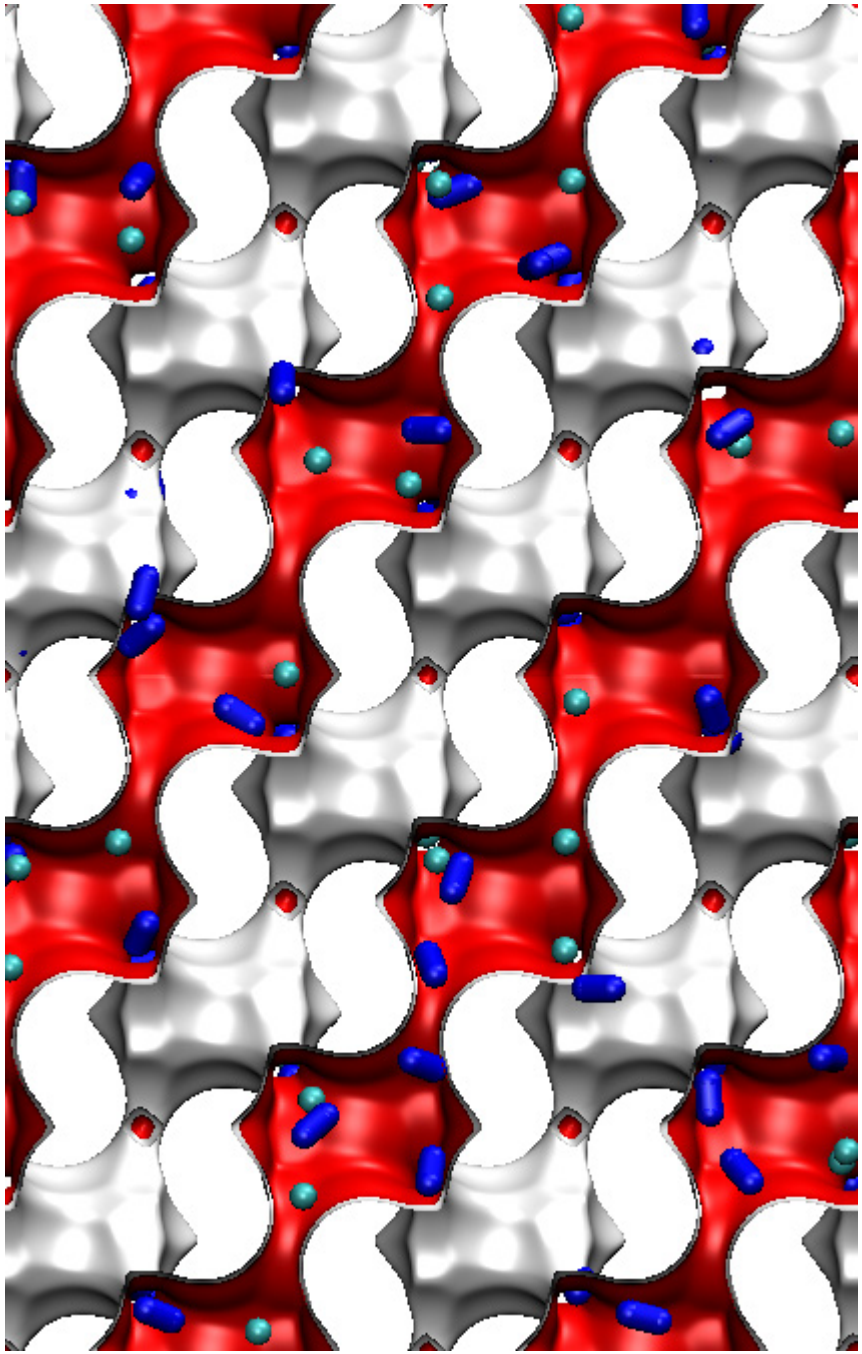

Figure 28

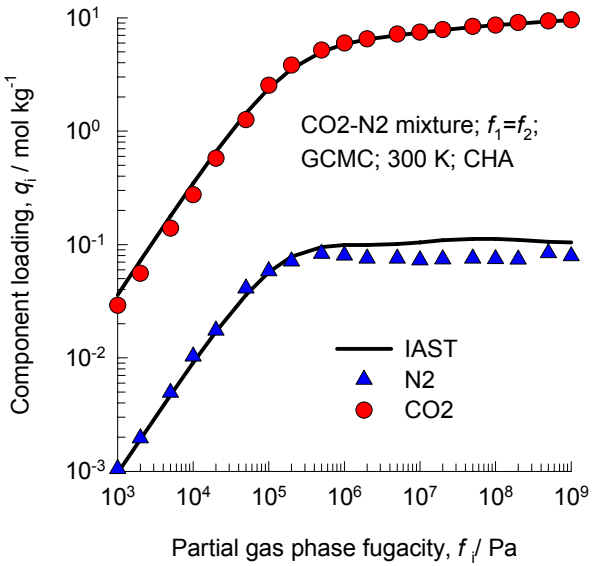
Component loading, q_i / mol kg^{-1}
10^{1}
10^{0}
10^{-1}
10^{-2}
10^{-3}
10^{3}
10^{4}
10^{5}
10^{6}
10^{7}
10^{8}
10^{9}
CO2-N2 mixture; f_1=f_2;
GCMC; 300 K; CHA
IAST
N2
CO2
Partial gas phase fugacity, f_i / Pa

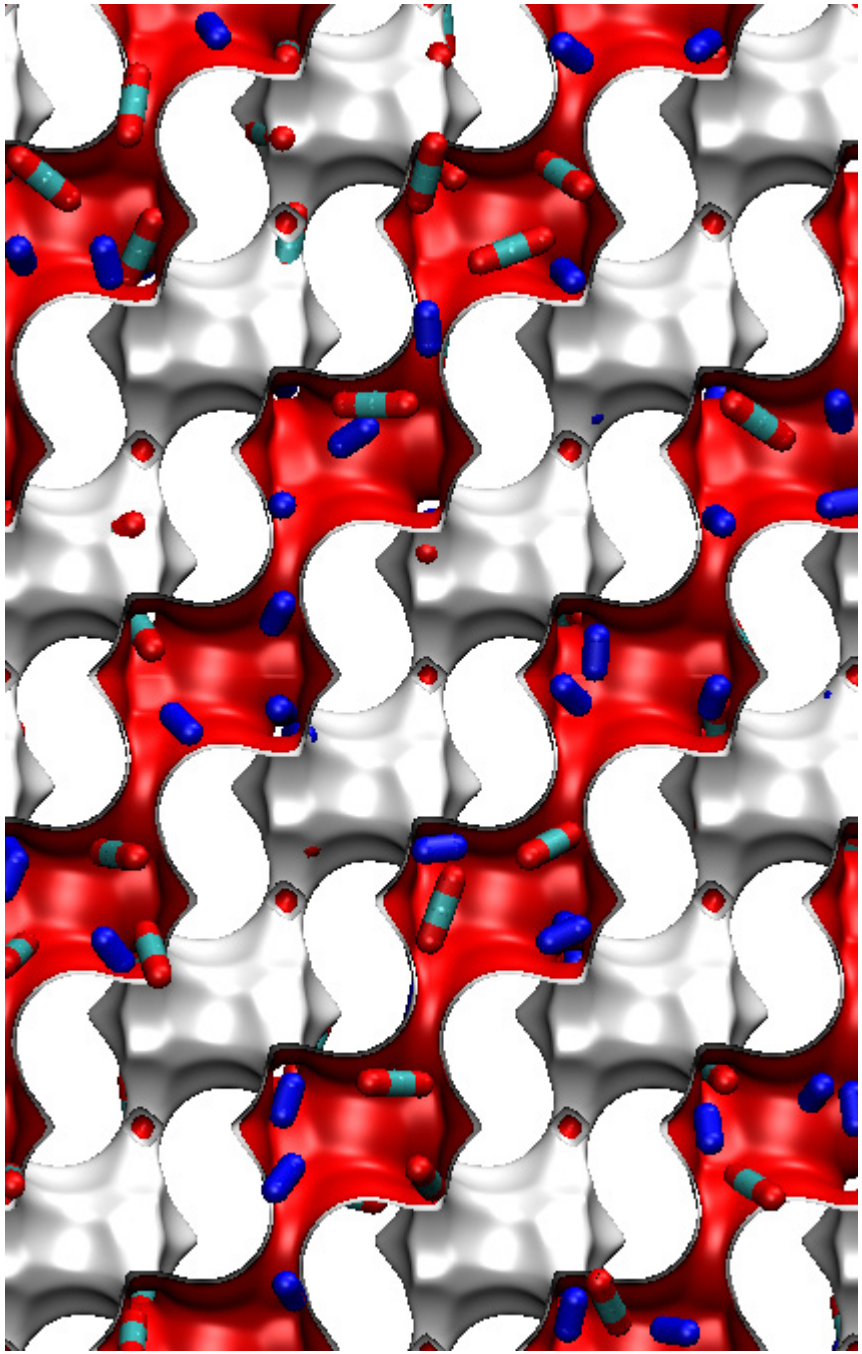

Figure 29

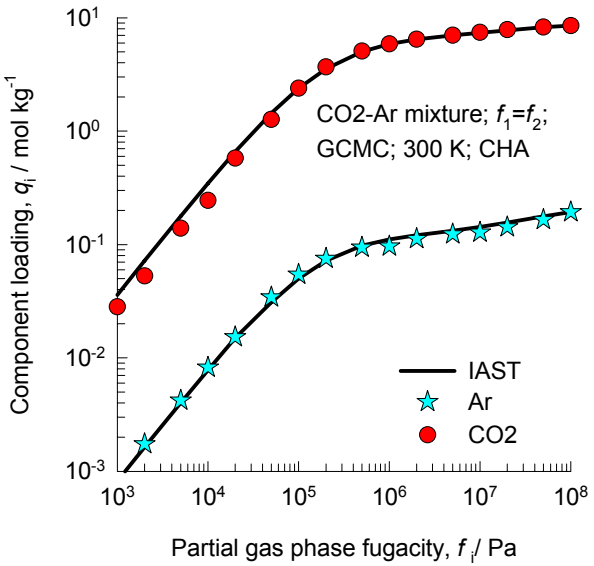
CO2-Ar mixture; f_1=f_2;
GCMC; 300 K; CHA
IAST
Ar
CO2
Component loading, q_i / mol kg^{-1}
Partial gas phase fugacity, f_i / Pa
10^{1}
10^{0}
10^{-1}
10^{-2}
10^{-3}
10^{3}
10^{4}
10^{5}
10^{6}
10^{7}
10^{8}

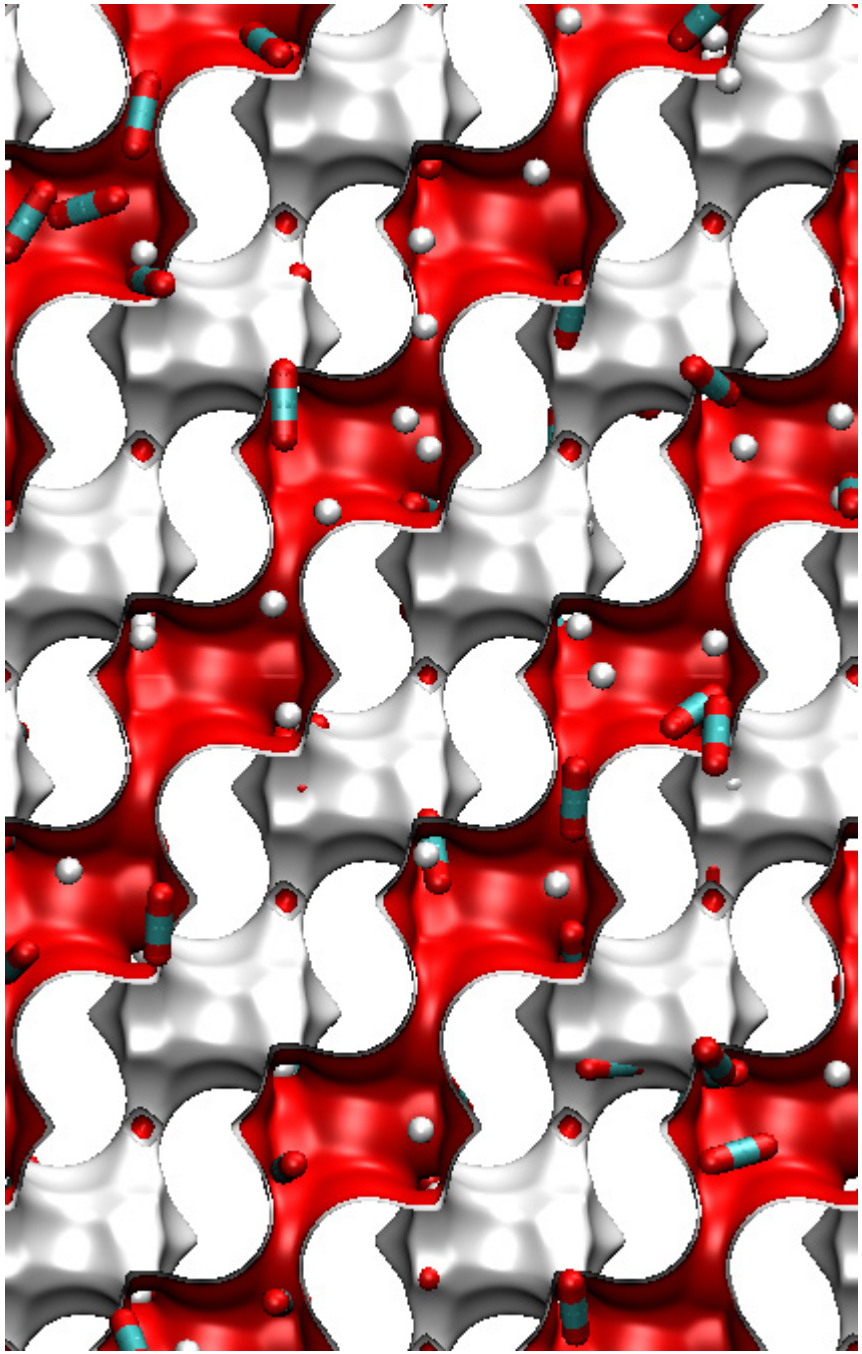

Figure 30

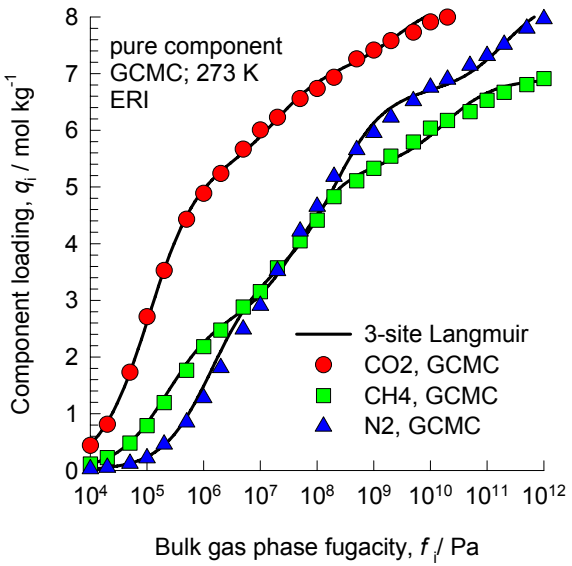
pure component
GCMC; 273 K
ERI
3-site Langmuir
CO2, GCMC
CH4, GCMC
N2, GCMC
Component loading, q_i / mol kg^{-1}
Bulk gas phase fugacity, f_i / Pa

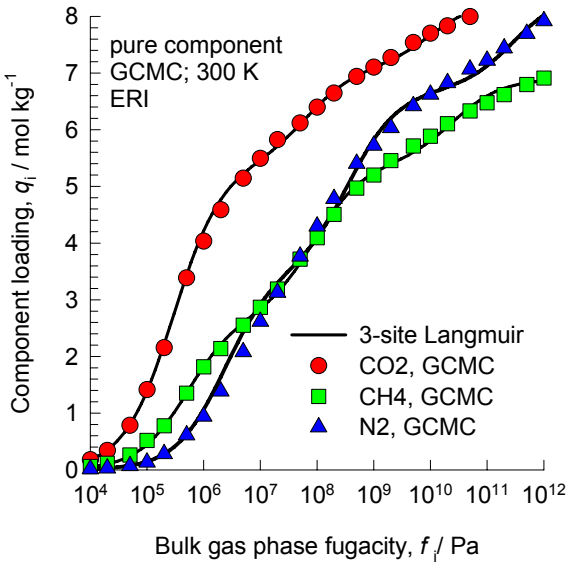
pure component
GCMC; 300 K
ERI
3-site Langmuir
CO2, GCMC
CH4, GCMC
N2, GCMC
Component loading, q_i / mol kg^{-1}
Bulk gas phase fugacity, f_i / Pa

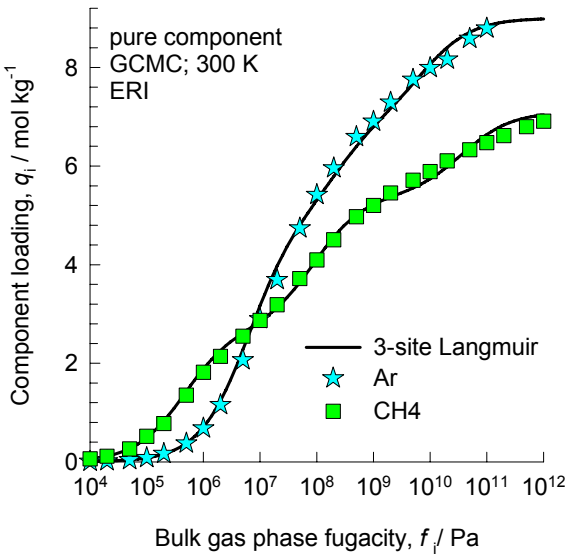
pure component
GCMC; 300 K
ERI
3-site Langmuir
Ar
CH4
Component loading, q_i / mol kg^{-1}
Bulk gas phase fugacity, f_i / Pa

ERI (all silica)

Figure 31

Window of ERI

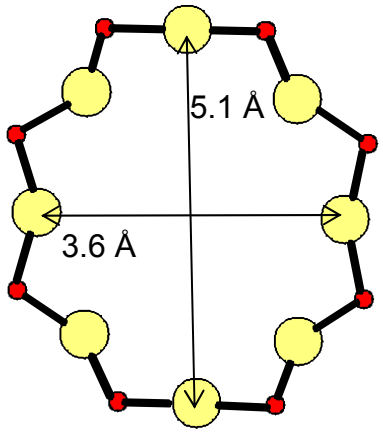

Blue spheres of 4 Å diameter

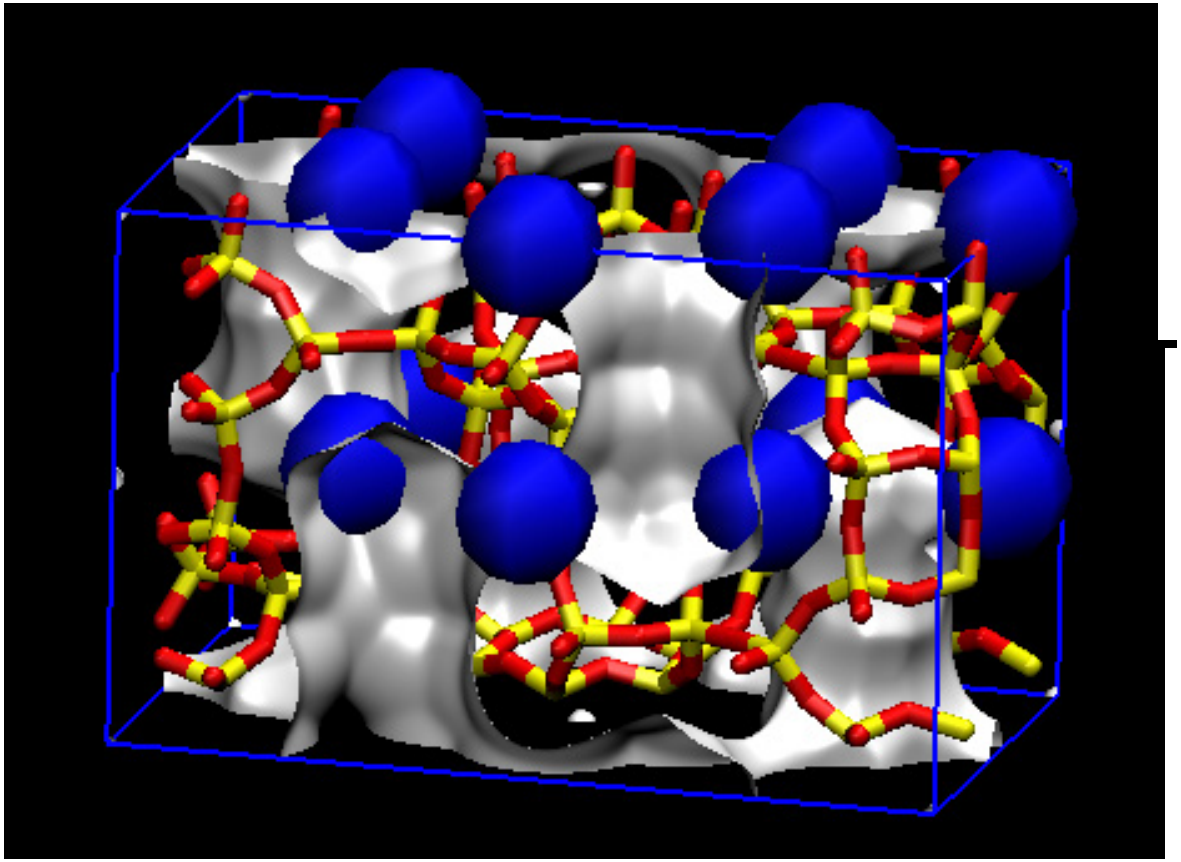

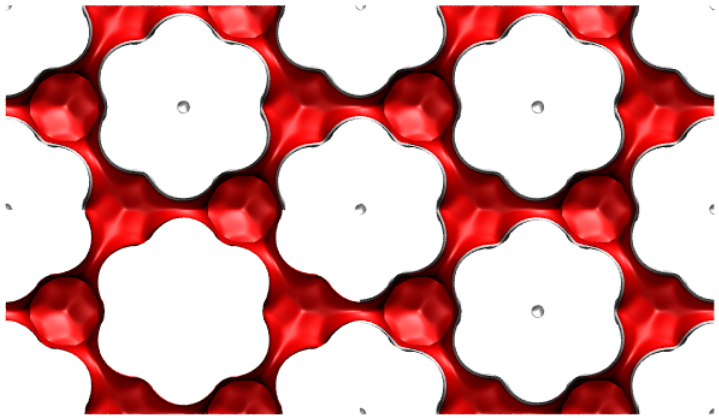

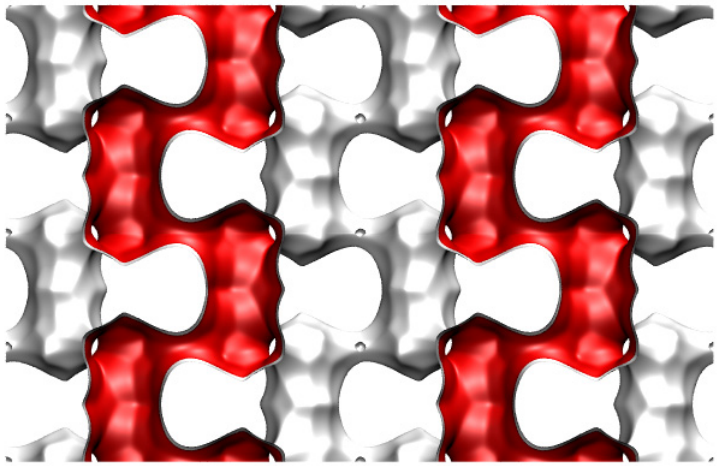

Figure 32

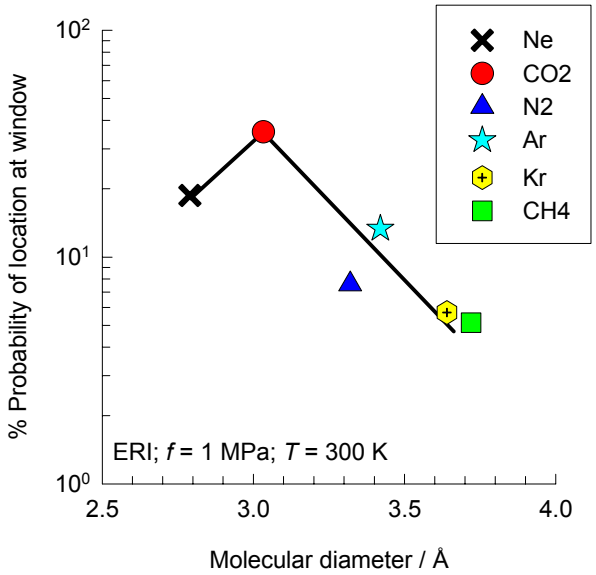
% Probability of location at window
10^2
10^1
10^0
2.5
3.0
3.5
4.0
Molecular diameter / Å
ERI; f = 1 MPa; T = 300 K
Ne
CO2
N2
Ar
Kr
CH4

Figure 33

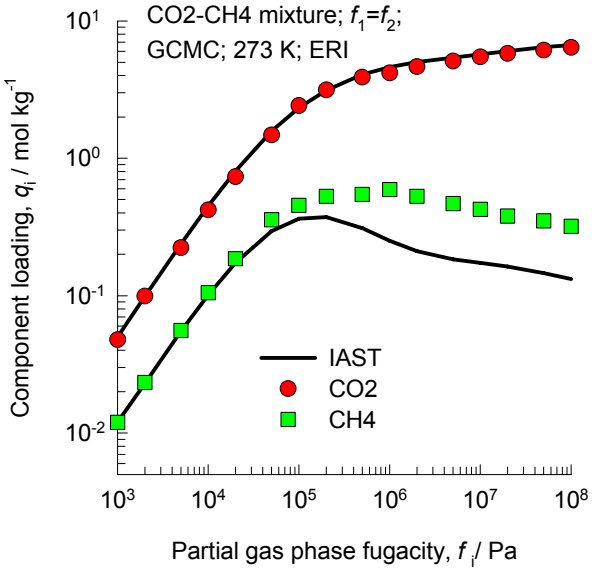

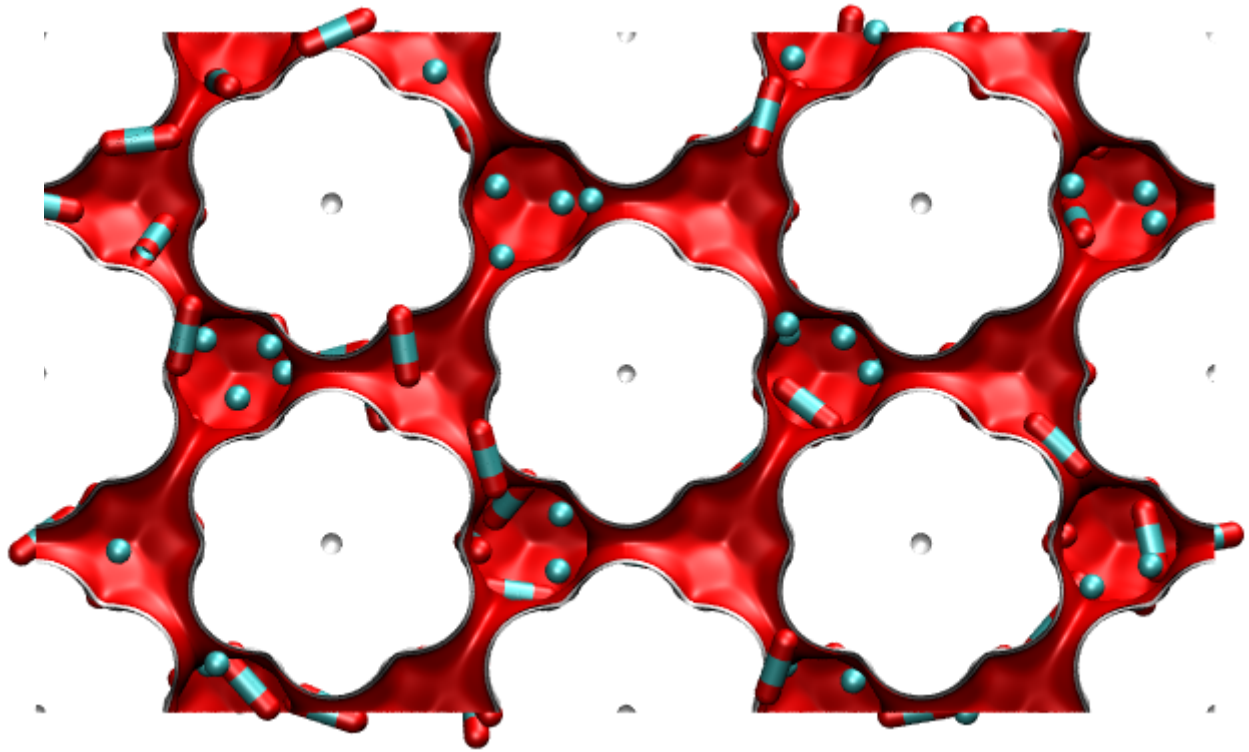

NVT snap with equal loadings
(2 uc deep view of molecules)

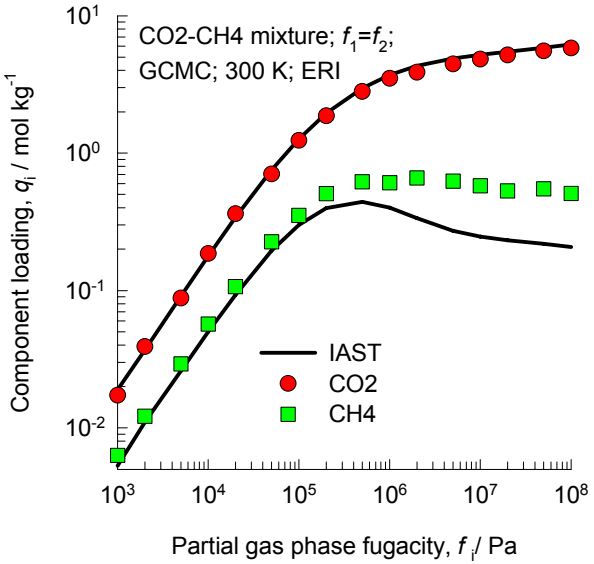

Figure 34

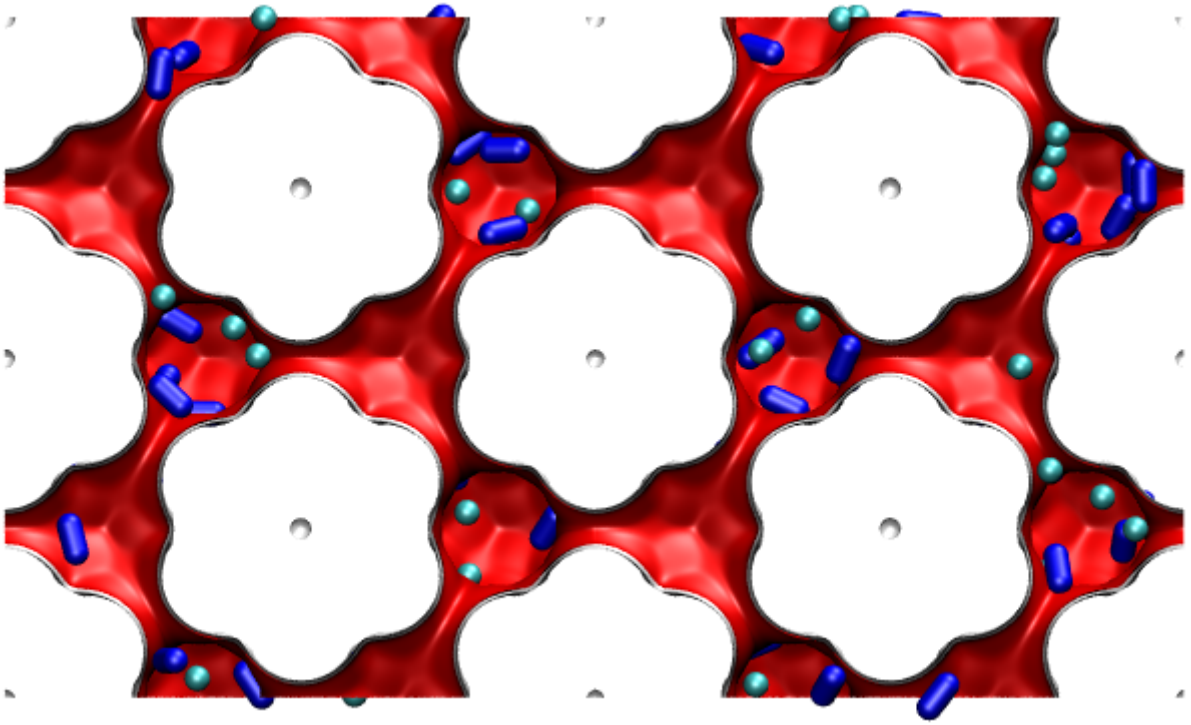

NVT snap with equal loadings
(2 uc deep view of molecules)

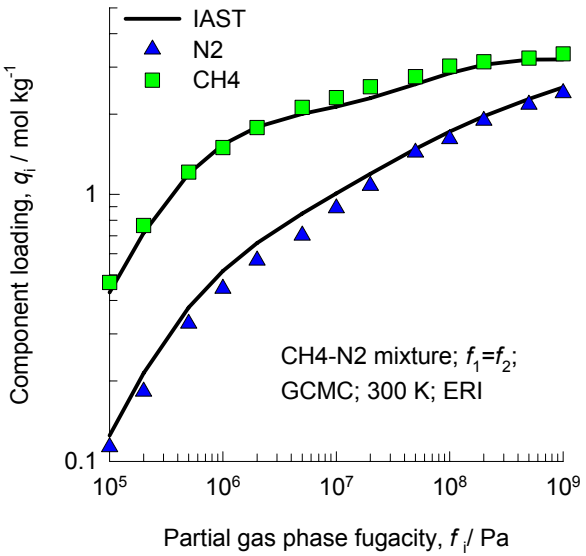

Figure 35

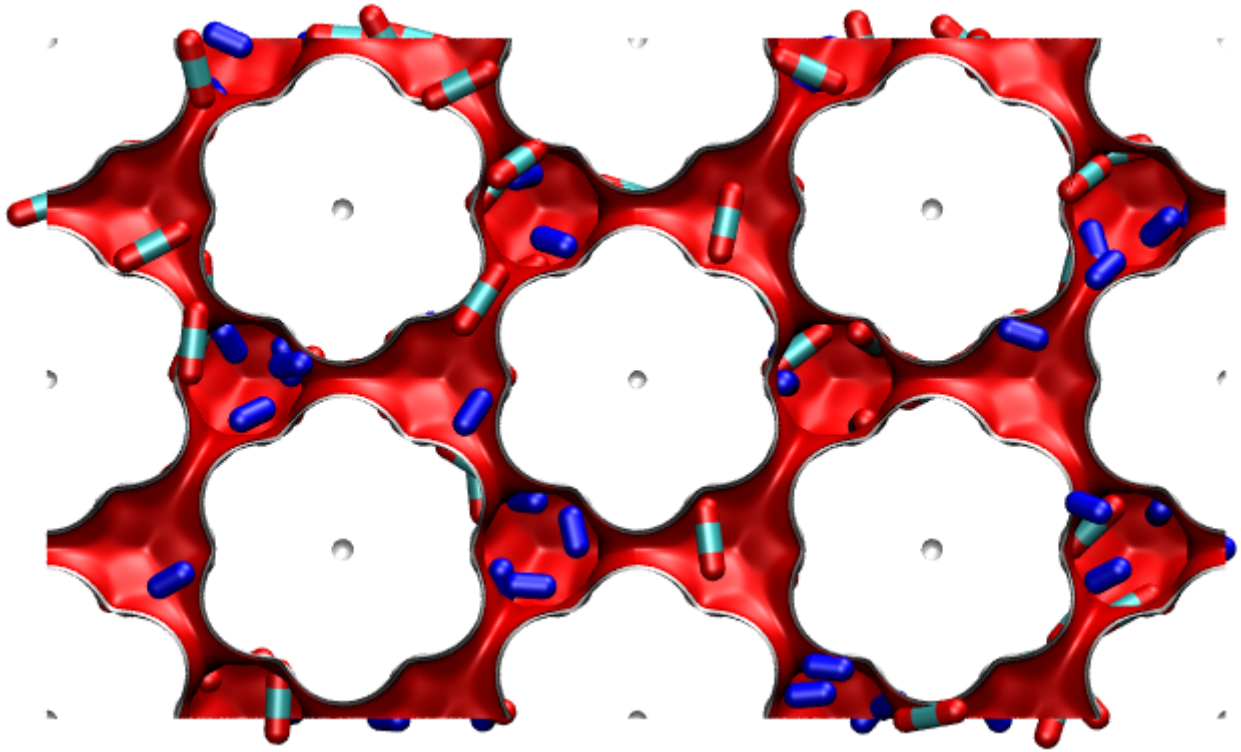

NVT snap with equal loadings
(2 uc deep view of molecules)

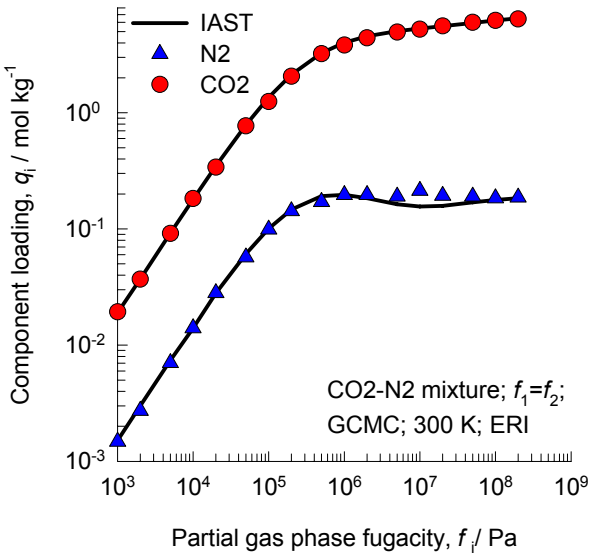

Figure 36

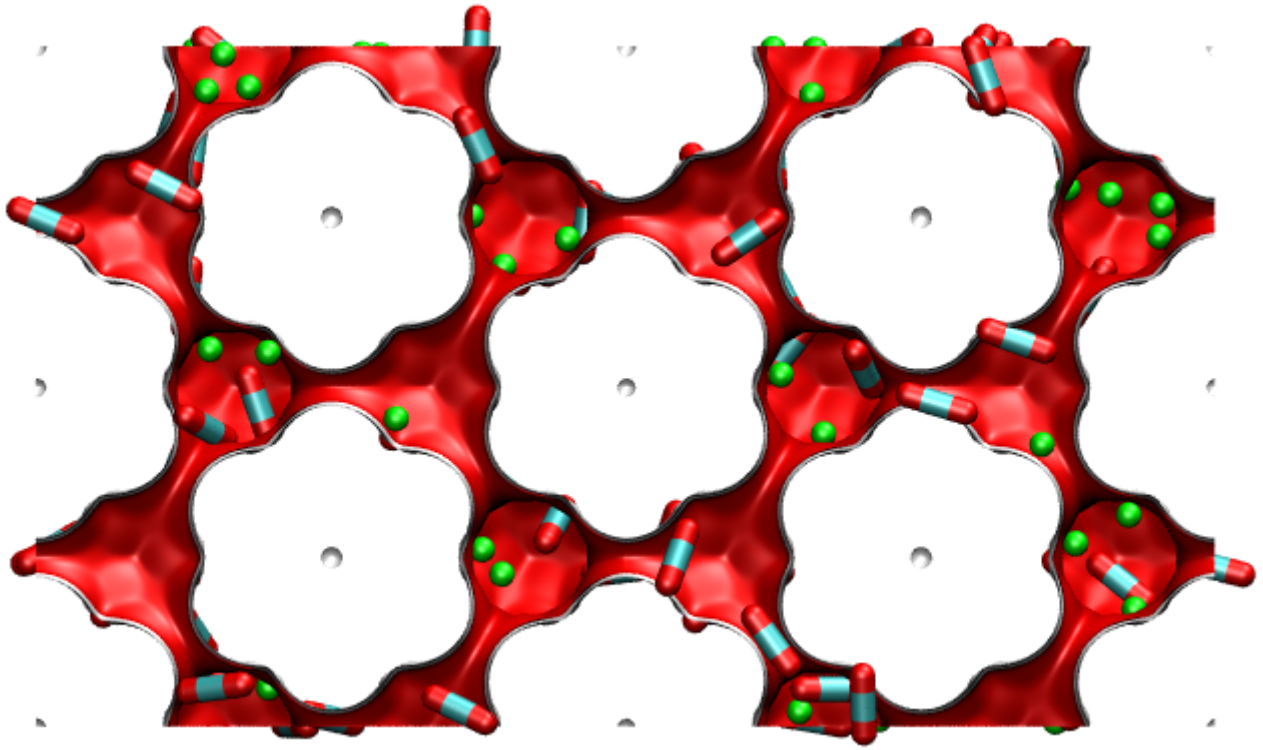

NVT snap with equal loadings
(2 uc deep view of molecules)

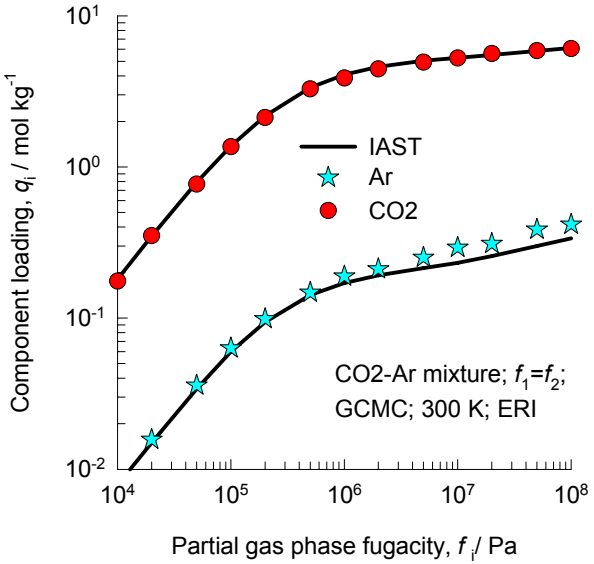

Figure 37

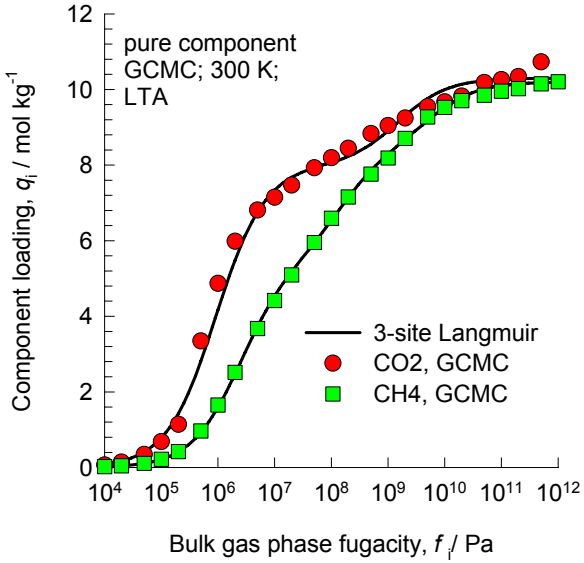
pure component
GCMC; 300 K;
LTA
3-site Langmuir
CO2, GCMC
CH4, GCMC
Component loading, q_i / mol kg^{-1}
Bulk gas phase fugacity, f_i / Pa

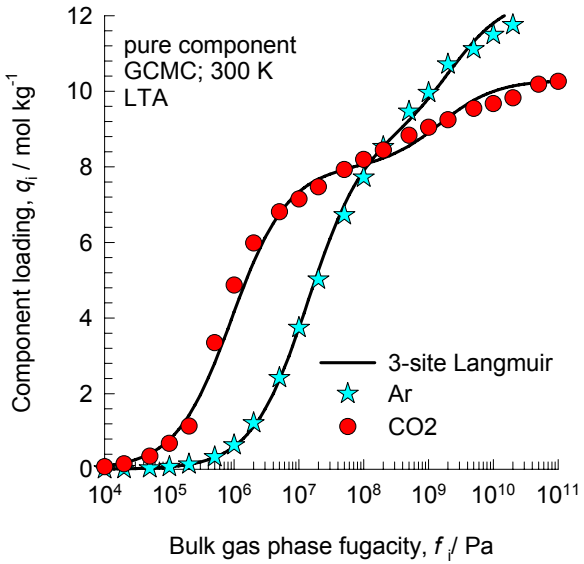
pure component
GCMC; 300 K
LTA
3-site Langmuir
Ar
CO2
Component loading, q_i / mol kg^{-1}
Bulk gas phase fugacity, f_i / Pa

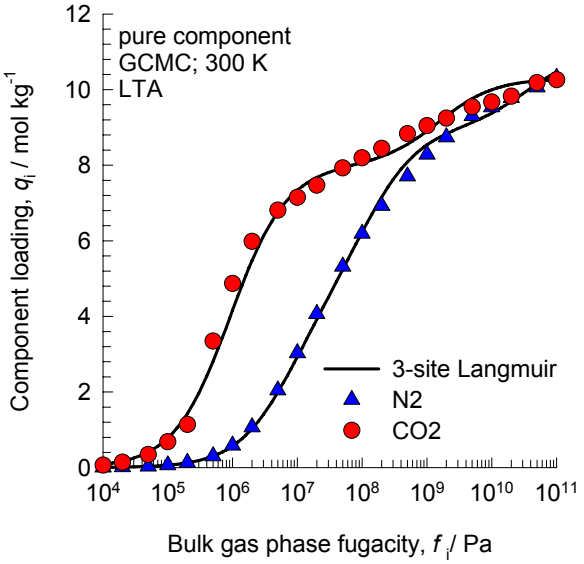
pure component
GCMC; 300 K
LTA
3-site Langmuir
N2
CO2
Component loading, q_i / mol kg^{-1}
Bulk gas phase fugacity, f_i / Pa

Figure 38

LTA (all silica)

Window of LTA

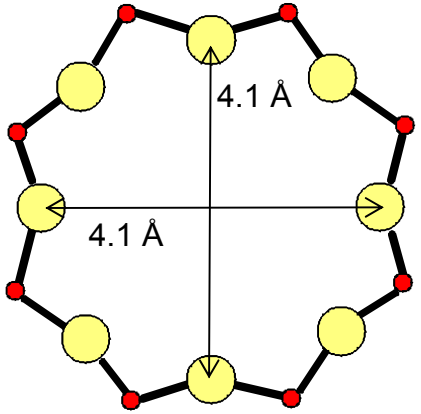

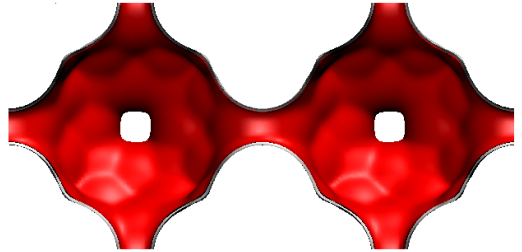

Blue spheres of 4 Å diameter

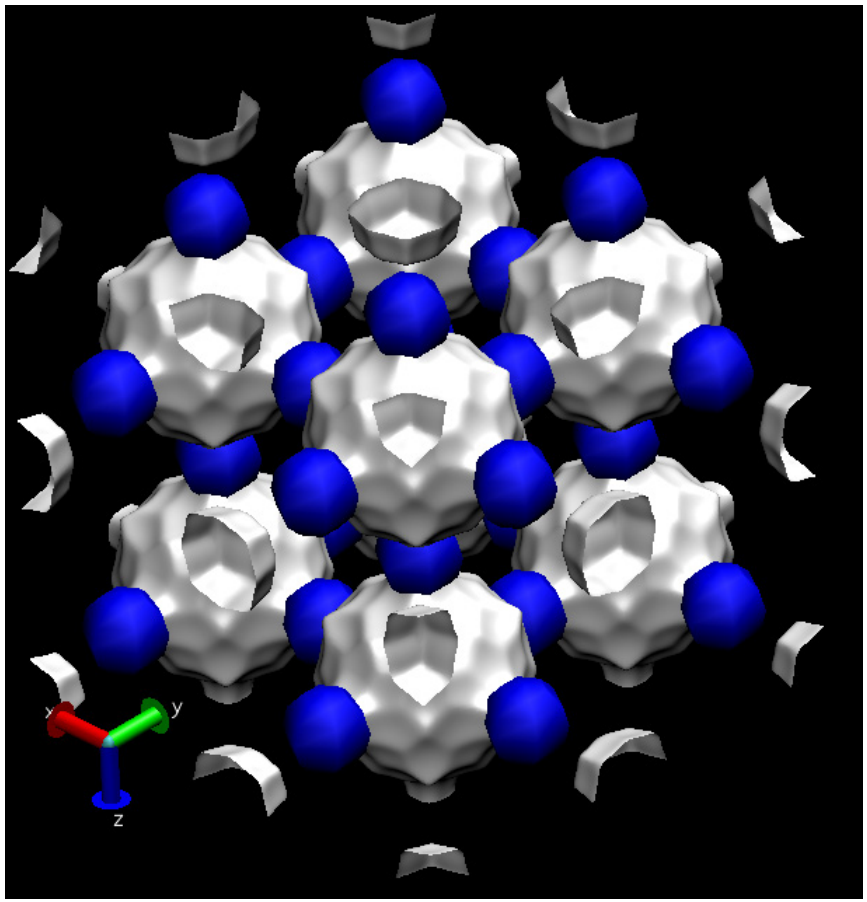

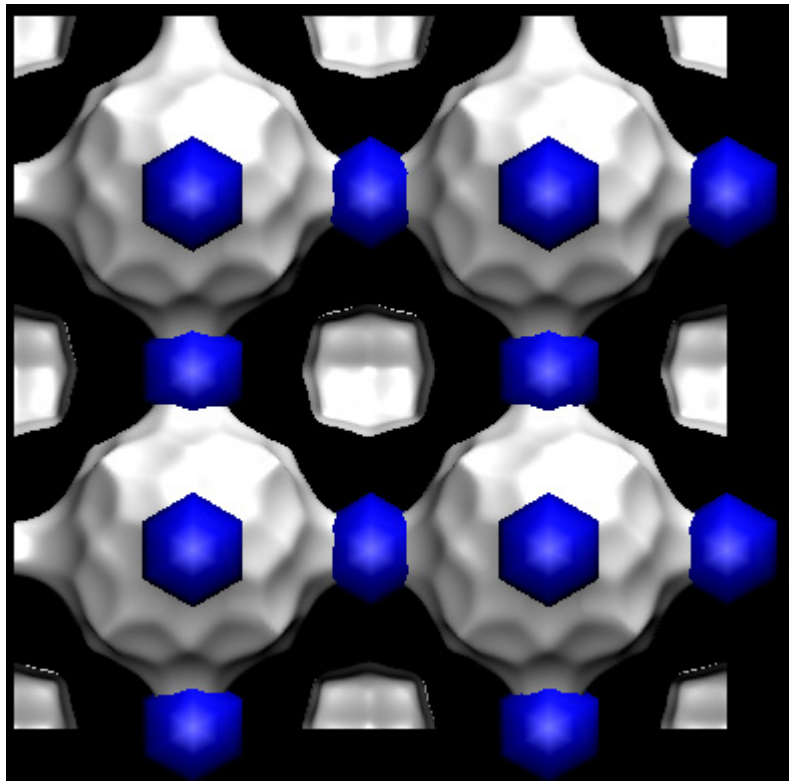

Figure 39

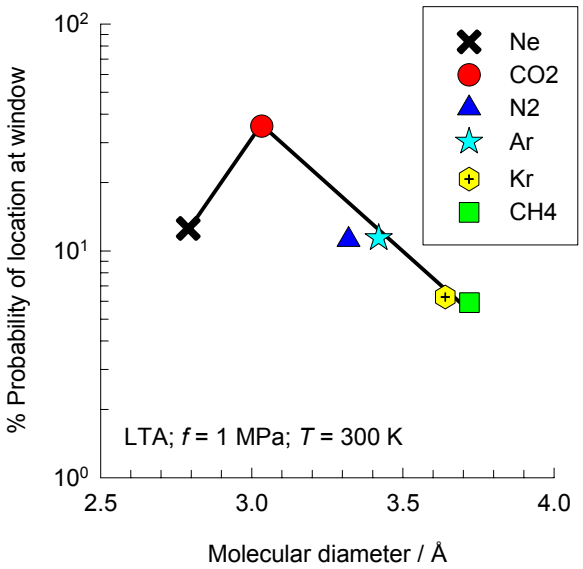
% Probability of location at window
10^2
10^1
10^0
2.5
3.0
3.5
4.0
Molecular diameter / Å
LTA; *f* = 1 MPa; *T* = 300 K
Ne
CO2
N2
Ar
Kr
CH4

Figure 40

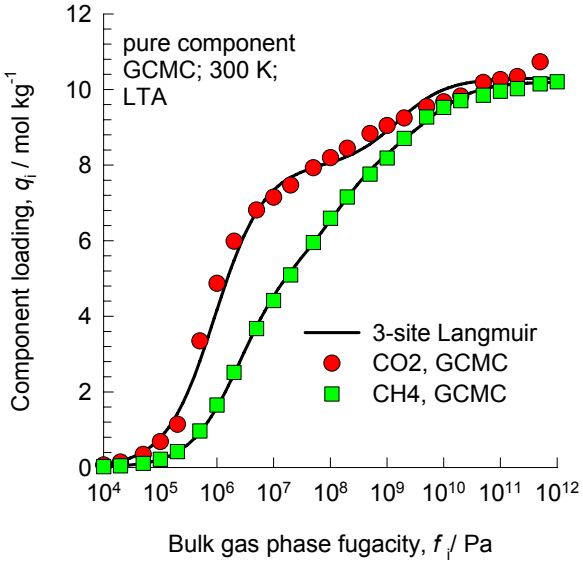

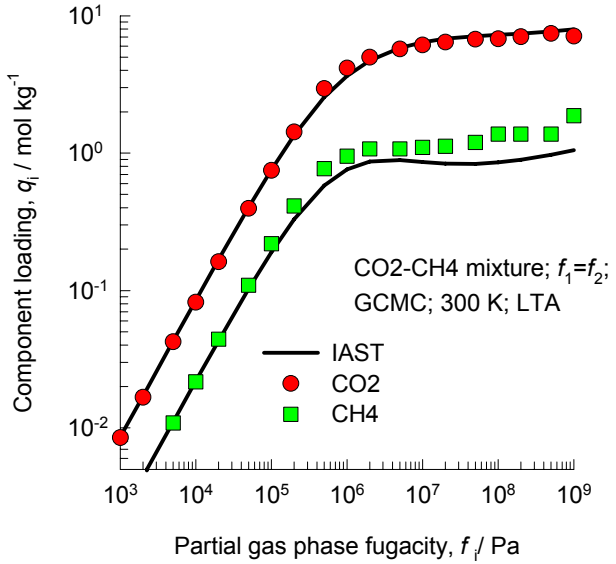

NVT snap with
equal loadings
(2 cages deep view
of molecules)

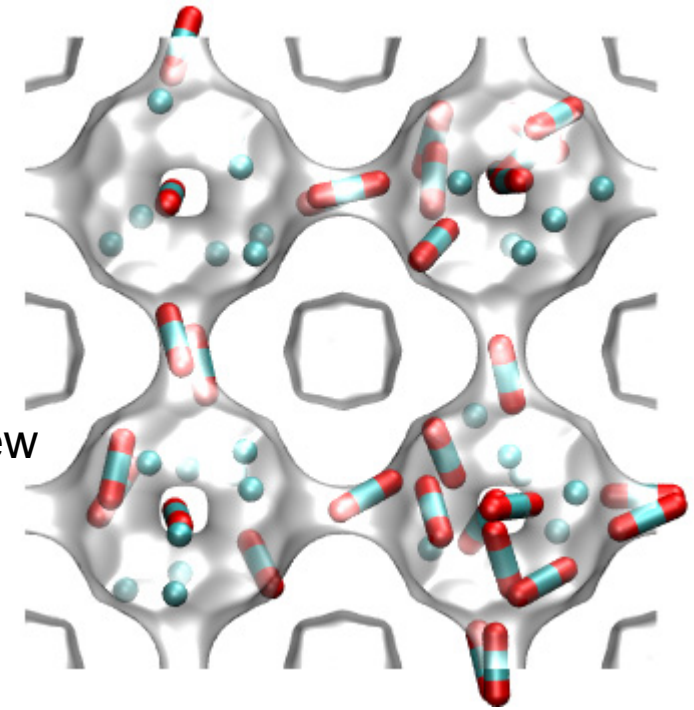

Figure 41

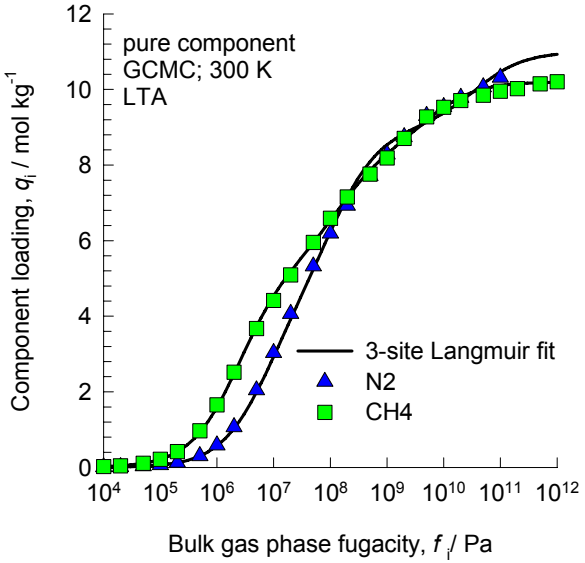

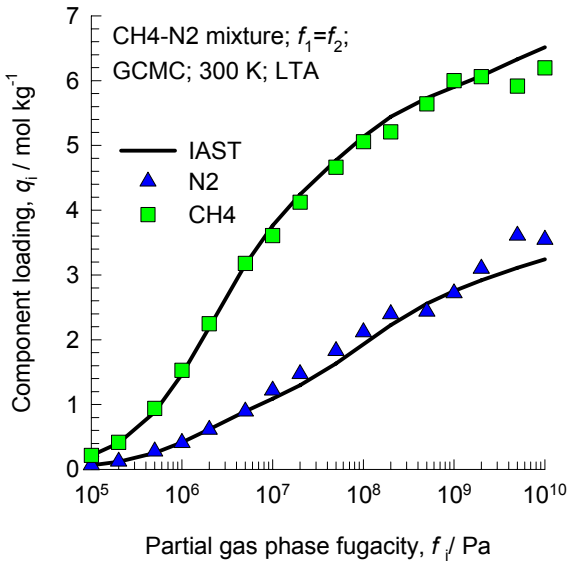

NVT snap with
equal loadings
(2 cages deep view
of molecules)

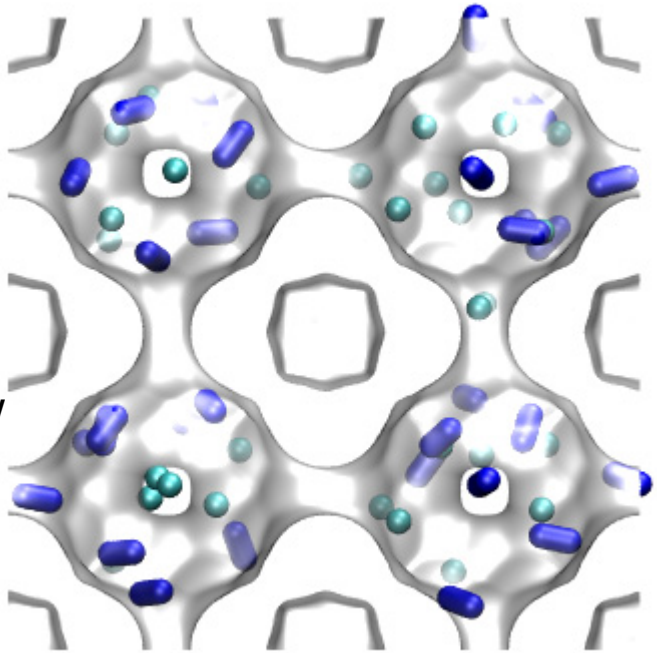

Figure 42

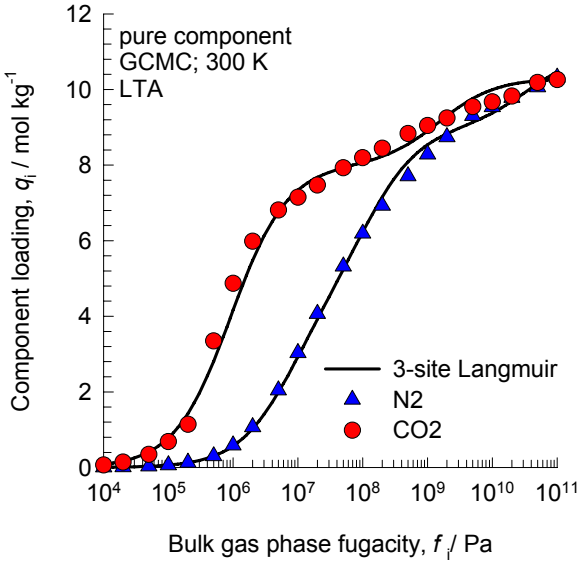

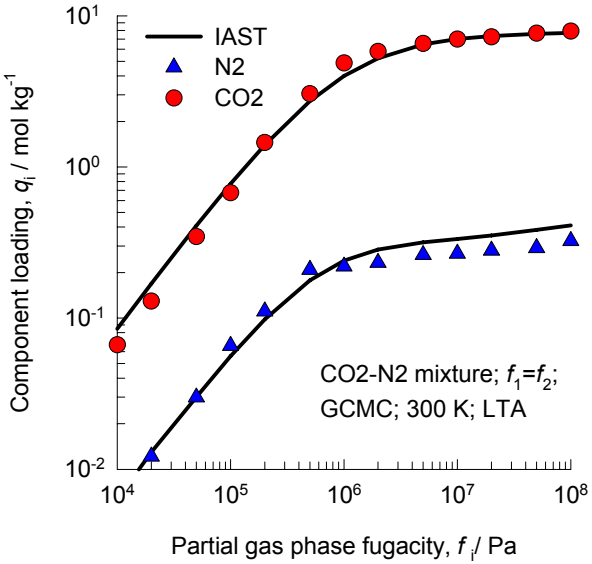

NVT snap with
equal loadings
(2 cages deep view
of molecules)

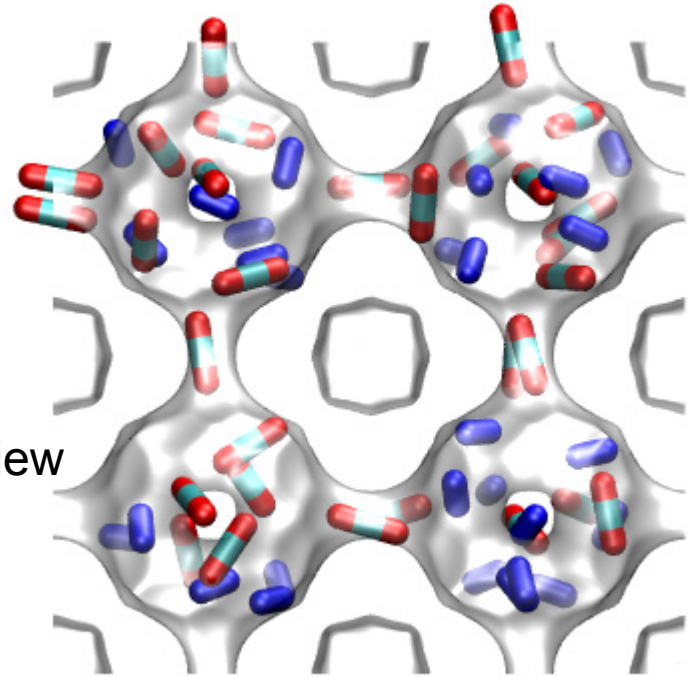

Figure 43

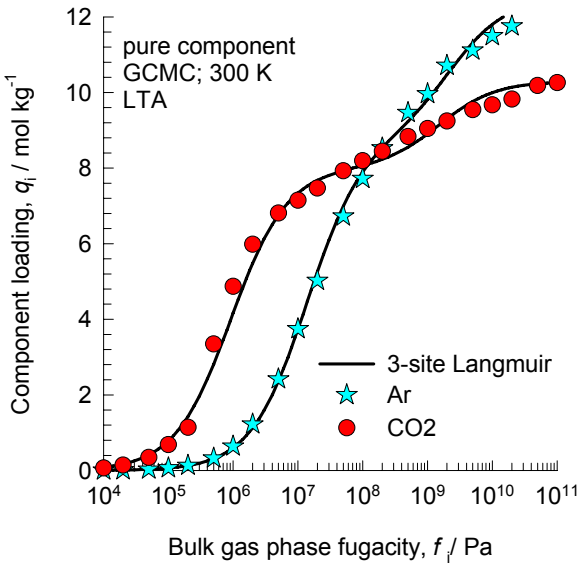

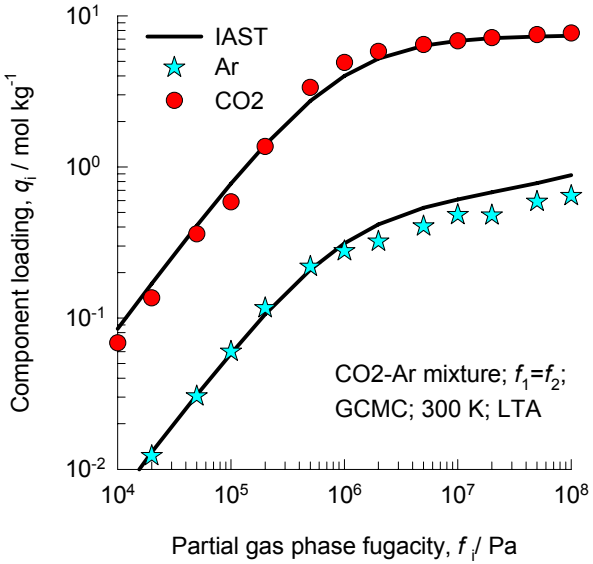

NVT snap with
equal loadings
(2 cages deep view
of molecules)

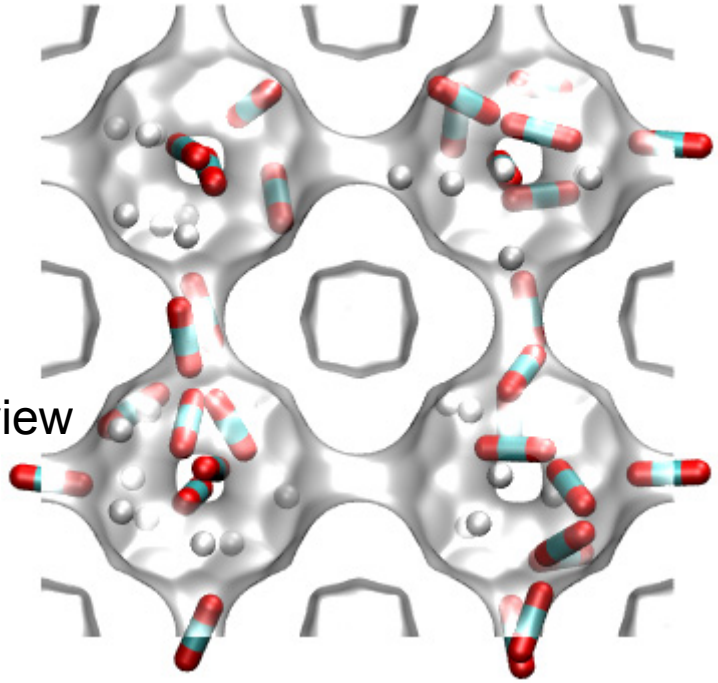

Figure 44

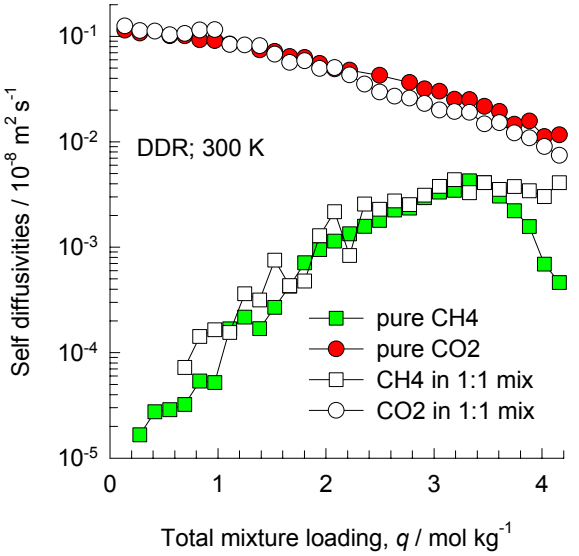
DDR; 300 K
pure CH4
pure CO2
CH4 in 1:1 mix
CO2 in 1:1 mix
Self diffusivities / 10^-8 m^2 s^-1
Total mixture loading, q / mol kg^-1

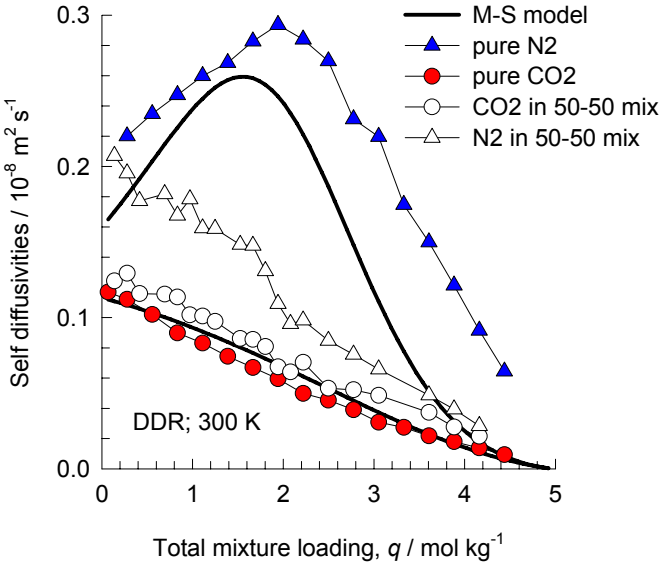
M-S model
pure N2
pure CO2
CO2 in 50-50 mix
N2 in 50-50 mix
DDR; 300 K
Self diffusivities / 10^-8 m^2 s^-1
Total mixture loading, q / mol kg^-1

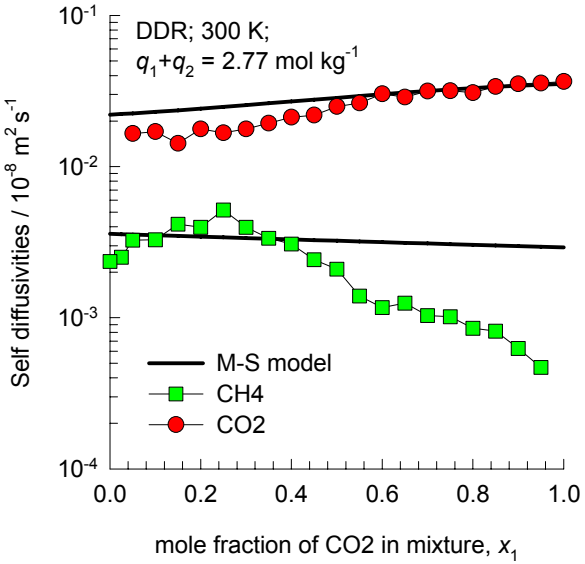
DDR; 300 K;
q1+q2 = 2.77 mol kg^-1
M-S model
CH4
CO2
Self diffusivities / 10^-8 m^2 s^-1
mole fraction of CO2 in mixture, x1

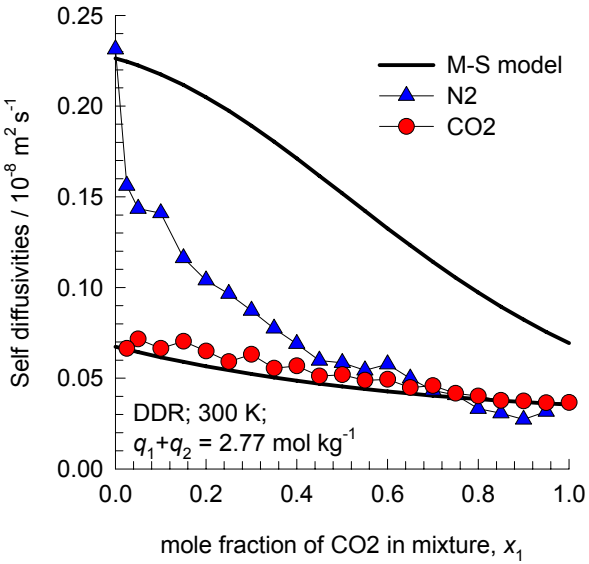
M-S model
N2
CO2
DDR; 300 K;
q1+q2 = 2.77 mol kg^-1
Self diffusivities / 10^-8 m^2 s^-1
mole fraction of CO2 in mixture, x1

Figure 45

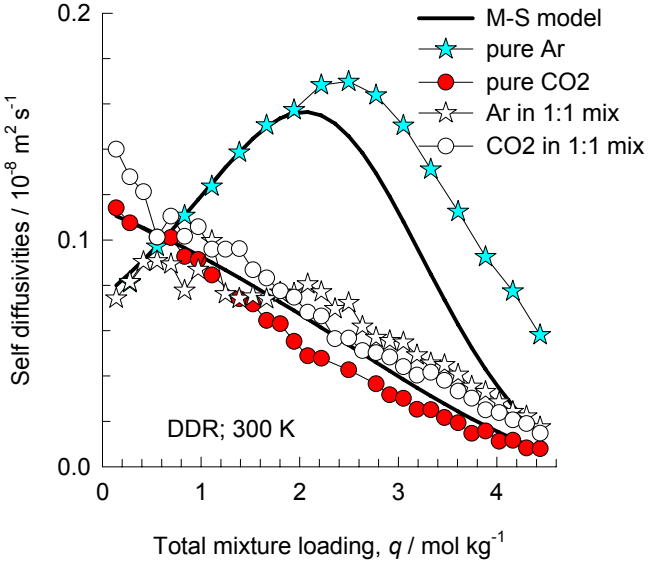
M-S model
pure Ar
pure CO2
Ar in 1:1 mix
CO2 in 1:1 mix
DDR; 300 K
Self diffusivities / 10^-8 m^2 s^-1
Total mixture loading, q / mol kg^-1

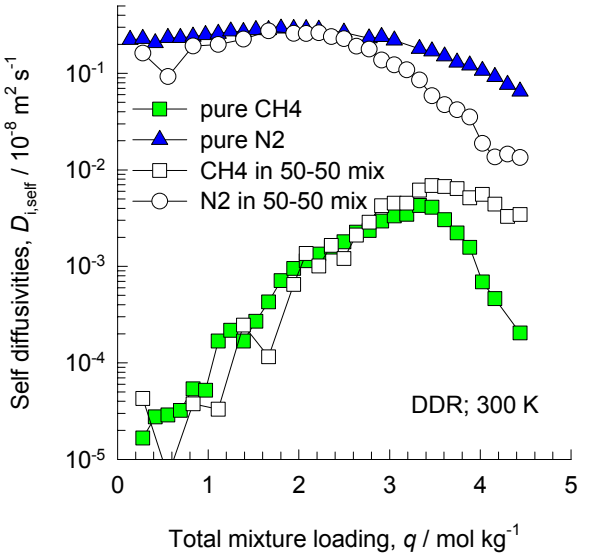
pure CH4
pure N2
CH4 in 50-50 mix
N2 in 50-50 mix
DDR; 300 K
Self diffusivities, D_i,self / 10^-8 m^2 s^-1
Total mixture loading, q / mol kg^-1

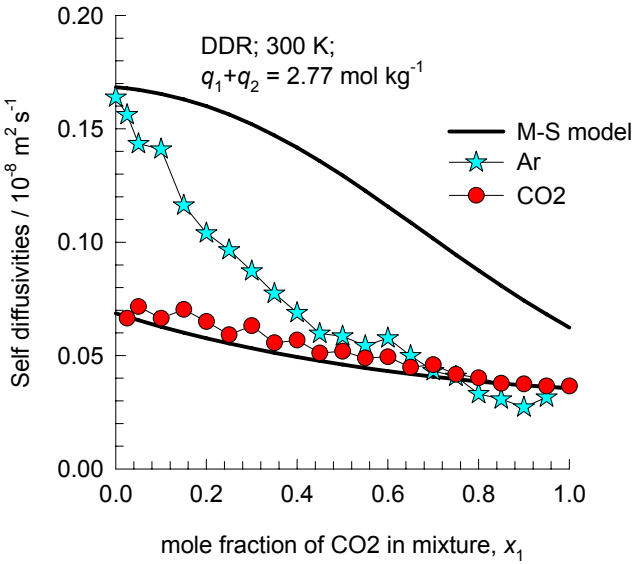
DDR; 300 K;
q1+q2 = 2.77 mol kg^-1
M-S model
Ar
CO2
Self diffusivities / 10^-8 m^2 s^-1
mole fraction of CO2 in mixture, x1

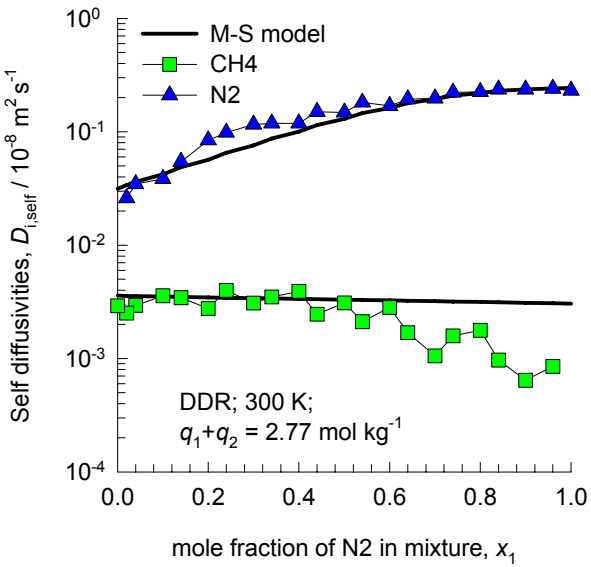
M-S model
CH4
N2
DDR; 300 K;
q1+q2 = 2.77 mol kg^-1
Self diffusivities, D_i,self / 10^-8 m^2 s^-1
mole fraction of N2 in mixture, x1

Figure 46

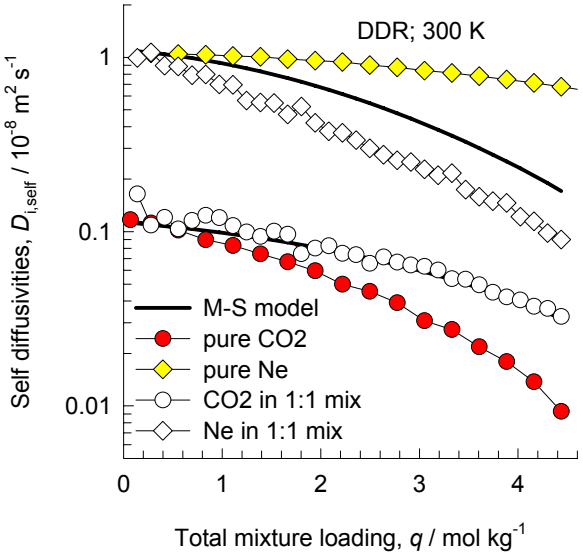
DDR; 300 K
Self diffusivities, $D_{i,self}$ / 10^{-8} m^2 s^{-1}
Total mixture loading, q / mol kg^{-1}
M-S model
pure CO2
pure Ne
CO2 in 1:1 mix
Ne in 1:1 mix

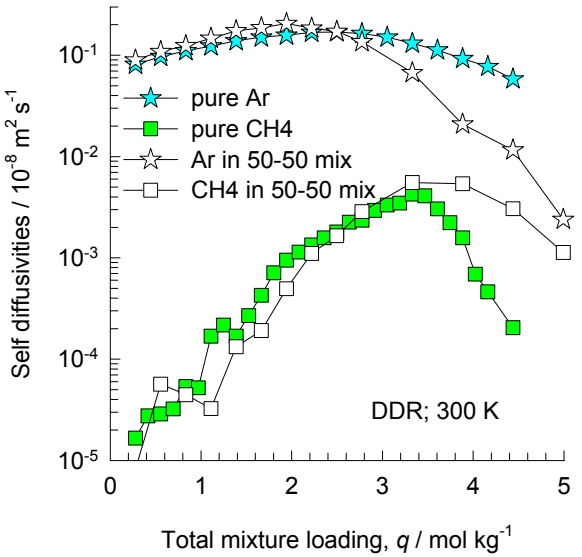
pure Ar
pure CH4
Ar in 50-50 mix
CH4 in 50-50 mix
DDR; 300 K
Self diffusivities / 10^{-8} m^2 s^{-1}
Total mixture loading, q / mol kg^{-1}

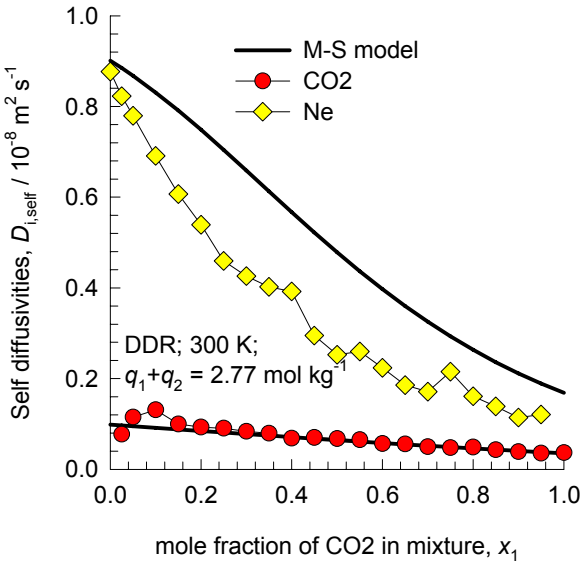
M-S model
CO2
Ne
DDR; 300 K;
q_1+q_2 = 2.77 mol kg^{-1}
Self diffusivities, $D_{i,self}$ / 10^{-8} m^2 s^{-1}
mole fraction of CO2 in mixture, x_1

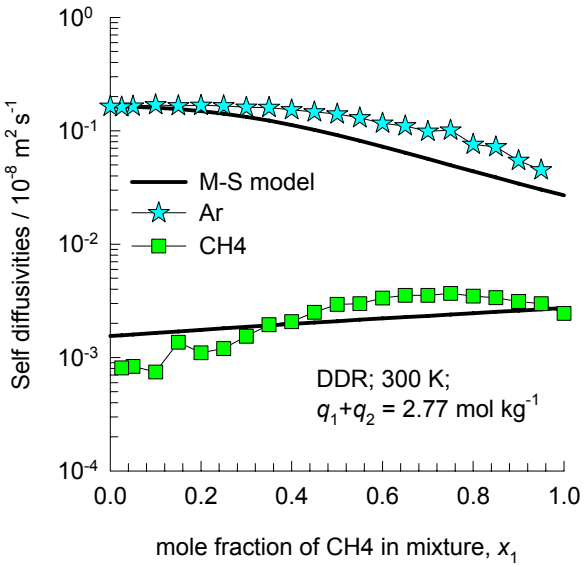
M-S model
Ar
CH4
DDR; 300 K;
q_1+q_2 = 2.77 mol kg^{-1}
Self diffusivities / 10^{-8} m^2 s^{-1}
mole fraction of CH4 in mixture, x_1

Figure 47

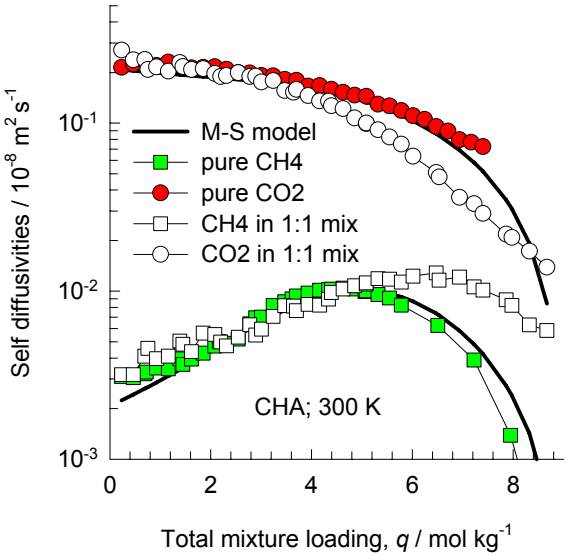
Self diffusivities / 10^-8 m^2 s^-1
10^-1
10^-2
10^-3
M-S model
pure CH4
pure CO2
CH4 in 1:1 mix
CO2 in 1:1 mix
CHA; 300 K
0
2
4
6
8
Total mixture loading, q / mol kg^-1

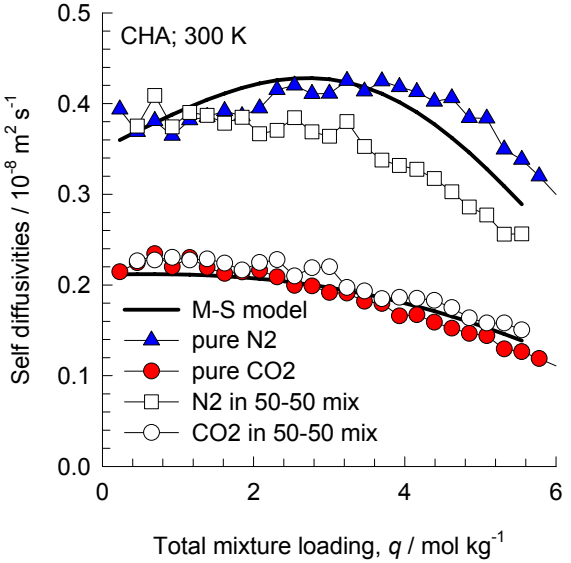
CHA; 300 K
Self diffusivities / 10^-8 m^2 s^-1
0.5
0.4
0.3
0.2
0.1
0.0
M-S model
pure N2
pure CO2
N2 in 50-50 mix
CO2 in 50-50 mix
0
2
4
6
Total mixture loading, q / mol kg^-1

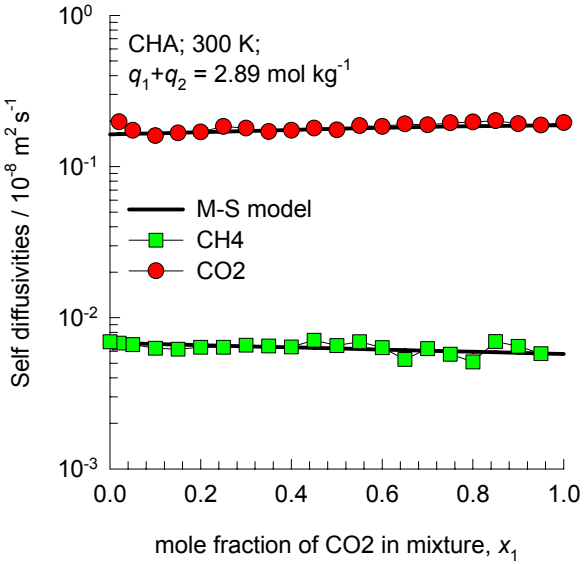
CHA; 300 K;
q1+q2 = 2.89 mol kg^-1
Self diffusivities / 10^-8 m^2 s^-1
10^0
10^-1
10^-2
10^-3
M-S model
CH4
CO2
0.0
0.2
0.4
0.6
0.8
1.0
mole fraction of CO2 in mixture, x1

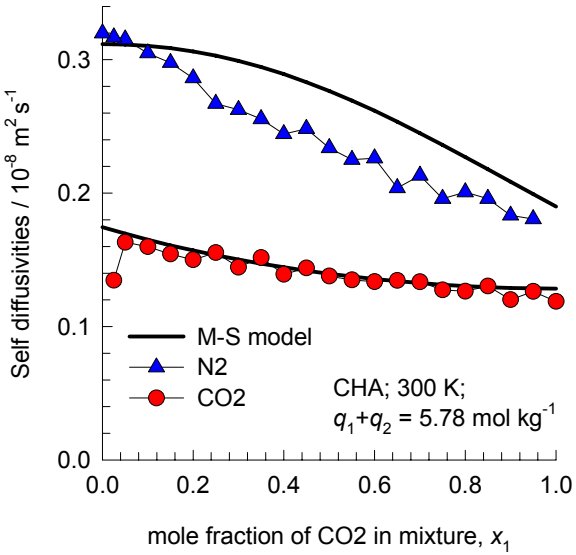
Self diffusivities / 10^-8 m^2 s^-1
0.3
0.2
0.1
0.0
M-S model
N2
CO2
CHA; 300 K;
q1+q2 = 5.78 mol kg^-1
0.0
0.2
0.4
0.6
0.8
1.0
mole fraction of CO2 in mixture, x1

Figure 48

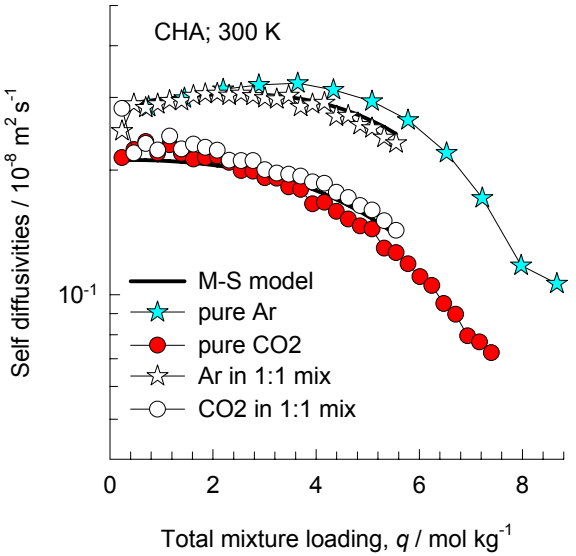
CHA; 300 K
Self diffusivities / 10^-8 m^2 s^-1
10^-1
M-S model
pure Ar
pure CO2
Ar in 1:1 mix
CO2 in 1:1 mix
0
2
4
6
8
Total mixture loading, q / mol kg^-1

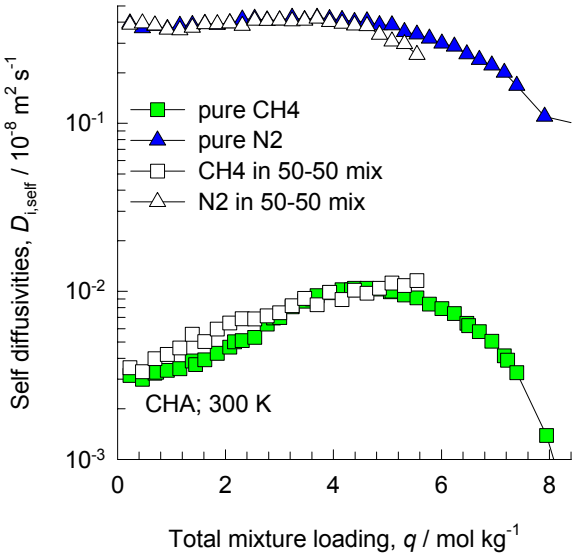
Self diffusivities, D_i,self / 10^-8 m^2 s^-1
10^-1
10^-2
10^-3
pure CH4
pure N2
CH4 in 50-50 mix
N2 in 50-50 mix
CHA; 300 K
0
2
4
6
8
Total mixture loading, q / mol kg^-1

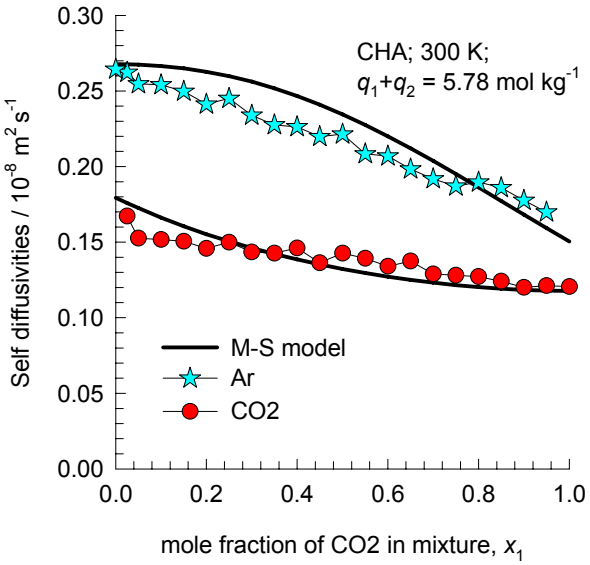
Self diffusivities / 10^-8 m^2 s^-1
0.30
0.25
0.20
0.15
0.10
0.05
0.00
CHA; 300 K;
q1+q2 = 5.78 mol kg^-1
M-S model
Ar
CO2
0.0
0.2
0.4
0.6
0.8
1.0
mole fraction of CO2 in mixture, x1

Figure 49

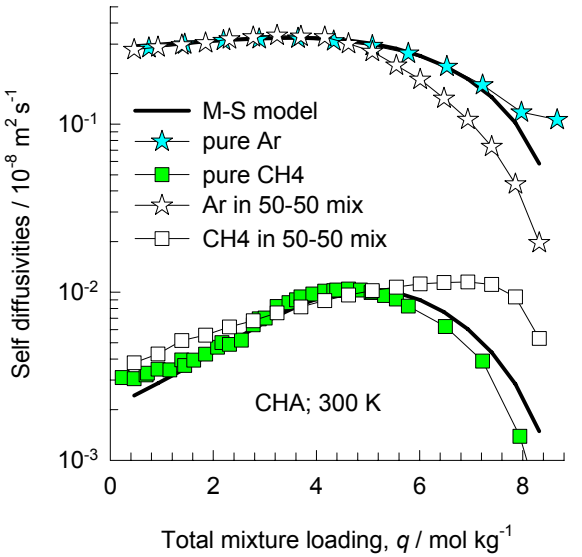
M-S model
pure Ar
pure CH4
Ar in 50-50 mix
CH4 in 50-50 mix
CHA; 300 K
Self diffusivities / 10^-8 m^2 s^-1
Total mixture loading, q / mol kg^-1

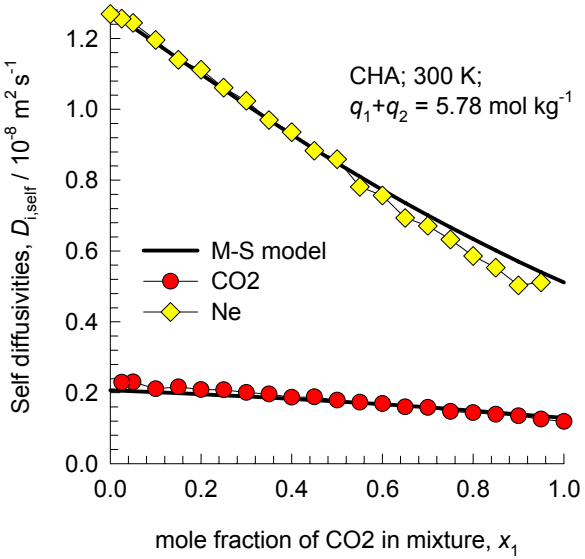
CHA; 300 K;
q1+q2 = 5.78 mol kg^-1
M-S model
CO2
Ne
Self diffusivities, D_i,self / 10^-8 m^2 s^-1
mole fraction of CO2 in mixture, x1

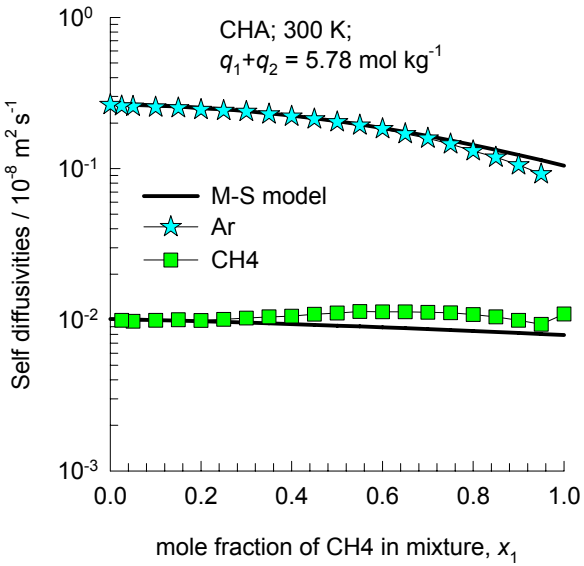
CHA; 300 K;
q1+q2 = 5.78 mol kg^-1
M-S model
Ar
CH4
Self diffusivities / 10^-8 m^2 s^-1
mole fraction of CH4 in mixture, x1

Figure 50

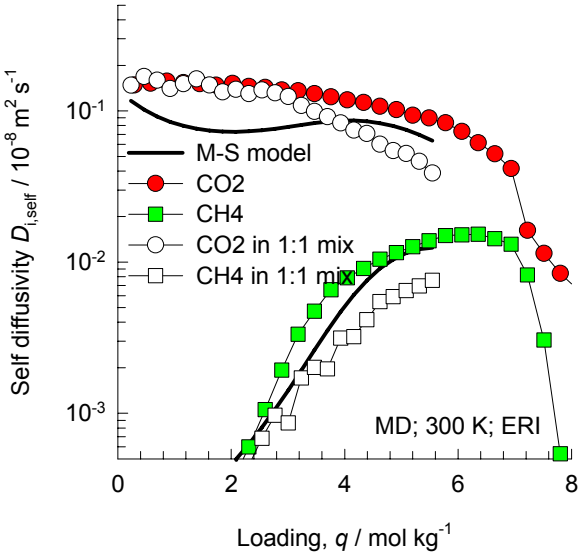
Self diffusivity $D_{i,self}$ / 10^{-8} m^2 s^{-1}
10^{-1}
10^{-2}
10^{-3}
M-S model
CO2
CH4
CO2 in 1:1 mix
CH4 in 1:1 mix
MD; 300 K; ERI
0
2
4
6
8
Loading, q / mol kg^{-1}

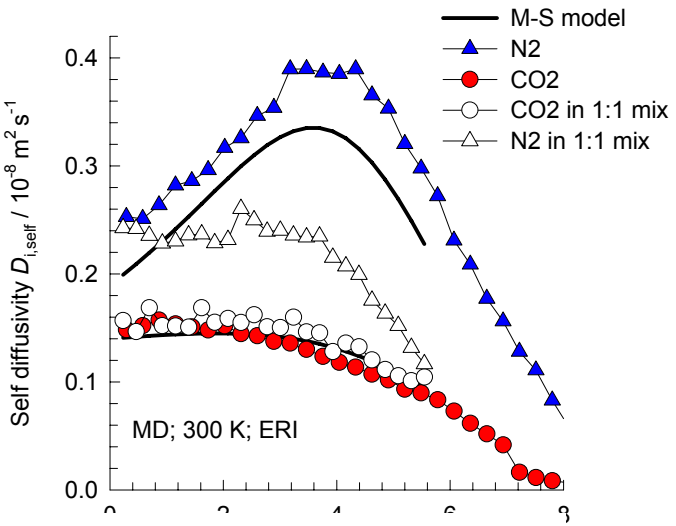
Self diffusivity $D_{i,self}$ / 10^{-8} m^2 s^{-1}
0.4
0.3
0.2
0.1
0.0
M-S model
N2
CO2
CO2 in 1:1 mix
N2 in 1:1 mix
MD; 300 K; ERI

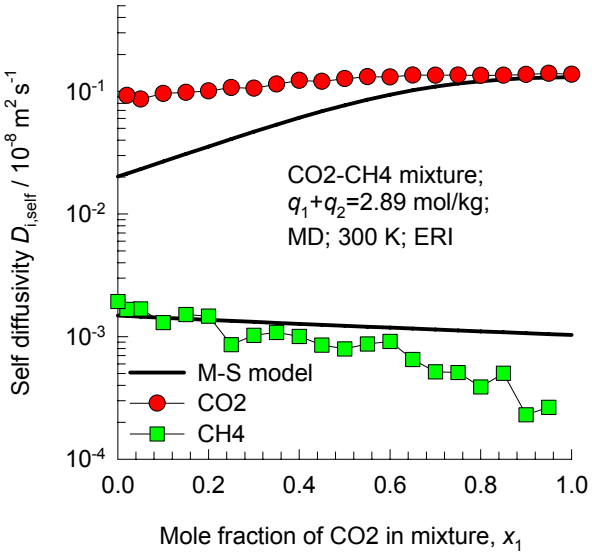
Self diffusivity $D_{i,self}$ / 10^{-8} m^2 s^{-1}
10^{-1}
10^{-2}
10^{-3}
10^{-4}
CO2-CH4 mixture;
q_1+q_2=2.89 mol/kg;
MD; 300 K; ERI
M-S model
CO2
CH4
0.0
0.2
0.4
0.6
0.8
1.0
Mole fraction of CO2 in mixture, x_1

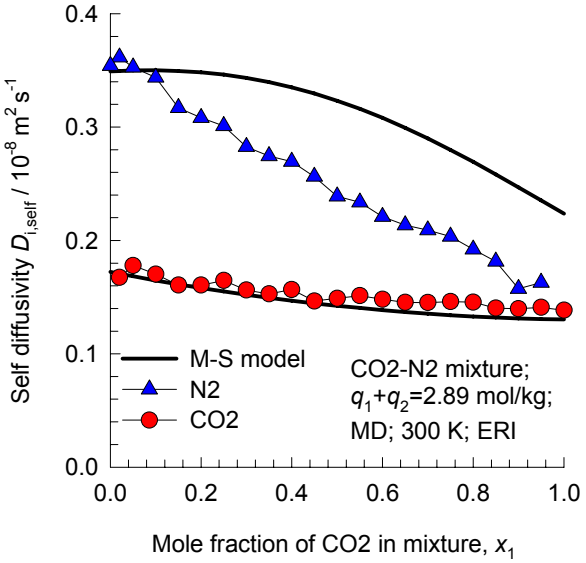
Self diffusivity $D_{i,self}$ / 10^{-8} m^2 s^{-1}
0.4
0.3
0.2
0.1
0.0
M-S model
N2
CO2
CO2-N2 mixture;
q_1+q_2=2.89 mol/kg;
MD; 300 K; ERI
0.0
0.2
0.4
0.6
0.8
1.0
Mole fraction of CO2 in mixture, x_1

Figure 51

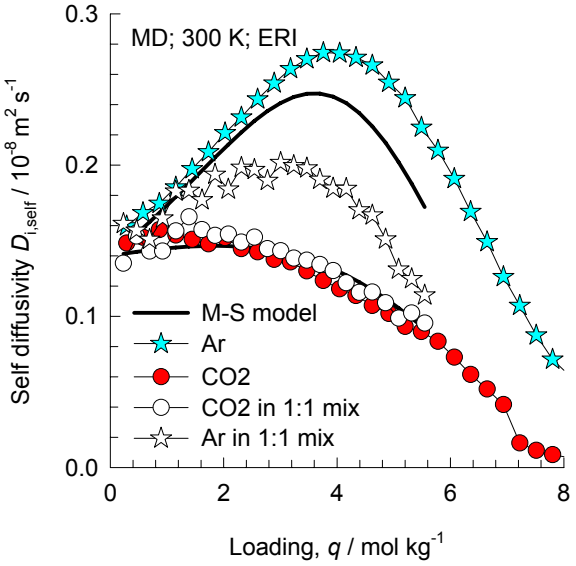
MD; 300 K; ERI
M-S model
Ar
CO2
CO2 in 1:1 mix
Ar in 1:1 mix
Self diffusivity $D_{i,self}$ / 10^{-8} m^2 s^{-1}
Loading, q / mol kg^{-1}
0.0
0.1
0.2
0.3
0
2
4
6
8

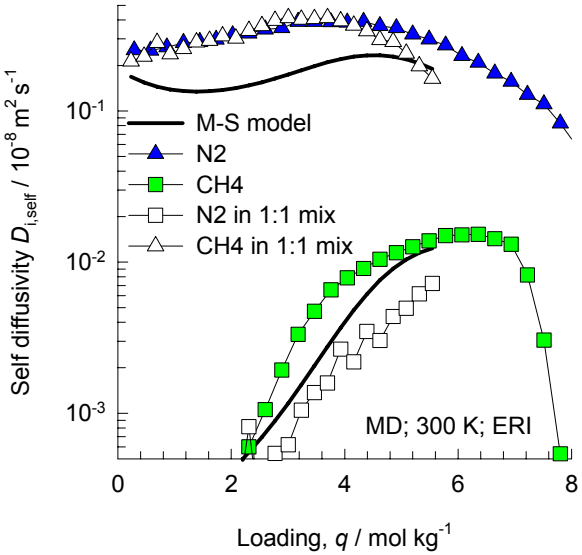
M-S model
N2
CH4
N2 in 1:1 mix
CH4 in 1:1 mix
MD; 300 K; ERI
Self diffusivity $D_{i,self}$ / 10^{-8} m^2 s^{-1}
Loading, q / mol kg^{-1}
10^{-1}
10^{-2}
10^{-3}
0
2
4
6
8

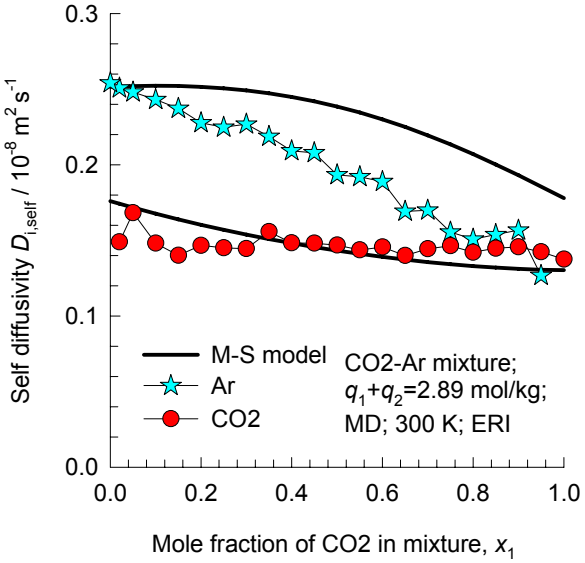
M-S model
Ar
CO2
CO2-Ar mixture;
q_1+q_2=2.89 mol/kg;
MD; 300 K; ERI
Self diffusivity $D_{i,self}$ / 10^{-8} m^2 s^{-1}
Mole fraction of CO2 in mixture, x_1
0.0
0.1
0.2
0.3
0.0
0.2
0.4
0.6
0.8
1.0

Figure 52

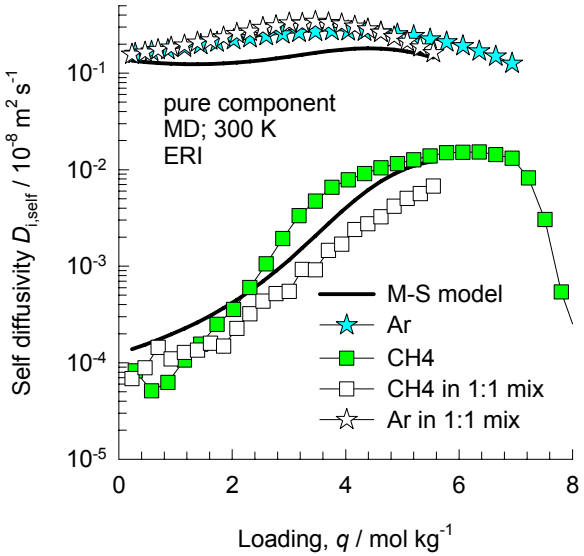
pure component
MD; 300 K
ERI
M-S model
Ar
CH4
CH4 in 1:1 mix
Ar in 1:1 mix
Self diffusivity $D_{i,self}$ / 10^{-8} m^2 s^{-1}
Loading, q / mol kg^{-1}

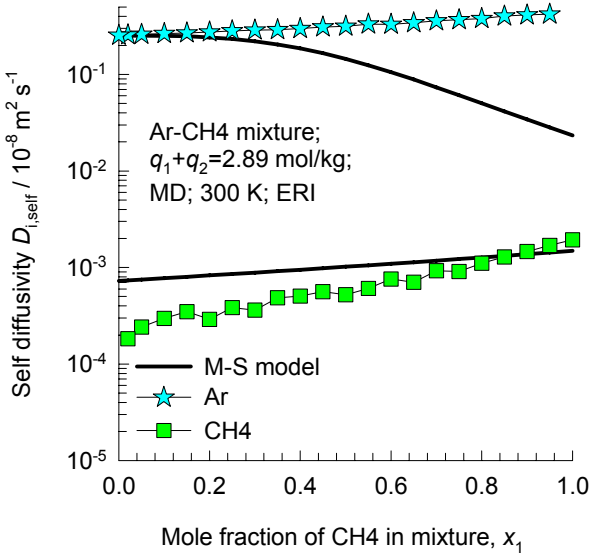
Ar-CH4 mixture;
q_1+q_2=2.89 mol/kg;
MD; 300 K; ERI
M-S model
Ar
CH4
Self diffusivity $D_{i,self}$ / 10^{-8} m^2 s^{-1}
Mole fraction of CH4 in mixture, x_1

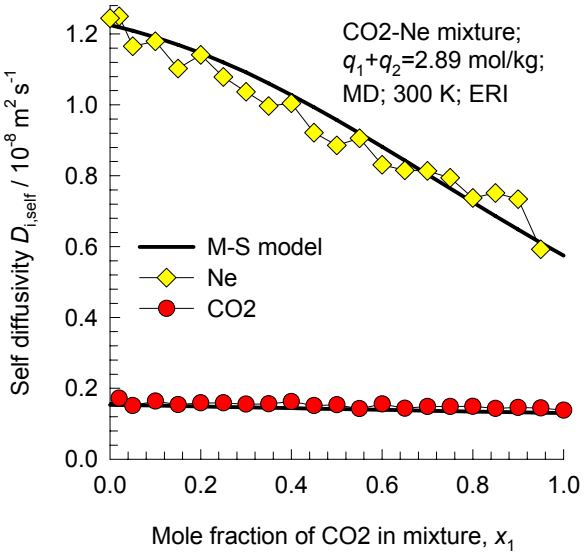
CO2-Ne mixture;
q_1+q_2=2.89 mol/kg;
MD; 300 K; ERI
M-S model
Ne
CO2
Self diffusivity $D_{i,self}$ / 10^{-8} m^2 s^{-1}
Mole fraction of CO2 in mixture, x_1

Figure 53

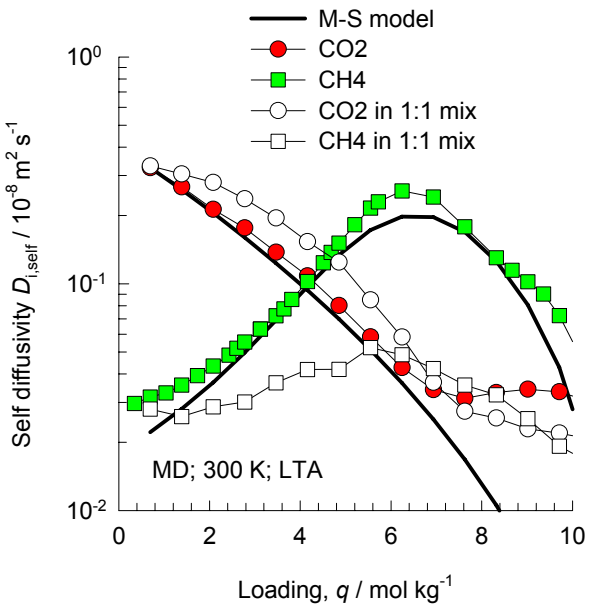
M-S model
CO2
CH4
CO2 in 1:1 mix
CH4 in 1:1 mix
MD; 300 K; LTA
Self diffusivity $D_{i,self}$ / 10^{-8} m^2 s^{-1}
Loading, q / mol kg^{-1}

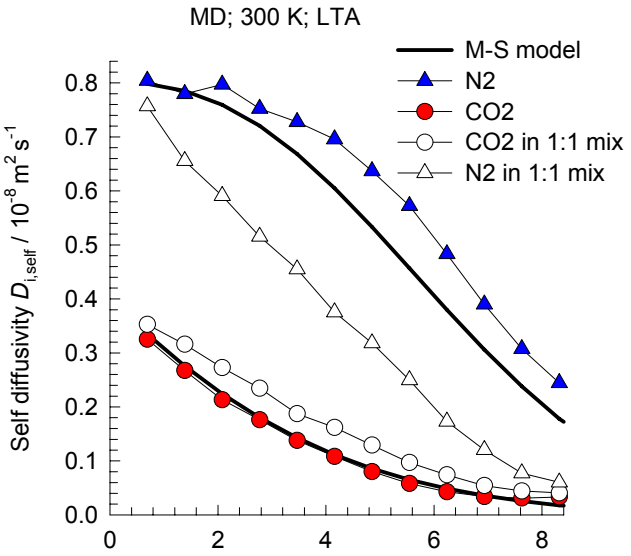
MD; 300 K; LTA
M-S model
N2
CO2
CO2 in 1:1 mix
N2 in 1:1 mix
Self diffusivity $D_{i,self}$ / 10^{-8} m^2 s^{-1}

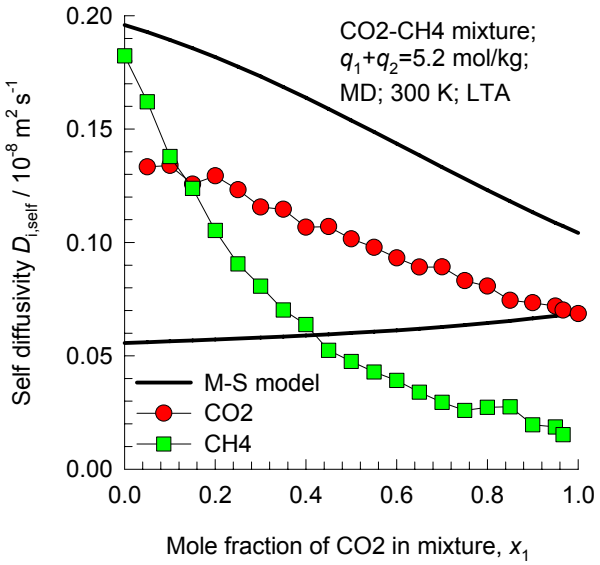
CO2-CH4 mixture;
q_1+q_2=5.2 mol/kg;
MD; 300 K; LTA
M-S model
CO2
CH4
Self diffusivity $D_{i,self}$ / 10^{-8} m^2 s^{-1}
Mole fraction of CO2 in mixture, x_1

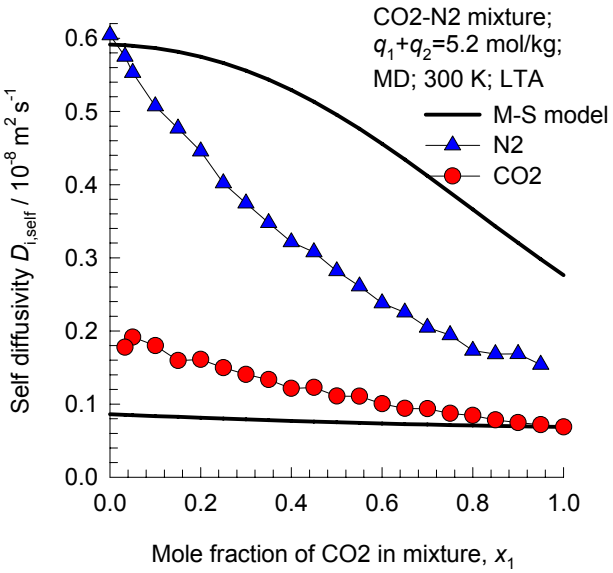
CO2-N2 mixture;
q_1+q_2=5.2 mol/kg;
MD; 300 K; LTA
M-S model
N2
CO2
Self diffusivity $D_{i,self}$ / 10^{-8} m^2 s^{-1}
Mole fraction of CO2 in mixture, x_1

Figure 54

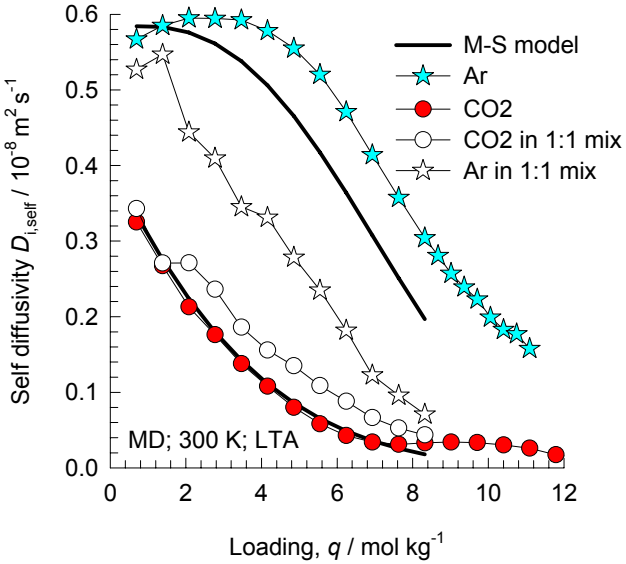
M-S model
Ar
CO2
CO2 in 1:1 mix
Ar in 1:1 mix
MD; 300 K; LTA
Self diffusivity $D_{i,self}$ / 10^{-8} m^2 s^{-1}
Loading, q / mol kg^{-1}

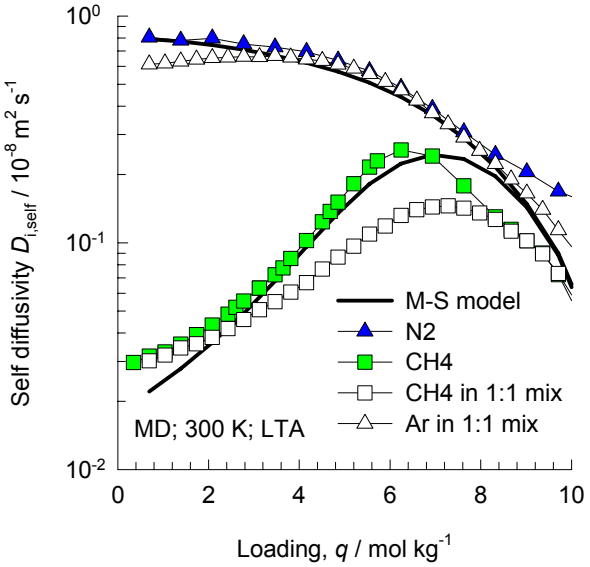
M-S model
N2
CH4
CH4 in 1:1 mix
Ar in 1:1 mix
MD; 300 K; LTA
Self diffusivity $D_{i,self}$ / 10^{-8} m^2 s^{-1}
Loading, q / mol kg^{-1}

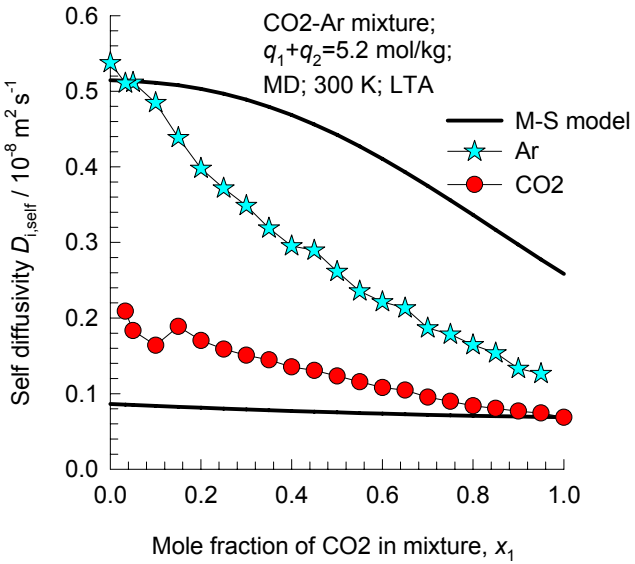
CO2-Ar mixture;
q_1+q_2=5.2 mol/kg;
MD; 300 K; LTA
M-S model
Ar
CO2
Self diffusivity $D_{i,self}$ / 10^{-8} m^2 s^{-1}
Mole fraction of CO2 in mixture, x_1

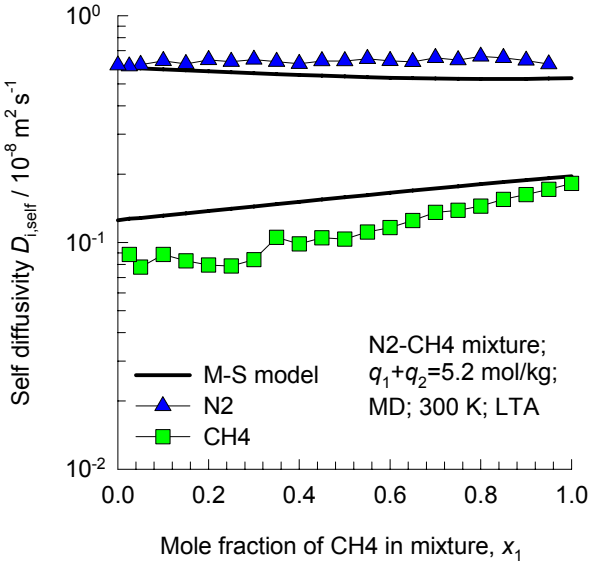
M-S model
N2
CH4
N2-CH4 mixture;
q_1+q_2=5.2 mol/kg;
MD; 300 K; LTA
Self diffusivity $D_{i,self}$ / 10^{-8} m^2 s^{-1}
Mole fraction of CH4 in mixture, x_1

Figure 55

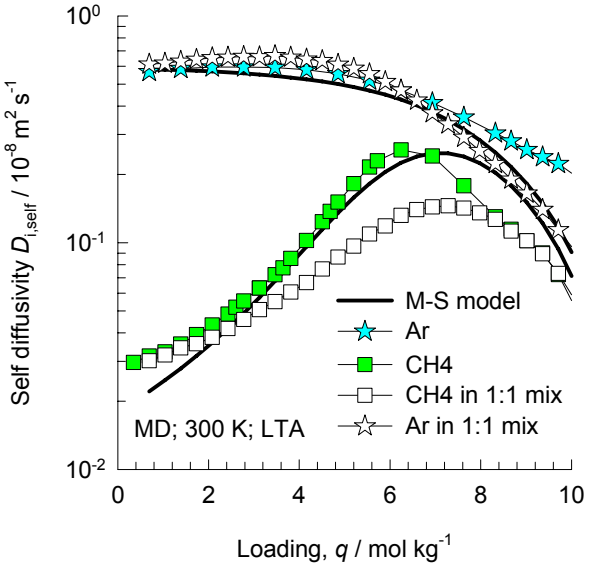
Self diffusivity $D_{i,self}$ / 10^{-8} m^2 s^{-1}
Loading, q / mol kg^{-1}
M-S model
Ar
CH4
CH4 in 1:1 mix
Ar in 1:1 mix
MD; 300 K; LTA

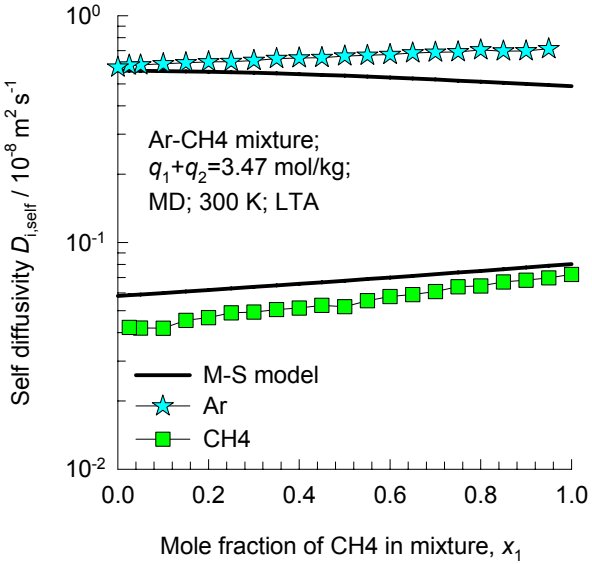
Self diffusivity $D_{i,self}$ / 10^{-8} m^2 s^{-1}
Ar-CH4 mixture;
q_1+q_2=3.47 mol/kg;
MD; 300 K; LTA
M-S model
Ar
CH4
Mole fraction of CH4 in mixture, x_1

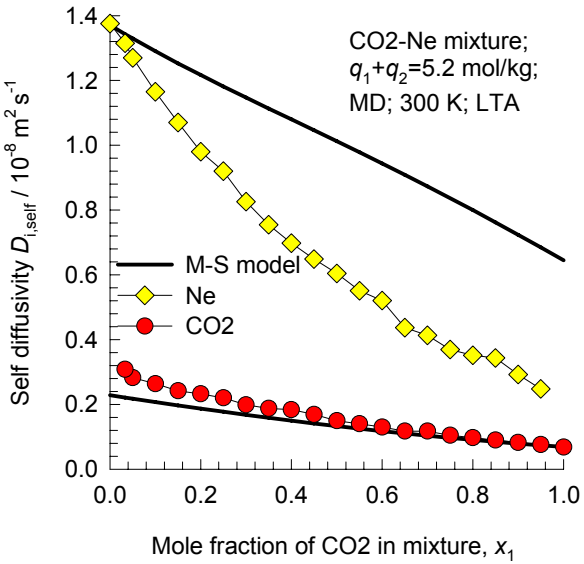
Self diffusivity $D_{i,self}$ / 10^{-8} m^2 s^{-1}
CO2-Ne mixture;
q_1+q_2=5.2 mol/kg;
MD; 300 K; LTA
M-S model
Ne
CO2
Mole fraction of CO2 in mixture, x_1

Figure 56

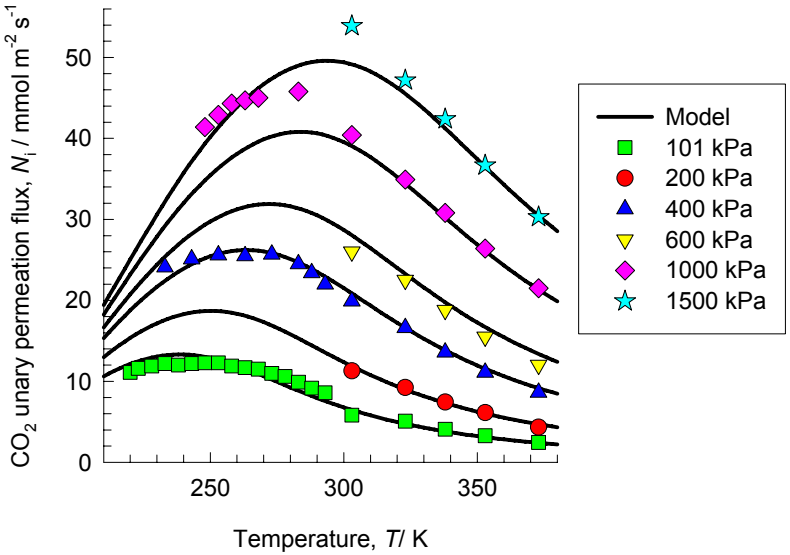

Unary permeation data of van den Bergh (2007) compared to model calculations

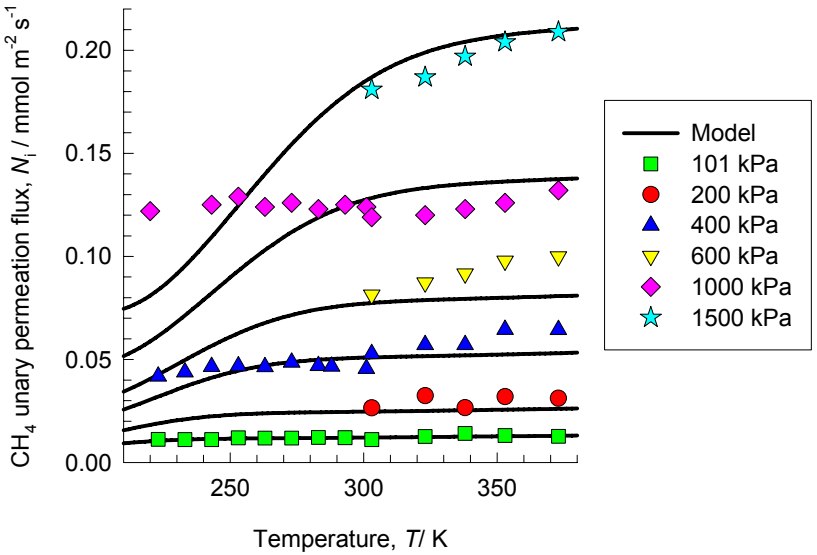

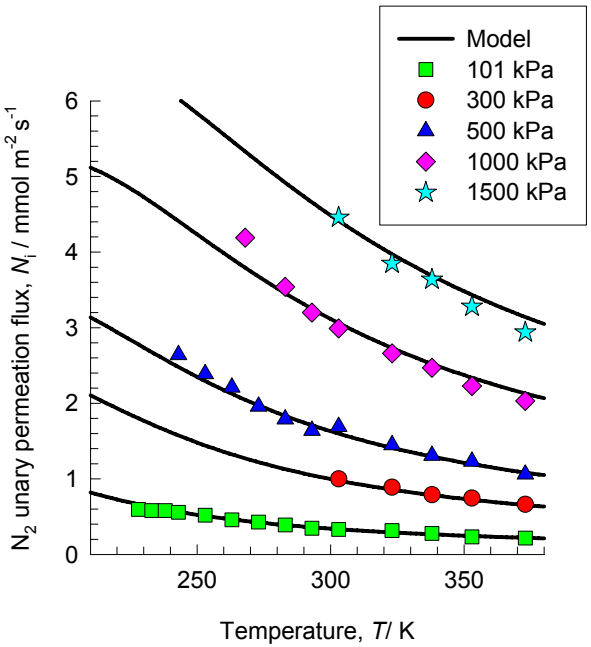

Figure 57

Binary N2-CH4 permeation data of van den Bergh (2007) compared to model calculations

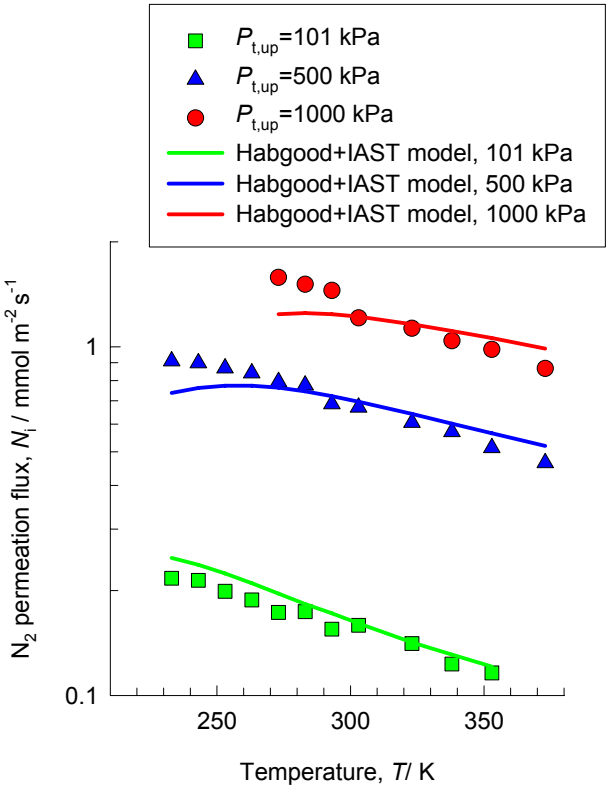

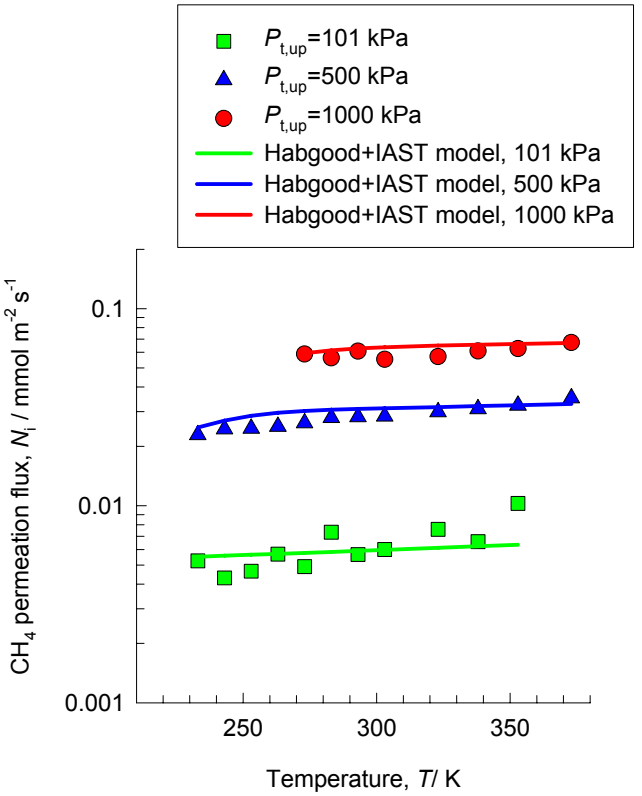

Figure 58

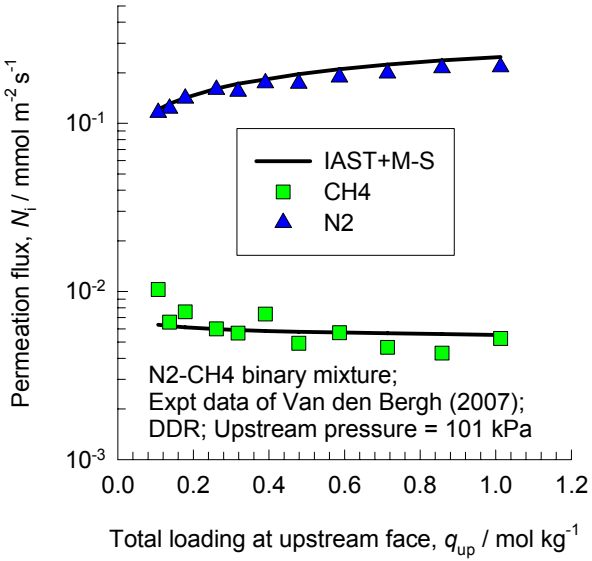

Binary N2-CH4 permeation data of van den Bergh (2007) compared to model calculations

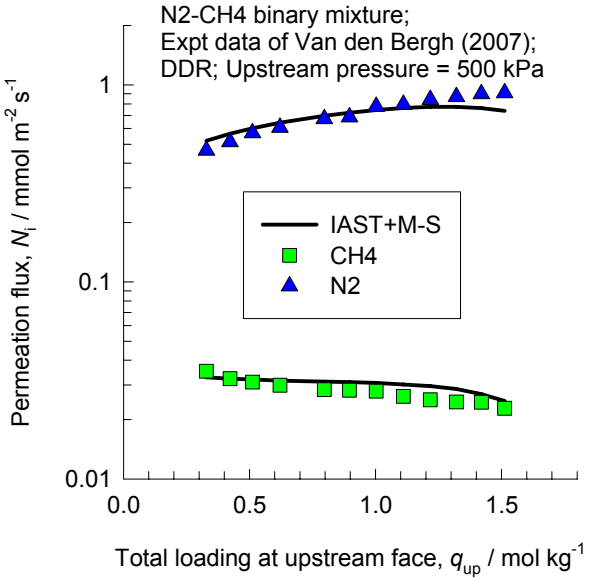

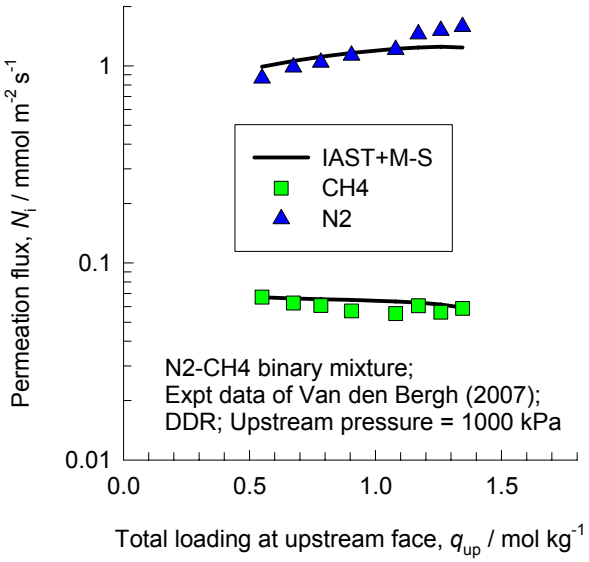

Figure 59

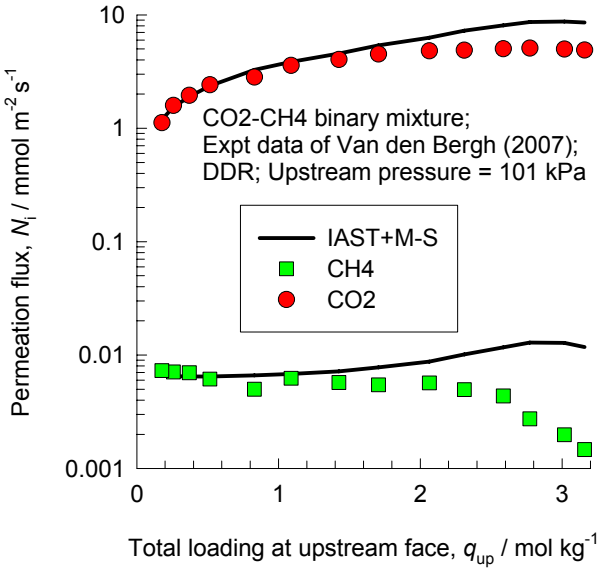

Binary CO2-CH4 permeation data of van den Bergh (2007) compared to model calculations

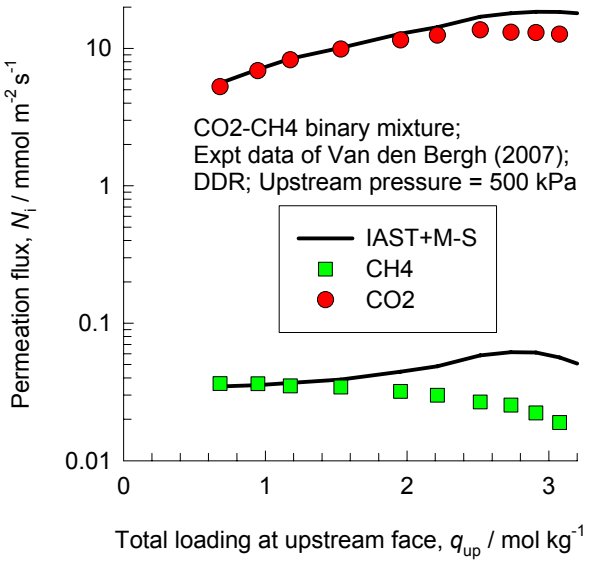

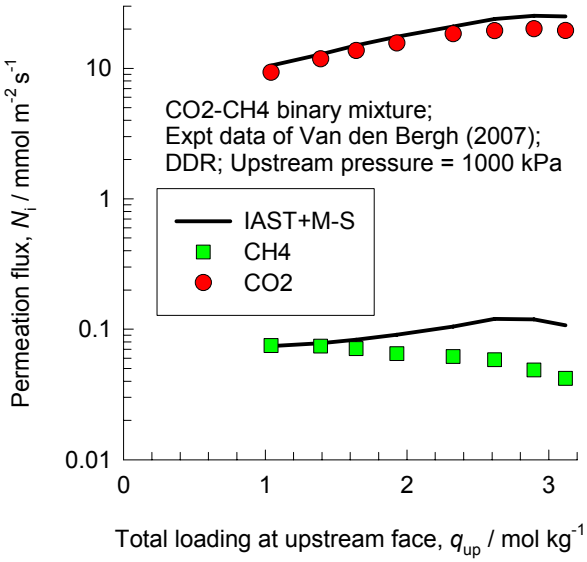

Figure 60

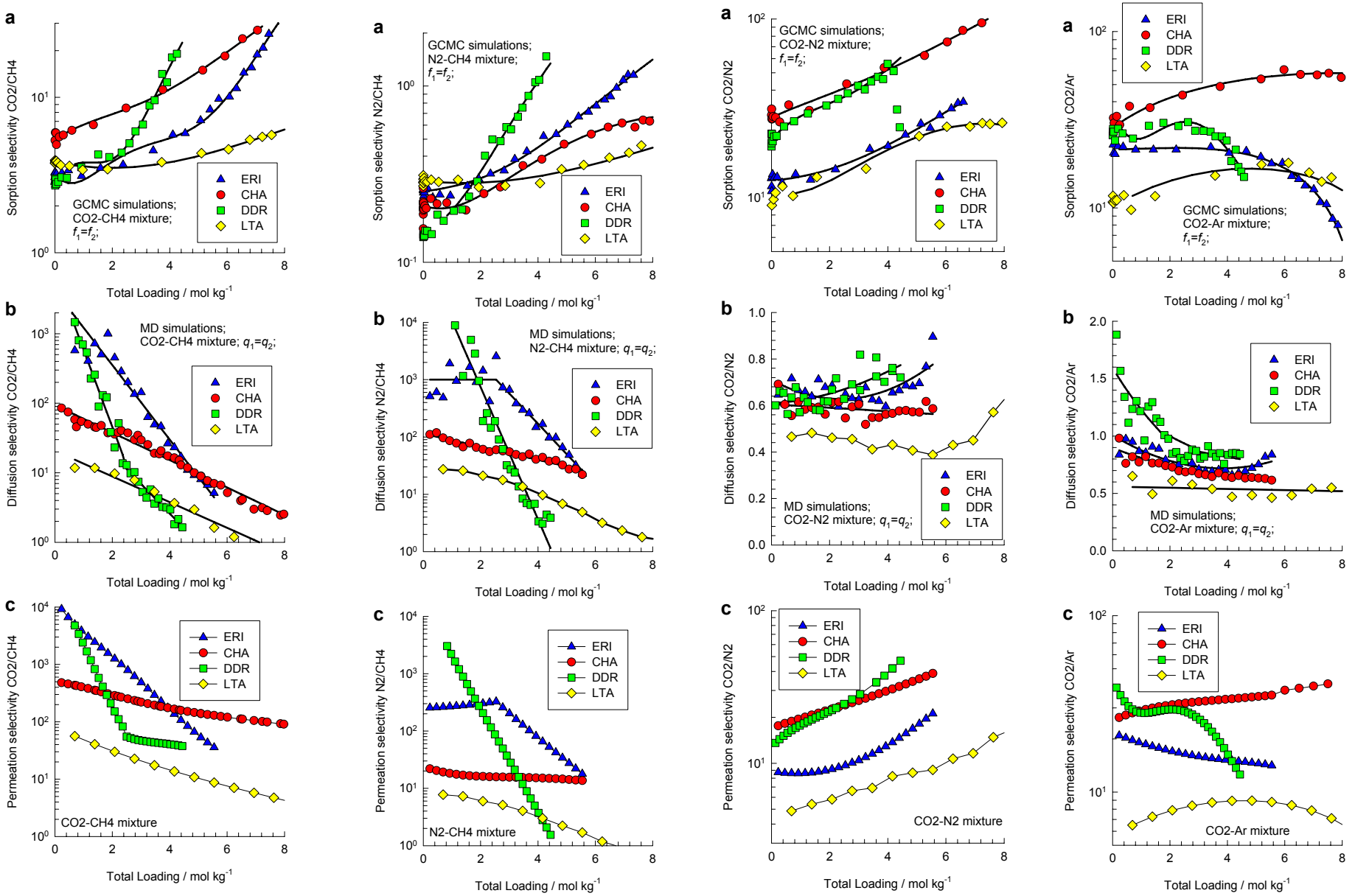
a
Sorption selectivity CO2/CH4
GCMC simulations;
CO2-CH4 mixture;
f_1=f_2;
ERI
CHA
DDR
LTA
Total Loading / mol kg^{-1}
b
Diffusion selectivity CO2/CH4
MD simulations;
CO2-CH4 mixture; q_1=q_2;
c
Permeation selectivity CO2/CH4
CO2-CH4 mixture
a
Sorption selectivity N2/CH4
GCMC simulations;
N2-CH4 mixture;
f_1=f_2;
b
Diffusion selectivity N2/CH4
MD simulations;
N2-CH4 mixture; q_1=q_2;
c
Permeation selectivity N2/CH4
N2-CH4 mixture
a
Sorption selectivity CO2/N2
GCMC simulations;
CO2-N2 mixture;
f_1=f_2;
b
Diffusion selectivity CO2/N2
MD simulations;
CO2-N2 mixture; q_1=q_2;
c
Permeation selectivity CO2/N2
CO2-N2 mixture
a
Sorption selectivity CO2/Ar
GCMC simulations;
CO2-Ar mixture;
f_1=f_2;
b
Diffusion selectivity CO2/Ar
MD simulations;
CO2-Ar mixture; q_1=q_2;
c
Permeation selectivity CO2/Ar
CO2-Ar mixture